ORNL/Sub/86-18417/1

ornl

OAK RIDGE NATIONAL LABORATORY

MARTIN MARIETTA

Energy Division

A Nominal Set of High-Altitude EMP Environments

Conrad L. Longmire
Robert M. Hamilton
Jane M. Hahn

POWER SYSTEMS TECHNOLOGY PROGRAM

OPERATED BY
MARTIN MARIETTA ENERGY SYSTEMS, INC.
FOR THE UNITED STATES
DEPARTMENT OF ENERGY

Printed in the United States of America. Available from
National Technical Information Service
U.S. Department of Commerce
5285 Port Royal Road, Springfield, Virginia 22161
NTIS price codes—Printed Copy: A06 Microfiche A01

ORNL/Sub/86-18417/1
(MRC-R-991R-1)
Dist. Category UC-97a,b,c

Energy Division

A NOMINAL SET OF HIGH-ALTITUDE EMP ENVIRONMENTS

Conrad L. Longmire
Robert M. Hamilton
Jane M. Hahn

Manuscript Completed: April 1986
Date Published: February 1987

Mission Research Corporation
P. O. Drawer 719
Santa Barbara, CA 93102-1245

Contract No. DNA 001-85-C-0080

THIS WORK WAS PARTLY SPONSORED BY THE DEFENSE NUCLEAR AGENCY UNDER RDT&E
RMSS CODE B326085466VC0032 25904D
Companion Report DNA-TR-86-300

ADDITIONAL SUPPORT WAS PROVIDED BY

THE OAK RIDGE NATIONAL LABORATORY
POWER SYSTEMS TECHNOLOGY PROGRAM
Oak Ridge, Tennessee 37831
operated by
MARTIN MARIETTA ENERGY SYSTEMS, INC.
for the
U.S. DEPARTMENT OF ENERGY
under Contract No. DE-AC05-840R21400

and by

C. L. LONGMIRE, PRIVATELY

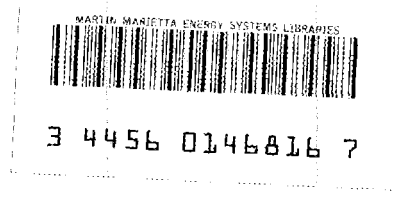

TABLE OF CONTENTS

ABSTRACT

This report presents high-altitude EMP (HEMP) environments calculated by the CHAP code for a nominal large yield burst at 400 km over the central U.S. Nominal, unclassified weapon output parameters were used, along with unclassified EMP theory and calculational techniques. While the resulting environments do not represent upper bounds, they should be useful in developing understanding of the effect of HEMP on electrical and electronic systems.

The calculated environments illustrate the wide variability of the HEMP from a single burst, depending on ground range and azimuth from ground zero. Analytic fits to the HEMP fields are provided to facilitate coupling calculations. The CHAP results are justified by a detailed examination of Compton currents, air conductivities, and the resulting fields. It is shown that both HEMP theory and the calculations conserve energy scrupulously.

LIST OF ILLUSTRATIONS

LIST OF TABLES

THIS PAGE IS INTENTIONALLY LEFT BLANK.

SECTION 1
INTRODUCTION

The principal purpose of this report is to provide an unclassified set of high-altitude EMP (HEMP) environments. It was our desire that these environments be near the maximum that can be produced by high-altitude nuclear explosions, without using any values of weapon output parameters that are classified under the Atomic Energy Act of 1954. This has turned out to be feasible.

We wish to emphasize that the environments presented here do not represent upper bounds to possible HEMP environments and are not a substitute for standards promulgated by the U. S. Government. However, they should be highly useful in efforts to develop understanding of the interaction of HEMP with electrical and electronic systems. In particular, the variability of the HEMP with range and azimuth is well illustrated by our results.

A second purpose of this report is to provide sufficient details of the HEMP calculations for knowledgeable readers (physicists and electrical engineers) to see for themselves that the results are at least approximately correct. To this end the outgoing wave equation, which is the basic equation of HEMP theory, is derived directly from the law of energy conservation in Section 2. Following presentation of the HEMP calculated by the CHAP code in Section 3, and formulae fitting those results as functions of time, range and azimuth in Section 4, justification of the results is presented in Section 5. The calculated Compton current and air conductivity are shown to be consistent with the relevant simple physics, and the electric field is then shown to follow from those results and the outgoing wave theory. Section 6 presents Fourier transforms and contour plots of pulse amplitude and impulse.

SECTION 2
ELEMENTS OF HEMP THEORY

A recent discussion of the theory of HEMP is contained in Reference 1, which starts from Maxwell's equations. A simpler (but approximate) derivation, which directly uses the conservation of energy, is given in this section.

2.1 HEMP GEOMETRY

The gamma rays from a nuclear explosion travel outward from the burst point with the speed c of light. Since the gammas are emitted by the nuclear device in a time span of about 10^{-8} second, at some time t after the burst the gammas occupy a spherical shell, centered about the burst point, of radius

$$r = ct \ , \tag{1}$$

and of radial thickness

$$\Delta r_{\gamma} \approx c \times 10^{-8} \approx 3 \text{ meters} \ . \tag{2}$$

The Compton recoil electrons are born in that part of this shell that intersects the atmosphere. Since the Compton electrons live for about 10^{-6} second, before being brought to rest by collisions with air atoms, the Compton current exists in a spherical shell having the same outer radius as the gammas, but with a radial thickness

??

$$\Delta r_c \approx c \times 10^{-6} \approx 300 \text{ meters} . \qquad (3)$$

The Compton electrons move radially outwards at birth, on the average, but they begin immediately to be deflected sideways, transverse to the radial direction, by the geomagnetic field. They therefore form a current density with both radial and transverse components, J_r and J_t respectively. The principal source of the HEMP is J_t, because it can radiate electromagnetic fields that propagate radially outward, maintaining phase with the Compton current. J_t also radiates waves radially inward, but these are mostly absorbed by air conductivity. J_r could (except in cases of spherical symmetry) radiate waves in transverse or oblique directions; these also are mostly absorbed by air conductivity.

The air conductivity σ results from secondary ionization produced by the Compton electrons. The conductivity is essentially zero at the outside of the Compton electron shell, and rises as we move inward from there, or as we stay at a fixed radius and let the Compton electron shell sweep over us in time.

2.2 THE RETARDED TIME

The Compton scattering mean-free-path λ_γ of the gamma rays is of the order of 6 km in the center of the HEMP source region (altitude ≈ 30 km). The flux of unscattered gammas decreases by a factor $e^{-1} = 0.37$ in this distance. This distance is much longer than the 300-meter thickness of the Compton current shell. (The HEMP is usually even shorter, of the order of 50 meters, because of air conductivity.) Therefore, if we look at the Compton current waveform, instead of at individual Compton electrons, we see a current pulse that propagates at the speed of light, with its shape and amplitude changing only slowly, i.e., in distances of the order of λ_γ.

??

In this situation it is convenient to replace the variable t by the retarded time

$$T = t - \frac{r}{c} . \qquad (4)$$

The retarded time T is zero at the front end of the Compton current pulse, since $r = ct$ there, and increases as we move back in the pulse, where $r < ct$. At any r, T is the time after the onset of the Compton current pulse. Figure 1 is a sketch of the pulse at two different real times t_1 and t_2, with t_2 later than t_1. Since we have graphed the pulse as a function of r, the retarded time is represented by cT, the distance behind the front of the pulse. The amplitude and shape of the pulse have changed only slightly between r_1 and r_2.

Let us therefore think of the transverse Compton current J_t and the air conductivity σ as being functions of r and T. At constant T, J_t and σ vary only slowly with r. It is reasonable to expect that the HEMP electric field E_t will have the same property. We shall try making this assumption, and see in Sections 2.3 and 2.4 that results are consistent.

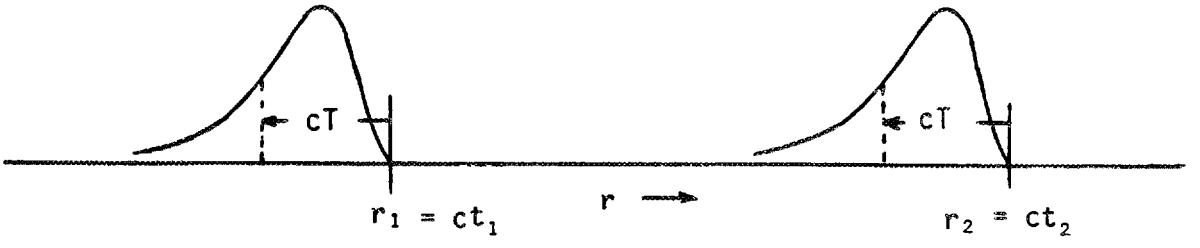

Figure 1. Compton current as a function of r at two different real times t_1 and t_2.

2.3 OUTGOING WAVE EQUATION IN PLANE GEOMETRY*

Let us assume at first, for simplicity, that the nuclear burst is moved very far away, but is made very strong, so that the gamma flux remains finite. Then, over distances of a few kilometers, we can neglect the curvature of the Compton current shell. Over these distances, the HEMP will appear to be a planar pulse propagating parallel to the Cartesian coordinate r.

The instantaneous power density in the HEMP is E_t^2/Z_0 watts/m^2, where $Z_0 \approx 377$ ohms. This depends on T, and more slowly on r. The partial derivative with respect to r at constant T,

$$\frac{\partial}{\partial r}\frac{E_t^2}{Z_0}\Big)_T \quad \frac{\text{watts}}{m^3}, \tag{5}$$

is the increase in power density at a fixed T in the wave per meter of travel. Conservation of energy requires that this increase be equal to the power put into the wave by the total electric current. This power is

$$-E_t(J_t + \sigma E_t) \quad \frac{\text{watts}}{m^3}. \tag{6}$$

Note that we have included both Compton and conduction currents. The quantities here are to be evaluated at the same T (and r) as in the expression (5). Thus conservation of energy is expressed by

$$\frac{\partial}{\partial r}\frac{E_t^2}{Z_0} = -E_t(J_t + \sigma E_t), \tag{7}$$

---

* Sections 2.3 and 2.4 are taken from Reference 5.

or, on working out the derivative,

$$\frac{\partial}{\partial r} E_t = - \frac{Z_0}{2} (J_t + \sigma E_t) . \quad \text{(at constant T)} \tag{8}$$

This is the outgoing wave equation of HEMP theory, first derived by Longmire in Reference 2. It says that, in the absence of any conductivity, the amplitude increases according to

$$E_t(r,T) = - \frac{Z_0}{2} \int J_t(r,T) dr . \quad \text{(at constant T)} \tag{9}$$

The minus sign is an example of Lenz's law. In the absence of any Compton current, E_t is attenuated according to

$$E_t(r,T) = E_{t0}(T) \exp(-Z_0 \sigma r/2) . \quad \text{(at constant T)} \tag{10}$$

Since σ depends on T, the wave gradually changes its shape as it is attenuated. However, E_t will have the expected property provided σ is not too large, a point to which we return in Section 2.6.

2.4 OUTGOING WAVE EQUATION IN SPHERICAL GEOMETRY

The derivation of Section 2.3 is easily extended to spherical geometry. In this case we focus our attention on a fixed element $\delta\Omega$ of solid angle. The power flow in this element is

$$r^2 \delta\Omega \frac{E_t^2}{Z_0} , \tag{11}$$

and the conservation of energy is expressed by

$$\frac{\partial}{\partial r}\,\delta\Omega\,\frac{(rE_t)^2}{Z_0} = -\,r^2\delta\Omega E_t(J_t + \sigma E_t)\ . \qquad (12)$$

Working out the derivative here and canceling common factors gives

$$\frac{\partial}{\partial r}\,(rE_t) = -\,\frac{Z_0}{2}\,(rJ_t + \sigma rE_t)\ . \qquad (13)$$

This is the outgoing wave equation in spherical geometry, first derived by Karzas and Latter in Reference 3. If the nuclear burst is very far away, $r \to \infty$, it reduces to equation 8 over r-intervals that remain finite. If both J_t and σ vanish, the solution is

$$rE_t = \text{constant}\ , \quad \text{or } E_t \sim 1/r\ , \qquad (14)$$

appropriate for a spherically expanding wave. Equation 8 in this case yields E_t = constant, appropriate for a plane wave. In many cases it is sufficient to use equation 8 in the source region, which is usually thin compared with r, but then put $E_t \sim 1/r$ after the HEMP leaves the source region.

2.5 COMPLETION OF ENERGY CONSERVATION

Since we have derived the outgoing wave equations from energy conservation, it would appear that they automatically conserve energy. However, there is one more step to be taken to make energy conservation

complete. What we have done so far is to ensure that the energy put into the wave by the Compton current either remains in the wave or goes into Joule heating through the conductivity term. We must also ensure that the energy put into the wave by the Compton electrons is taken out of their kinetic energy. This can be accomplished by solving the equations of motion of the Compton electrons in the presence of the HEMP electric and magnetic fields. It is well known that the combination of Maxwell's equations with the equations of motion of charged particles conserves the total energy of fields and particles.

The computer code CHAP (Ref. 4) solves both Maxwell's equations and the Compton electron equations of motion simultaneously, including the forces of the fields on the electrons. Such codes are called self-consistent.

The derivations of the outgoing wave equations in Sections 2.3 and 2.4 were only approximate in two respects. First, reflection of the outgoing wave by the air conductivity was neglected. This neglection can be justified if the conductivity σ is not too large, as is discussed in Section 2.6. The code CHAP treats both outgoing and ingoing waves; the reflection terms are included. The effect of including the ingoing waves on the HEMP observed at ground level is never substantial.

Second, the derivations neglected diffraction; it was assumed that wave energy flows only in the radial direction. The justification for this assumption is that the HEMP wave is very broad in its transverse dimensions compared with its radial wavelengths. The breadth is of the order of at least the atmospheric scale height, or about 6 km, whereas the radial wavelengths are of the order of 60 m. Direct calculations (Ref. 5) of the effect of diffraction on the HEMP observed from the Kingfish event in Operation Fishbowl (a rather severe geometry) showed that the change in amplitude was less than 1%.

The derivations of the outgoing wave equations given here are similar to those applied in lasers. In fact, the generation mechanism of the HEMP can be regarded as a free-electron laser.

2.6 SOLUTION OF THE OUTGOING WAVE EQUATION

In this section we derive some elementary properties of the solution of the planar outgoing wave equation (8). The spherical form, equation (13), could be used with little increase in difficulty.

Consider a nuclear burst at, say, 100 km altitude, and a ray that slopes downward to the ground. As the gamma shell moves outward, increasing r, the air density is at first too small to make a significant number of Compton electrons, so that J_t is effectively zero. The air conductivity produced by the few Compton electrons is also insignificant. Hence the right-hand side of equation (8) is effectively zero, and therefore E_t remains equal to zero.

When the ray reaches about 50 km altitude, there is enough air to make a few Compton electrons and a weak J_t, which produce a weak σ. Since E_t will also be still weak, the term σE_t is doubly weak compared with J_t, and can be neglected at first. The solution of equation (8) in this region is then

$$E_t(r,T) \approx -\frac{Z_0}{2} \int J_t(r',T)dr' \ . \qquad (15)$$

Note that the integral here has to be done for each retarded time T that we wish to consider. However, since T is just a constant parameter in the integral, it is clear that the pulse shape of E_t in T will be the same as that of J_t, provided the pulse shape of J_t changes little as r increases.

Now the air density increases approximately exponentially with r, so that the density of Compton electrons does also. Therefore,

$$J_t(r,T) \sim J_{t0}(T) \exp(r/h') \ . \tag{16}$$

Here h' is the scale length of the atmosphere as seen by the sloping ray,

$$h' = h/\cos\theta \ , \tag{17}$$

where h is the atmospheric scale height,

$$h \approx 6.6 \text{ km} \ , \tag{18}$$

and θ is the angle of the ray with respect to the vertical. With the exponential dependence of J_t, the integral in equation (15) is easily performed, with the result

$$E_t(r,T) \approx - \frac{Z_0}{2} h' \, J_t(r,T) \ . \tag{19}$$

As the ray goes deeper into the atmosphere, it may happen that the term σE_t is no longer negligible compared with J_t in equation (8). This is bound to happen if the gamma flux F_γ is sufficiently large, since both J_t and σ are proportional to F_γ and equation (19) indicates that E_t is also proportional to F_γ if σE_t is neglected. Since E_t and J_t have opposite signs (according to equation (19)) while σ is positive, the σE_t term will tend to cancel the J_t term. Let us try assuming that the cancellation is complete, so that

$$E_t(r,T) = - J_t(r,T)/\sigma(r,T) \equiv E_s(r,T) \ . \tag{20}$$

The field E_s is called the saturated field; it is the field at which the conduction current cancels the Compton current. It turns out that $E_s(r,T)$ varies only slowly with r, since both J_t and σ are proportional to the product of F_γ and air density. Therefore, the left-hand side of equation (8) is approximately zero, and

$$E_t(r,T) \approx E_s(r,T) \tag{21}$$

is the limiting solution of equation (8) when the product of F_γ and air density is large, i.e., when σ is large.

Under the condition of saturation, ohmic (Joule heating) losses take energy from the wave as fast as Compton electrons add energy to it. The wave is continually being absorbed by conductivity and regenerated by Compton current.

The condition that saturation be reached can be estimated by requiring that equation 19 gives E_t at least as large as E_s. The result is that

$$\frac{Z_0 h'}{2} \geq \frac{1}{\sigma(r,T)} ,$$

or

$$\sigma(r,T) \geq 2/Z_0 h' \approx 10^{-6} \text{ mho/m} . \tag{22}$$

This is a quite low conductivity. At this conductivity, the attenuation rate is, from equation (10),

$$\frac{Z_0\sigma}{2} \approx 1/h' \approx 10^{-4}/m \ . \qquad (23)$$

For wavelengths in the HEMP of the order of 60 meters, it is easy to show that there is little reflection of the outgoing wave from such a conductivity. For larger conductivity, i.e., strong saturation, the wave is absorbed and regenerated by the Compton current, so that reflection makes little difference.

Note that the saturated field, equation (20), does depend on the retarded time T. The reason is that J_t, as a function of T, rises to a maximum and then falls, whereas the secondary electron density, and therefore σ, continues to rise throughout the Compton current shell. Thus E_s decreases with increasing T. The earlier in the pulse that saturation is reached, the larger is the peak value of the HEMP. Since σ is smaller at earlier T, equation (22) shows that larger gamma flux is required to produce saturation at earlier T.

When the ray reaches about 30 km altitude, it has traversed one mean free path for Compton scattering of the gammas. The production of Compton current is maximum at this altitude. As we proceed to lower altitude, the flux of unscattered gammas decreases rapidly. Once-scattered gammas also make some Compton current, but this is produced mostly after the conductivity has already built up, so the fields produced by scattered gammas are mostly absorbed.

Eventually, the ray reaches an altitude sufficiently low that most of the gammas have been scattered. Both J_t and σ have again become too small to either build up or attenuate the HEMP further, and equation (8) indicates that $E_t(r,T)$ will remain constant in r, i.e., propagate as a free electromagnetic wave. This is the altitude of <u>desaturation</u>. It depends on the magnitude of the gamma flux incident on the atmosphere.

Actually, the spherical equation (13) indicates that E_t will fall as 1/r, r being the distance from the nuclear burst point, in this region. Note that equation (13) gives the same value as equation (8) for the saturated field, since the r-factors on the right-hand side of equation (13) cancel out when one sets the total current equal to zero.

When the HEMP reaches the ground, it is reflected. The reflection can be calculated by well-known procedures. The total fields seen by systems near the ground are the sums of incident and reflected fields, with appropriate time delays. Since reflection depends on soil conductivity, HEMP environments are generally given as incident fields only.

SECTION 3
HEMP CALCULATION BY CHAP CODE

3.1 WHAT CHAP DOES

The computer code CHAP (Ref. 4) solves Maxwell's equations in spherical coordinates r, θ, ϕ, where θ is the polar angle measured from the downward vertical through the burst point and ϕ is the azimuthal angle. The angular derivatives in the equations are dropped, which amounts to neglecting diffraction (see Section 2.5). Both outgoing and ingoing waves are included, as well as the radial electric field E_r. The geomagnetic field is put into the code in the well-known dipole approximation. The curvature of the earth and atmosphere is included. The gamma transport is handled by free streaming, plus a first-order correction to include gammas that have been scattered through small angles only, and so have small time delay. Gammas that are scattered through large angles fall behind the others, and make little contribution to the early HEMP.

Sample Compton electrons are injected at sequences of r's and retarded times T, with energies and angular distributions appropriate for Compton scattering. Their equations of motion are solved in the presence of both the geomagnetic and HEMP fields. Energy loss and multiple scattering in collisions with air atoms are taken into account. The total Compton current density is computed by summing over the sample Compton electrons.

The secondary electrons produced by the Compton electrons are accumulated. Some secondaries are energetic enough to produce tertiaries, etc, and this build-up of ionization is included with the appropriate time

delay (Ref. 6). From the total density of electrons, the air conductivity is calculated by assigning the electrons a mobility that depends on the electric field and the air density. (Reference 7 gives some details of the conductivity calculation.) This conductivity, along with the Compton current, are used in advancing the fields by Maxwell's equations.

Attachment and recombination of the electrons are also included, but these have only small effects within the short time span of the HEMP at the air densities in the source region. Avalanching, which can become significant for large electric fields, is also included.

3.2 CHOICE OF WEAPON OUTPUT PARAMETERS

For the HEMP calculations presented in this report we have assumed that the total gamma output of the weapon is

$$Y_\gamma = 10 \text{ kilotons} = 4.19 \times 10^{13} \text{ Joules} . \qquad (24)$$

With the nominal gamma fraction given by Glasstone and Dolan (Ref. 8) of 0.003, this could come from a weapon with a total yield of 3.3 megatons.

The gammas emitted by a nuclear weapon have energy spectra that range from a small fraction of an MeV to about 10 MeV. This spectrum depends substantially on the outer materials in the nuclear device, where the gammas are produced by neutron interactions. We have assumed that the spectrum can be replaced by a single quantum energy,

$$E_\gamma = 2 \text{ MeV} . \qquad (25)$$

The value assumed here is purely nominal.

The pulse shape of the gammas can be fairly well characterized by giving a rise time, a peak value, and a decay time. Realistic rise times tend to be classified. An exponential decay rate of the order of 10^8 per second is unclassified. We have therefore assumed an isotropic gamma output rate

$$S_\gamma = 0 \quad \text{for} \quad T < 0 \ ,$$

$$S_\gamma = S_0 e^{-\beta T} \ \frac{\gamma\text{-MeV}}{\text{sec}} \quad \text{for} \quad T \geq 0 \ . \tag{26}$$

where

$$S_0 = 2.6 \times 10^{34} \ \gamma\text{-MeV/sec} \ , \tag{27}$$

$$\beta = 10^8/\text{sec} \ . \tag{28}$$

The value of S_0 is such that the time integral of S_γ is equal to Y_γ. The rise time in this pulse is zero, which is unclassified but also unrealistic. However, the HEMP has a finite rise time of its own, connected with the time needed for the Compton electrons to be deflected by the geomagnetic field. This rise time will be apparent in the calculated HEMP. If this rise time is longer than that of the gamma pulse, then taking the latter to be zero should not cause too much error.

For the geomagnetic field, we have assumed the intensity at a point on the ground underneath the burst point to be

$$B_0 = 0.56 \text{ Gauss} , \tag{29}$$

a value appropriate to the central U.S., and have assigned it an appropriate dip angle (from the horizontal) of 70° at the same point.

For most of the calculations, we have used a height of burst of

$$H = 400 \text{ km} . \tag{30}$$

For this height the distances to the horizon are

$$\text{slant range} = SR \approx 2300 \text{ km} , \tag{31}$$

$$\text{ground range} = GR \approx 2200 \text{ km} . \tag{32}$$

Thus such a burst over the central U.S. would include most of the U.S. within the line of sight.

In order to provide a reasonably complete depiction of the dependence of the HEMP on ground range GR and magnetic azimuth ϕ_c, we have performed CHAP calculations for observers on the ground at a set of ground ranges. These are:

$$\begin{aligned} GR &= 0, 233, 501, 777, 1356, 2201 \text{ km} ; \\ \theta_c &= 0, 30, 50, 60, 68, 70.2 \text{ degrees} . \end{aligned} \tag{33}$$

Here θ_c is the angle of the ray with respect to the downward vertical at the burst point. At each ground range, we have calculated for a set of azimuths:

$$\phi_c = 0, 45, 90, 135, 180 \text{ degrees} . \tag{34}$$

Here 0° is magnetic north, 90° is magnetic east, etc. The fields for westward azimuths ($-180° < \phi_c < 0°$) can be obtained by symmetry considerations.

The CHAP coordinate system is indicated by figure 2. The basic coordinates are the spherical polar coordinates r, θ_c, ϕ_c. At the observer these define three orthogonal directions $\vec{r}$, $\vec{\theta}$, $\vec{\phi}$, right handed in the order named. The ϕ direction is locally horizontal and azimuthal about ground zero. The r and θ directions are both in the vertical plane containing the ray from burst point to observer. The θ direction is tipped with respect to the local vertical $\vec{v}$ by an angle θ_0, which is the elevation angle of the burst point as viewed by the observer. The angles χ_c and χ_0 are the magnetic colatitudes of the burst point and the observer, respectively, and ψ_0 is the angle between burst point and observer as viewed from the earth's center. R_e is the radius of the earth, taken in CHAP to be

$$R_e = 6371 \text{ km} . \tag{35}$$

The HEMP, being a transverse wave propagating in the r direction, has electric field components E_θ and E_ϕ. Of these E_ϕ is locally horizontal azimuthal. E_θ can be decomposed into locally vertical and horizontal components,

$$E_v = E_\theta \cos\theta_0 , \text{ (vertical upward)} \tag{36}$$

$$E_\rho = E_\theta \sin\theta_0 . \text{ (horizontal radial)} \tag{37}$$

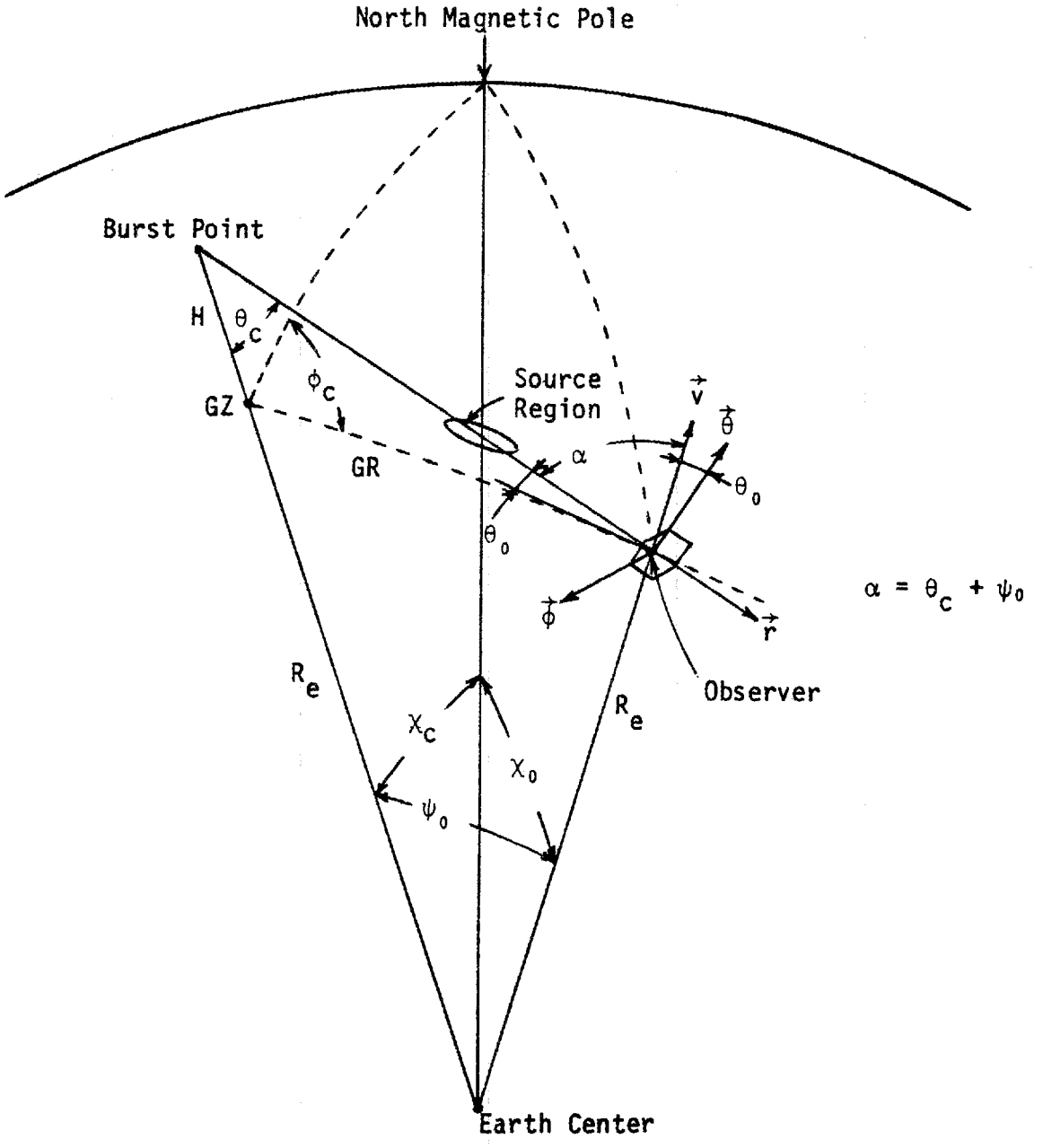

Figure 2. Geometric variables. Dashed curves are great circles on earth surface. GZ = ground zero, GR = ground range.

Relations between the coordinate quantities defined above follow from trigonometry. Some of these relations are stated in Section 4.

For a given observer, the source region for the HEMP observed by him is on the ray from burst point to him, at an altitude such that gammas traveling along that ray have passed through about one Compton scattering mean-free-path of air. For observers on or near the horizon, the source region is at a considerable distance back along the ray toward the burst point. The HEMP seen by an observer is determined by the gamma flux, air density and geomagnetic field in his source region. We shall therefore make use of the coordinates of the source region: ψ_S is the geocentric angle between it and the burst point; χ_S is its magnetic colatitude; ϕ_S is the azimuth of the ray with respect to its local magnetic north; and θ_S is the elevation angle of the burst point with respect to its local horizontal. The symbols are the same as for the same quantities at the observer but with a subscript s instead of 0. In the static dipole model of the geomagnetic field used in CHAP, the local northward-horizontal and downward-vertical components of the field vary with χ_S as, respectively,

$$B_N = \sin\chi_S \ , \tag{38}$$

$$B_D = 2\cos\chi_S \tag{39}$$

Here we have dropped from both equations a factor containing the inverse cube of the distance of the source region from the center of the earth and a normalization constant to produce agreement with equation (29) at ground zero. We shall need only the angular dependence.

3.3 EXPECTED ANGULAR DEPENDENCE OF HEMP

At a given ground range, the flux of gammas incident on the source region is independent of the azimuth ϕ_c. We therefore expect the build up of conductivity to be approximately independent of ϕ_c. The variation of the HEMP with ϕ_c should be determined by the Compton current, and in particular by the deflection of the Compton electrons by the geomagnetic field.

The Compton electrons move radially, on the average, at birth. The ratio $\vec{\beta}_0$ of their velocity to c is not much less than unity in magnitude. As a result of the geomagnetic force $-e\vec{\beta}_0 \times \vec{B}$, they will gradually acquire a transverse velocity (divided by c) proportional to

$$\vec{\beta}_1 = -(\vec{\beta}_0 \times \vec{B})t \ , \tag{40}$$

where t is the time after birth. The magnetic force $-e\vec{\beta}_1 \times \vec{B}$ due to the new velocity will induce an additional velocity

$$\vec{\beta}_2 = -\int (\vec{\beta}_1 \times \vec{B})dt = -[(\vec{\beta}_0 \times \vec{B}) \times \vec{B}]t^2 \ . \tag{41}$$

The direction of $\vec{\beta}_1$ is perpendicular to both $\vec{r}$ and $\vec{B}$. Thus it is a purely transverse direction to $\vec{r}$, and the current proportional to $-\vec{\beta}_1$ radiates an electric field $\vec{E}_1 \sim \vec{\beta}_1$. Actually, since electrons are born continuously after T = 0, so that their number is proportional to T, we expect

$$\vec{E}_1 = -(\vec{\beta}_0 \times \vec{B})T^2 \ . \tag{42}$$

The angular symmetry of this field is that of a magnetic dipole.

The direction of $\vec{\beta}_2$ is perpendicular to both $\vec{\beta}_1$ and $\vec{B}$. In general, it has a part parallel to $\vec{r}$ and a part perpendicular to $\vec{r}$. The latter part is of interest since the current proportional to $-(\vec{\beta}_2)_\perp$ also radiates a field $\vec{E}_2 \sim (\vec{\beta}_2)_\perp$, or

$$\vec{E}_2 \sim [(\vec{\beta}_0 \times \vec{B}) \times \vec{B}]_\perp T^3 \ . \tag{43}$$

The angular symmetry of this field is that of an electric quadrupole.

Since there are only two independent directions transverse to $\vec{r}$, iteration of the procedure that produced equations (40 and (41) yields no new field components, but only higher-power corrections to the time dependence of $\vec{E}_1$ and $\vec{E}_2$. We are interested here in the angular dependences.

These angular dependences are expressed more simply if the geomagnetic field is decomposed into its local r, θ and ϕ components. Let these be B_r, B_θ and B_ϕ respectively; expressions are given for them in Section 4. Then working out the cross products gives

$$E_{1\theta} \sim B_\phi \ , \quad E_{1\phi} \sim -B_\theta \tag{44}$$

and

$$E_{2\theta} \sim B_\theta B_r \ , \quad E_{2\phi} \sim B_\phi B_r \ . \tag{45}$$

The geomagnetic field components here are to be evaluated in the source region for each observer. We shall see that these angular dependences agree well with the CHAP results.

3.4 CHAP RESULTS FOR 400 KM HEIGHT OF BURST

Figures 3 through 20 show the CHAP results for the height of burst of 400 km, for various ground ranges GR and magnetic azimuths PHI. The fields shown are the electric field components E_θ and E_ϕ, plus the magnitude $(E_\theta^2 + E_\phi^2)^{1/2}$. The units are MKS. Solid curves indicate a positive field, dashed curves a negative field.

Accompanying the electric field is the EMP magnetic field, with components

$$B_\phi = E_\theta/c \ , \tag{46}$$

$$B_\theta = - E_\phi/c \ , \tag{47}$$

again in MKS units, where $c = 3 \times 10^8$ m/sec, the speed of light.

The efficiency of conversion of gamma energy to EMP energy is indicated on the E-mag figures, for the largest pulse on the particular figure. The efficiency is always less than 100%, of course. Contributing to inefficiency are the following facts. First, only about half of the gamma energy is transferred to the Compton recoil electron, on the average. Second, the Compton electron loses some energy in collisions with air molecules. Third, the air conductivity absorbs energy from the EMP. The last of these effects is very pronounced for intense gamma flux, where the EMP is saturated over many kilometers in altitude. This accounts for the low efficiencies at the smaller ground ranges in the present case. The maximum efficiency, 6.0%, occurs for the observer on the horizon in the present case. We believe this efficiency could be raised to about 10% by optimum choice of gamma yield Y_γ.

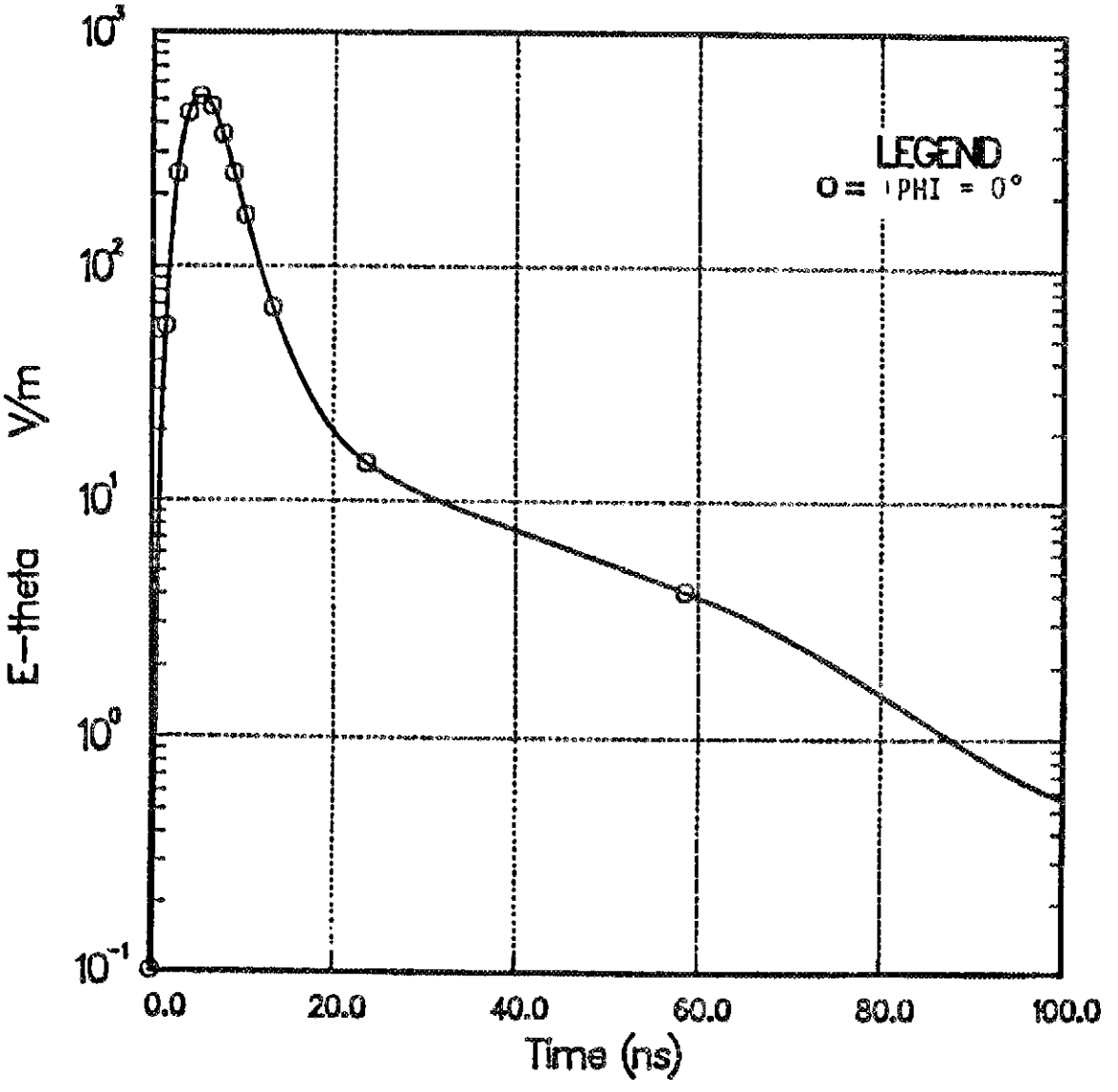

Figure 3. H = 400 km. Observer at GZ. Horizontal northward field. CHAP THETA = 0.

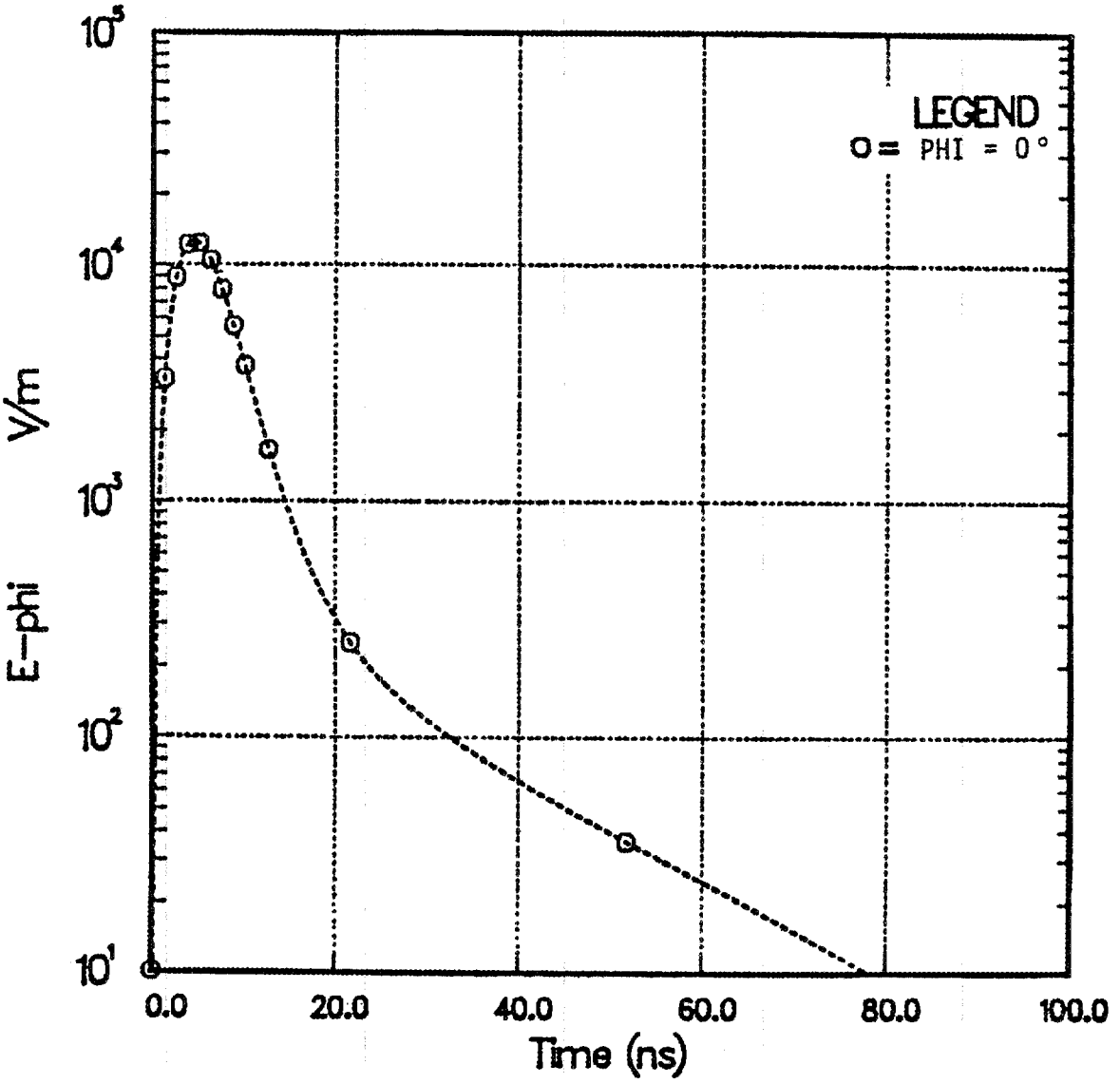

Figure 4. H = 400 km. Observer at GZ. Horizontal eastward field. CHAP THETA = 0.

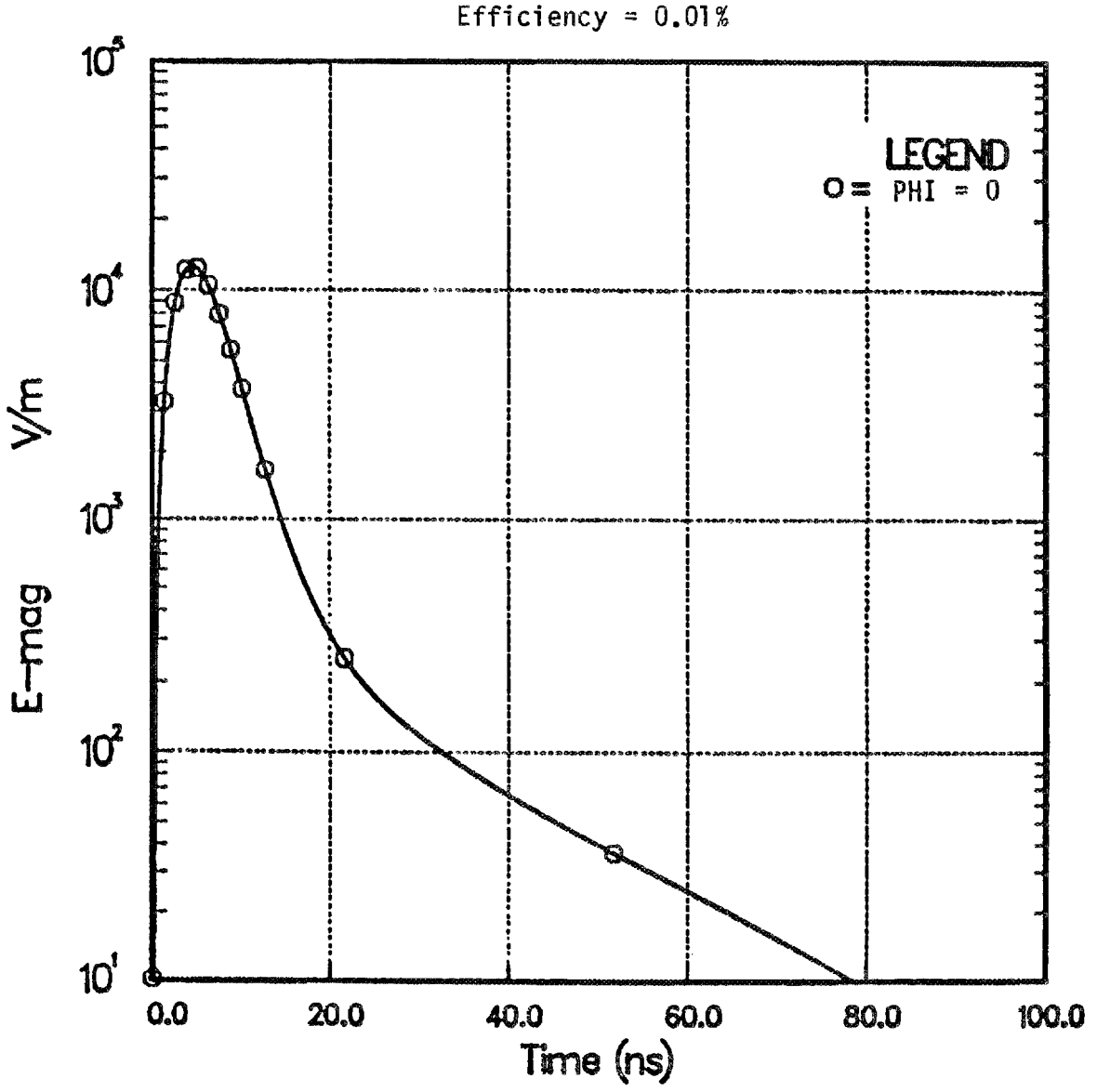

Figure 5. H = 400 km. Observer at GZ.
CHAP THETA = 0.

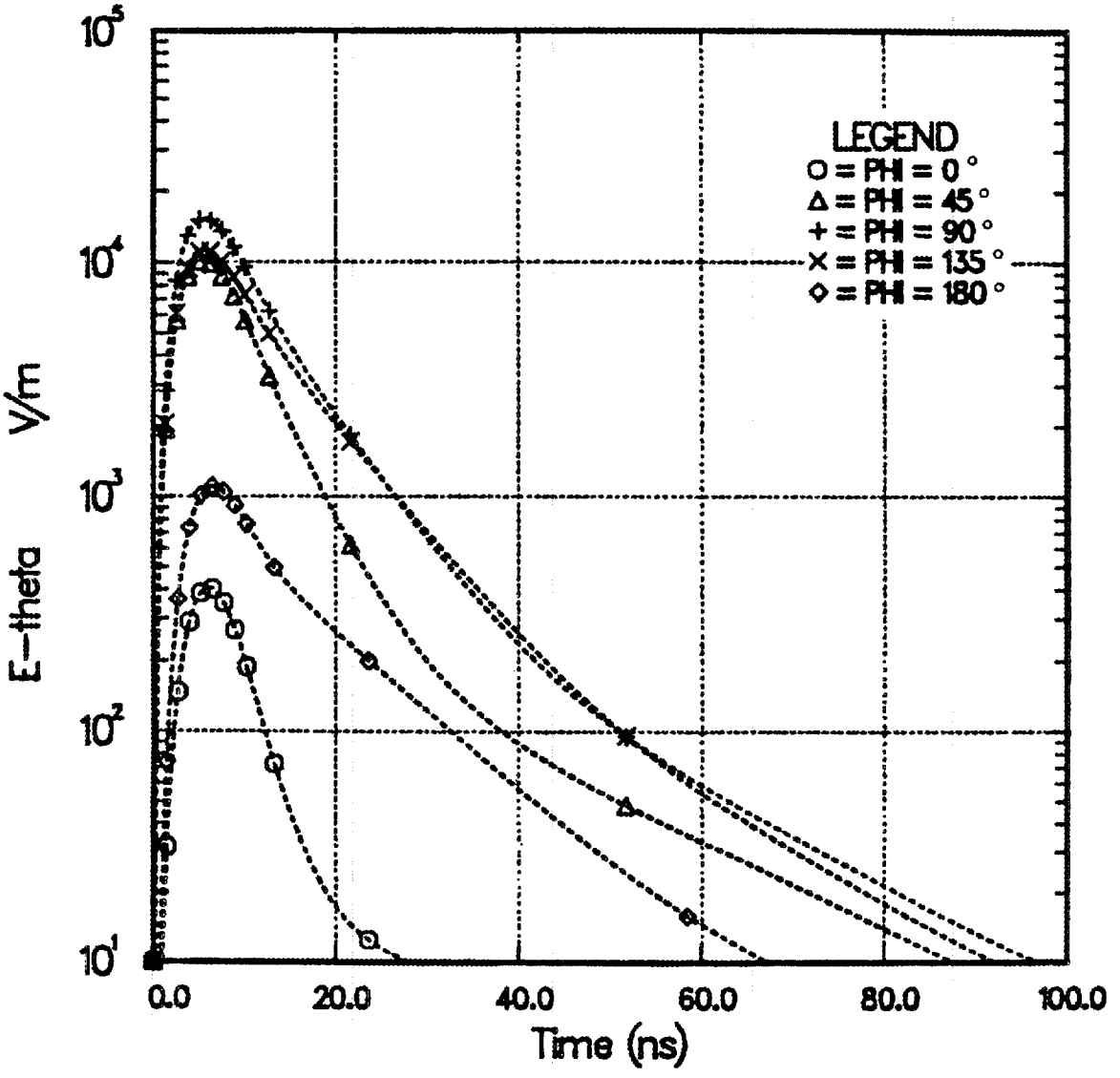

Figure 6. H = 400 km. Observer at GR = 233.5 km.
CHAP THETA = 30°.

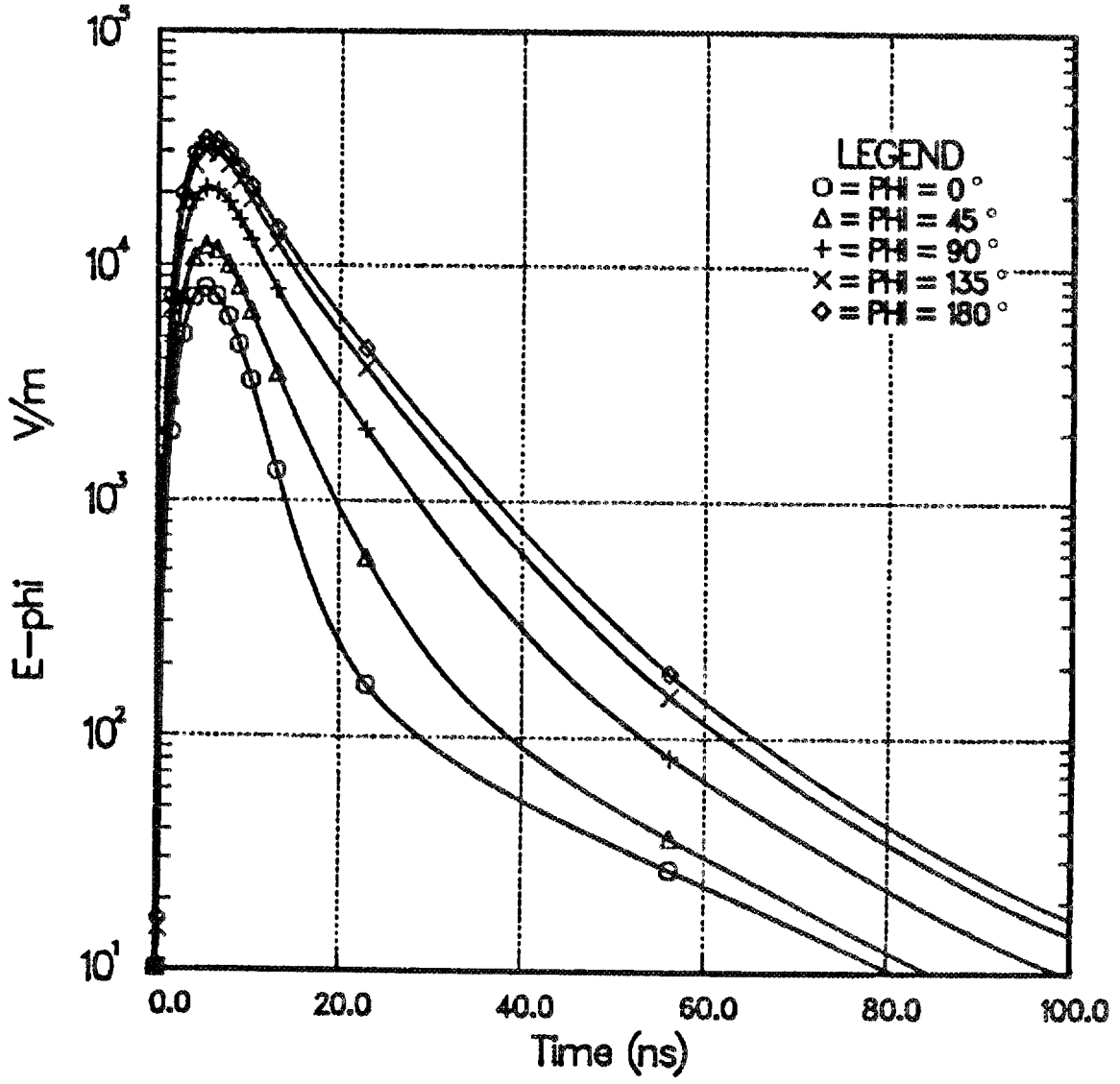

Figure 7. H = 400 km. Observer at GR = 233.5 km.
CHAP THETA = 30°.

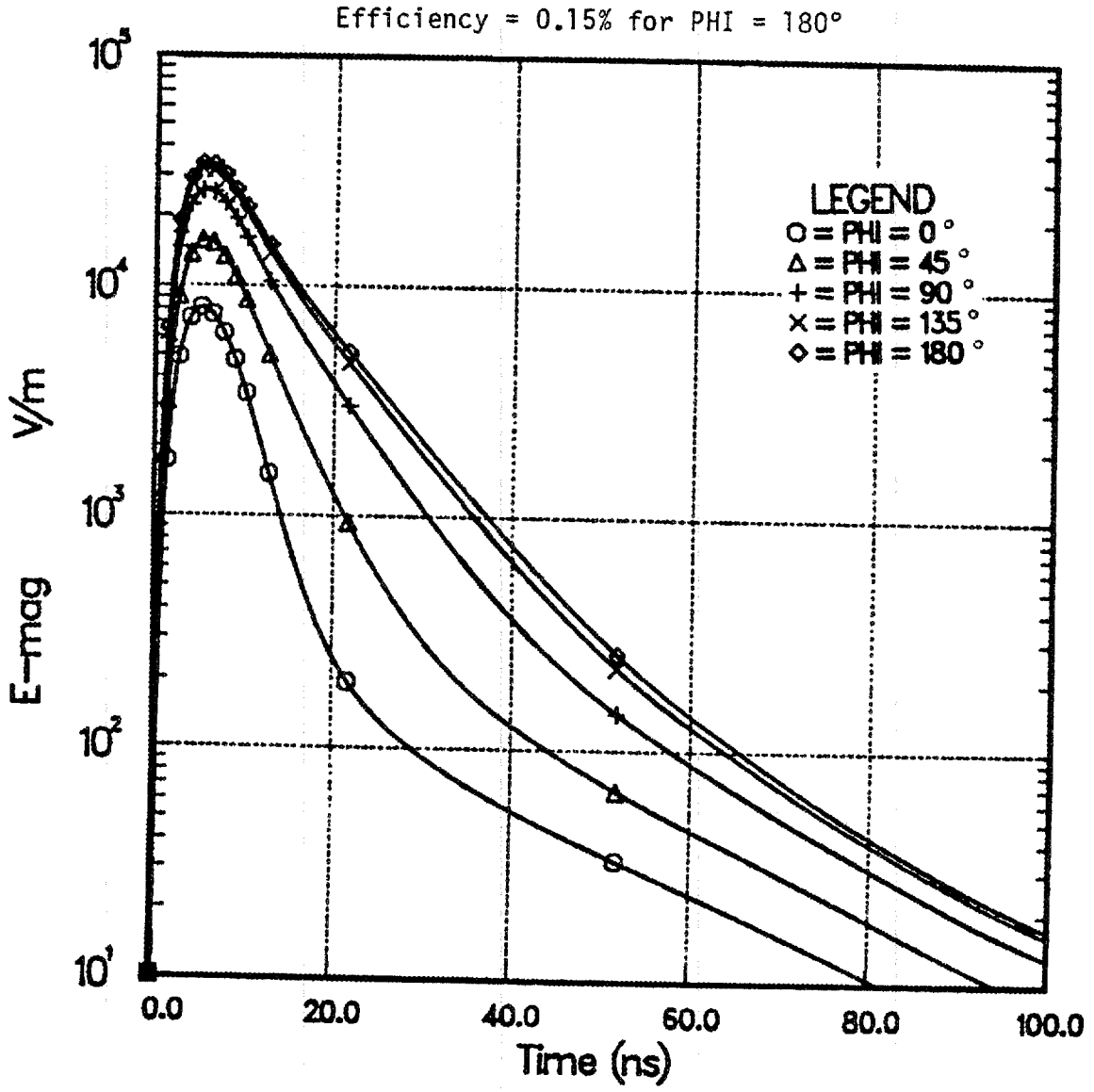

Figure 8. H = 400 km. Observer at GR = 233.5 km. CHAP THETA = 30°.

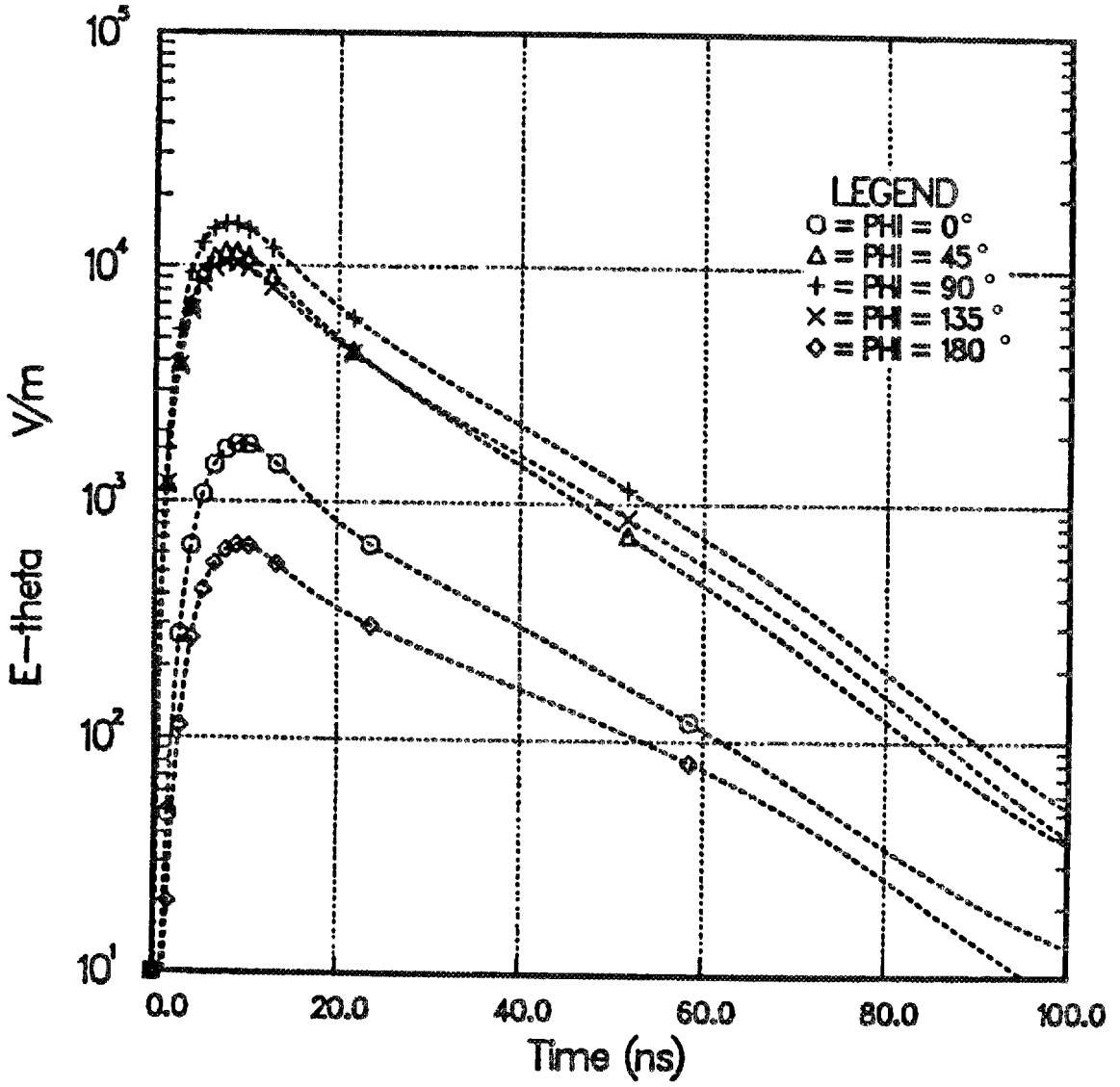

Figure 9. H = 400 km. Observer at GR = 500.6 km. CHAP THETA = 50°.

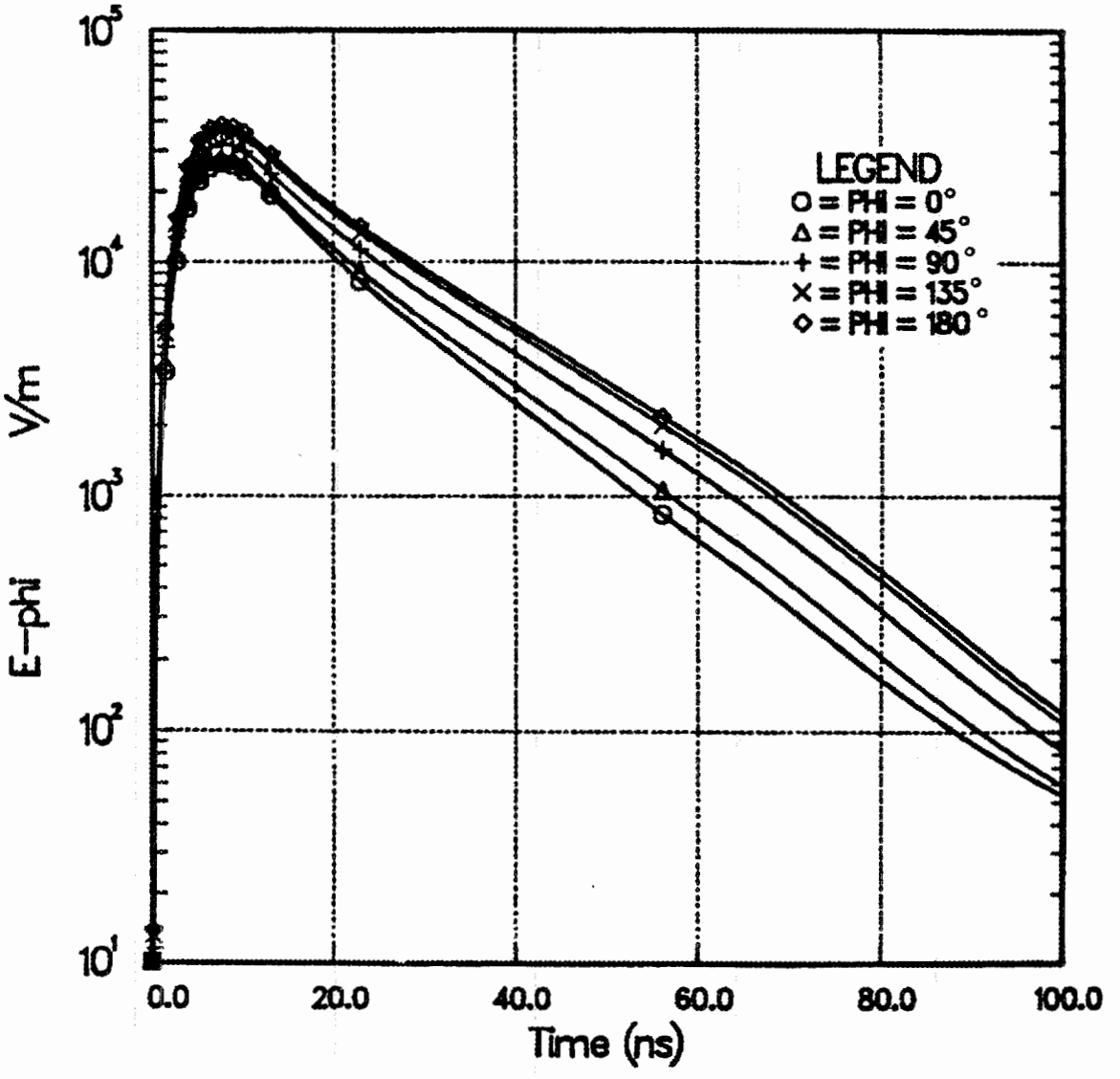

Figure 10. H = 400 km. Observer at GR = 500.6 km.
CHAP THETA = 50°.

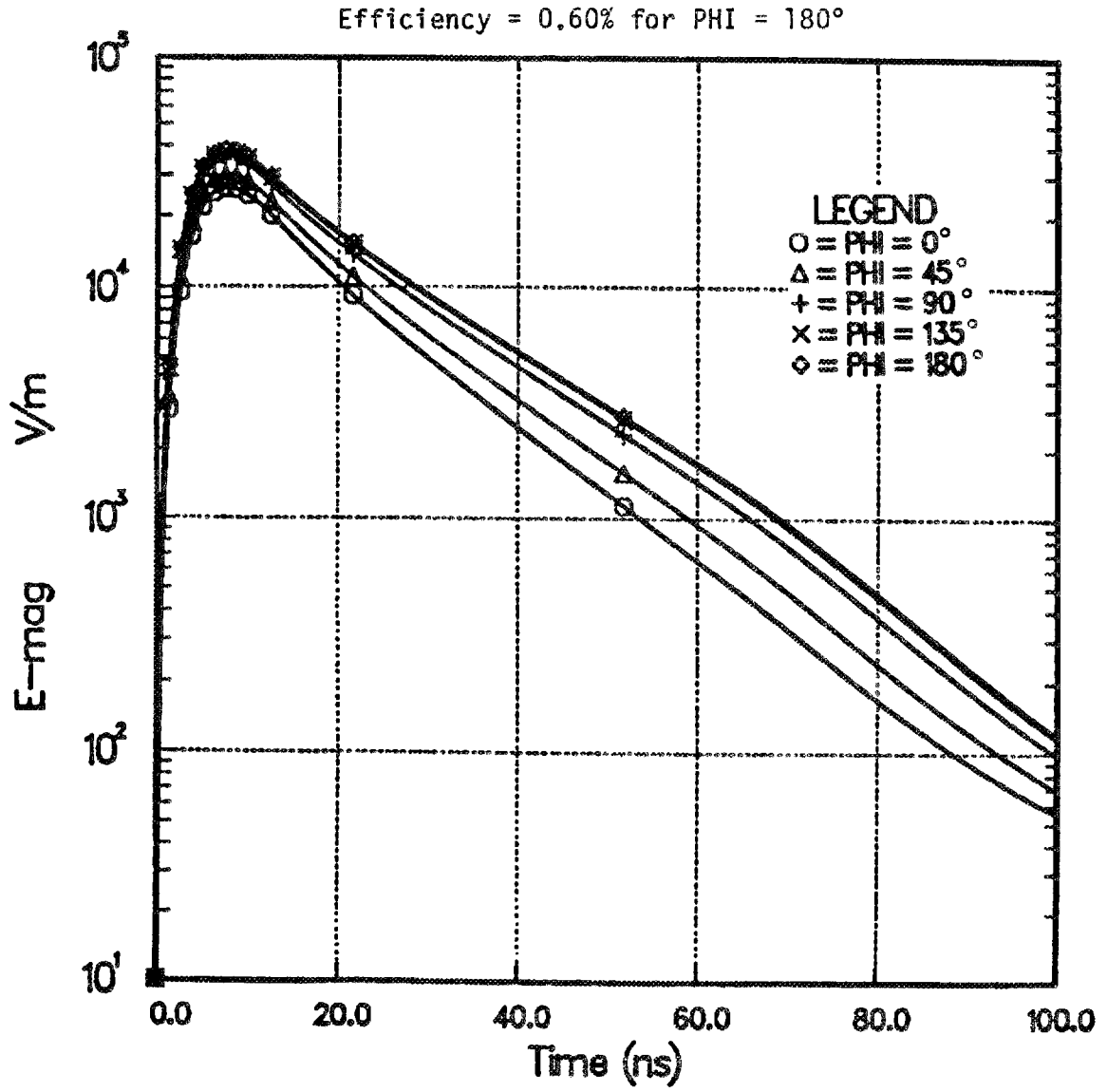

Figure 11. H = 400 km. Observer at GR = 500.6 km. CHAP THETA = 50°.

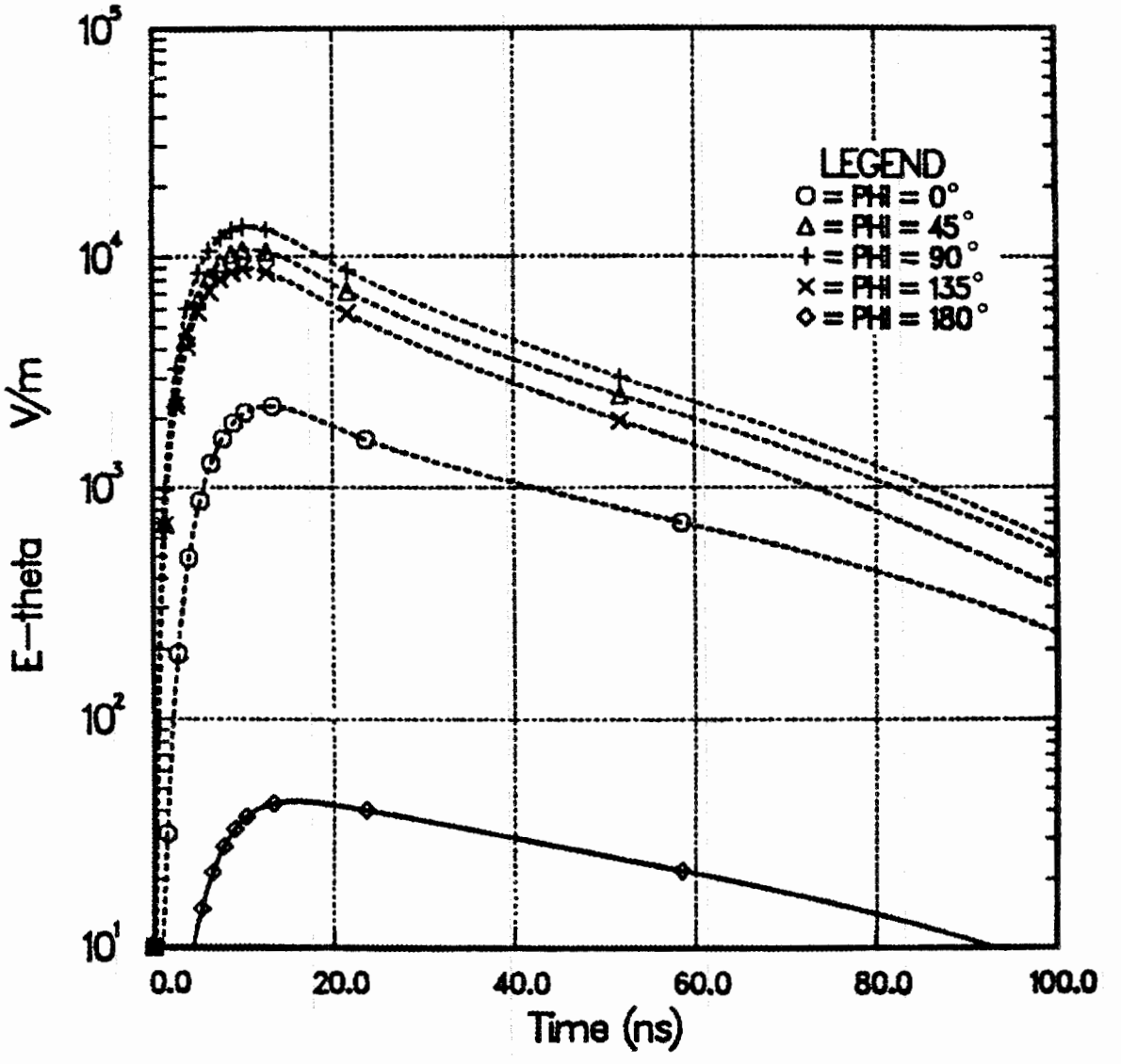

Figure 12. H = 400 km. Observer at GR = 776.6 km. CHAP THETA = 60°.

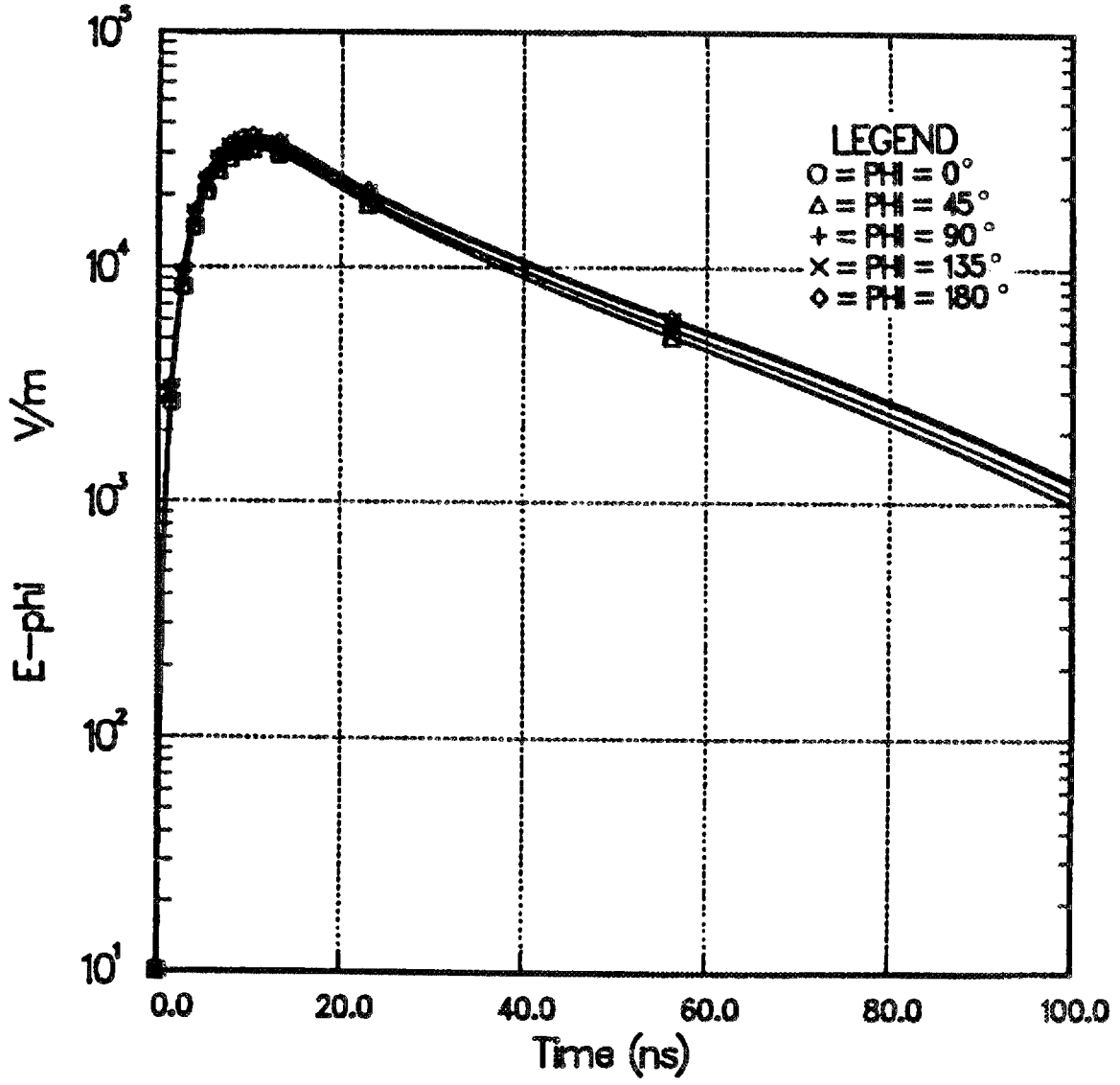

Figure 13. H = 400 km. Observer at GR = 776.6 km. CHAP THETA = 60°.

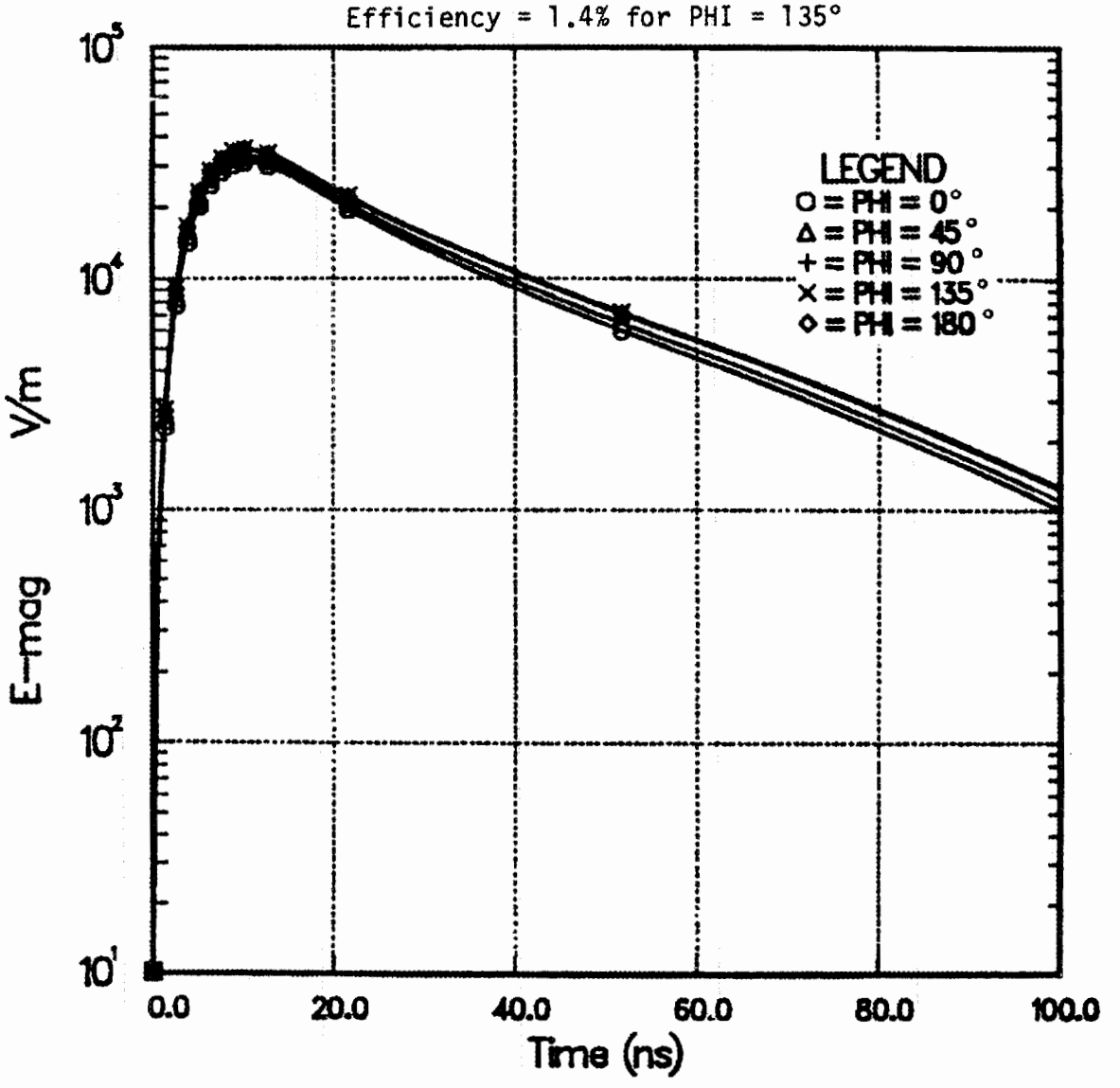

Figure 14. H = 400 km. Observer at GR = 776.6 km. CHAP THETA = 60°.

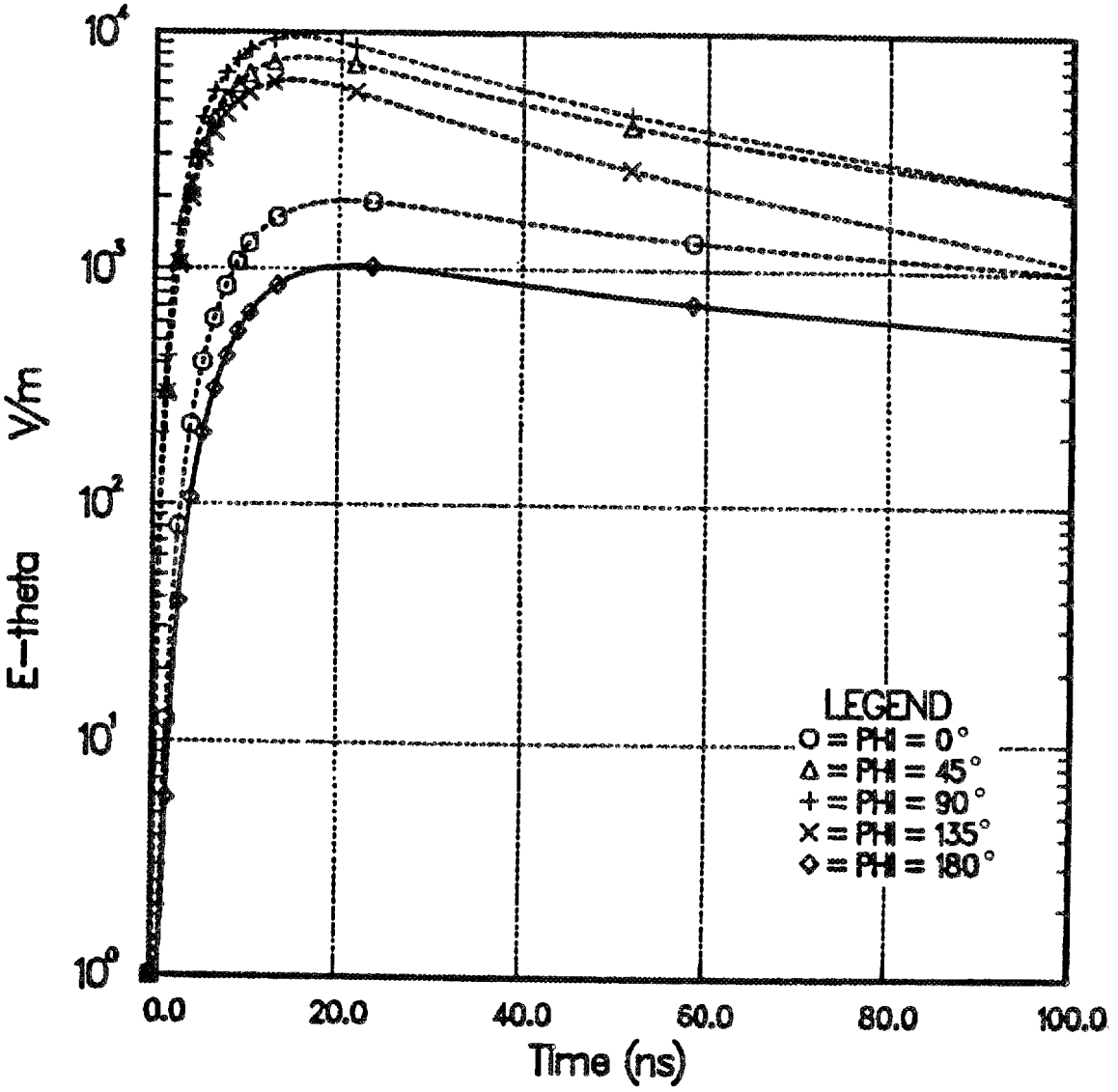

Figure 15. H = 400 km. Observer at GR = 1356.0 km. CHAP THETA = 68°.

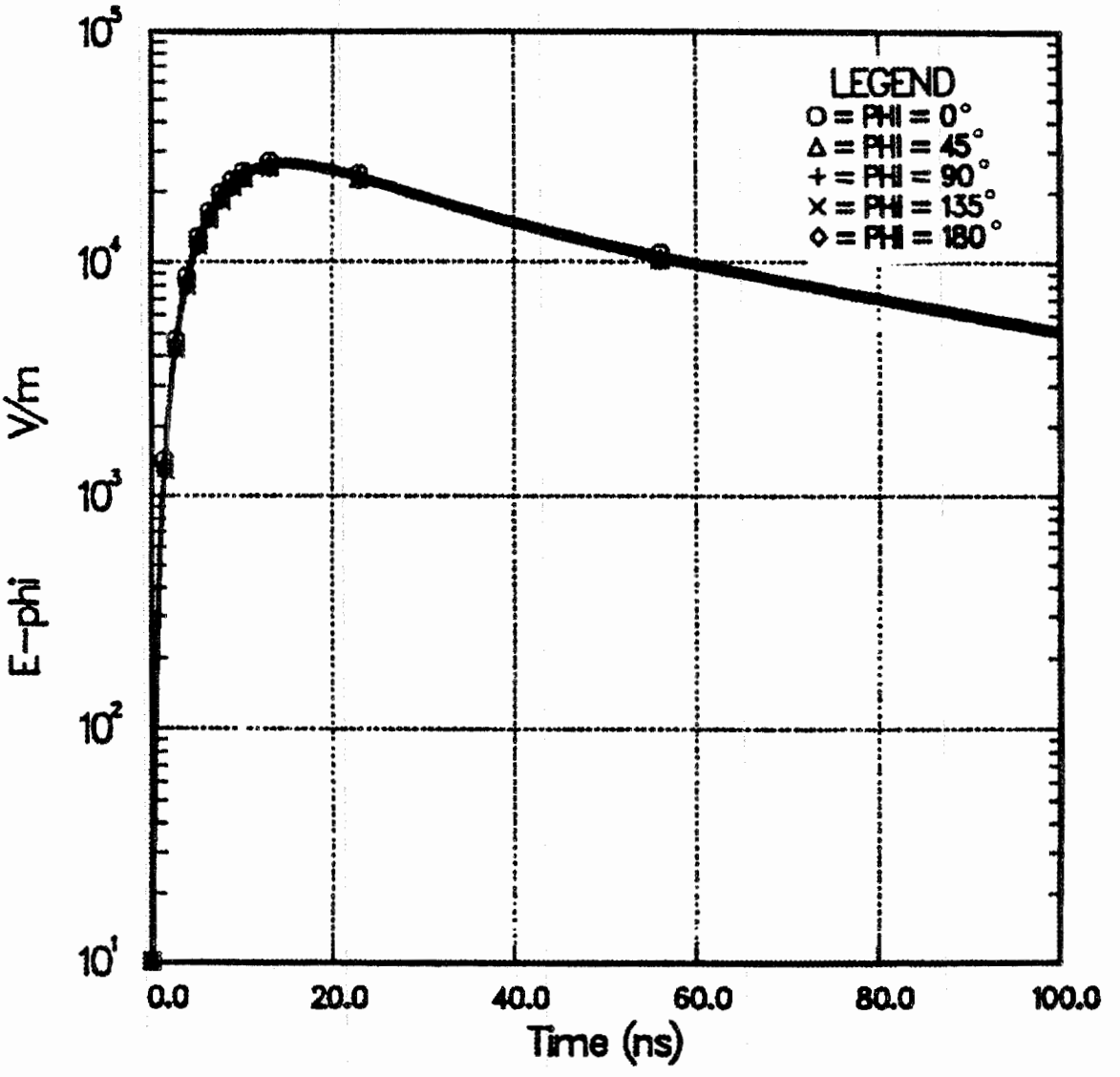

Figure 16. H = 400 km. Observer at GR = 1356.0 km. CHAP THETA = 68°.

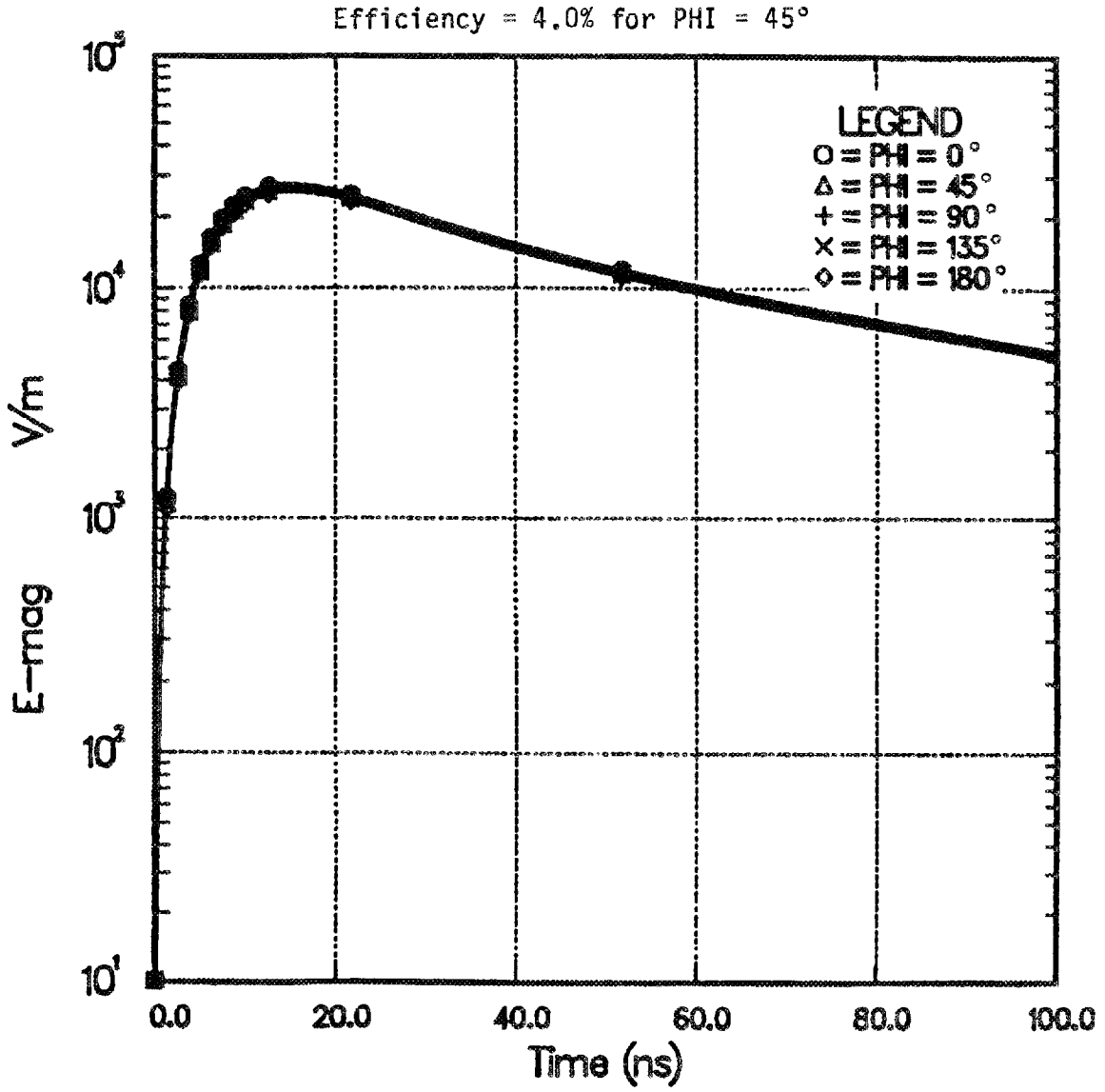

Figure 17. H = 400 km. Observer at GR = 1356.0 km. CHAP THETA = 68°.

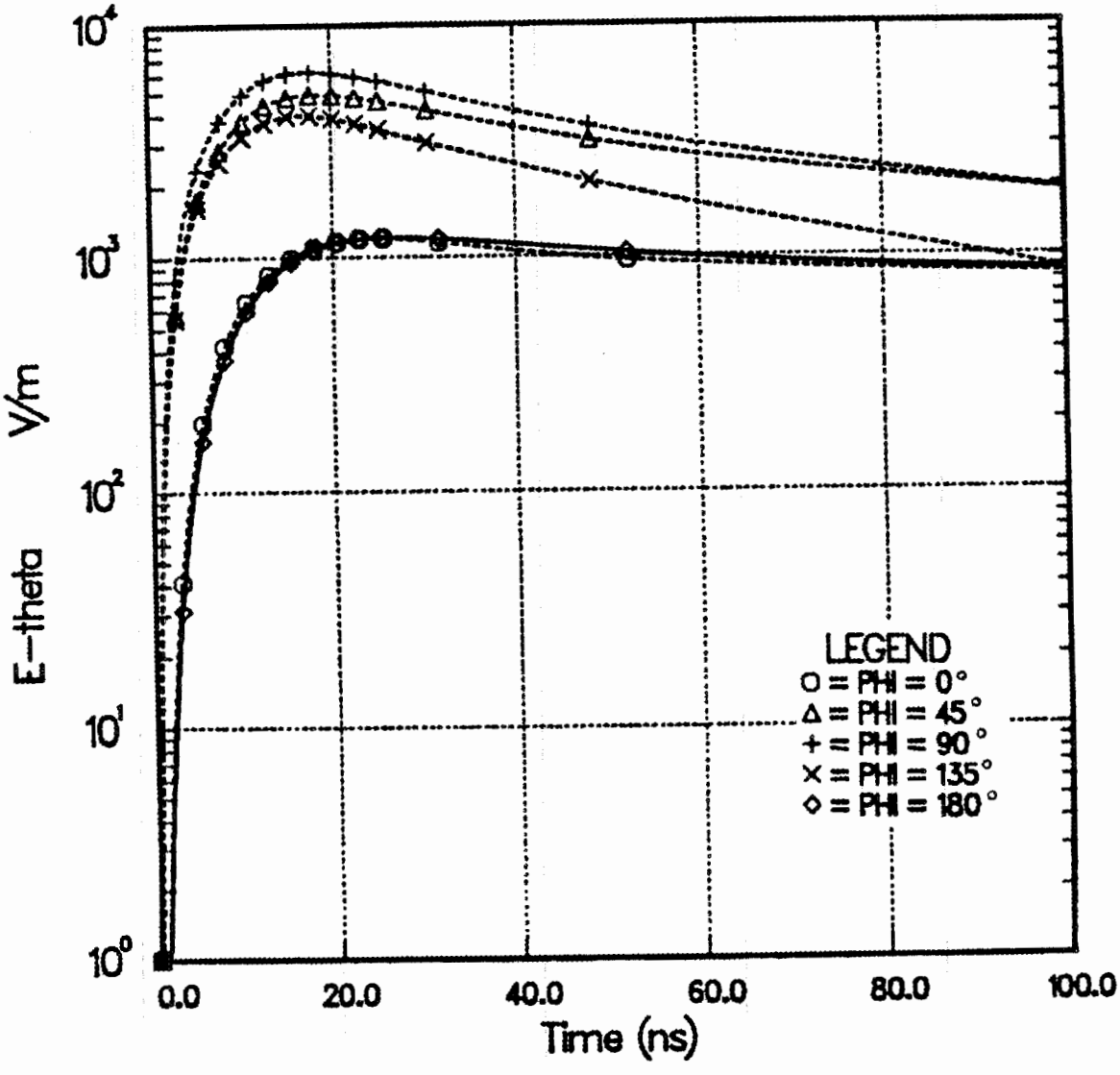

Figure 18. H = 400 km. Observer at GR = 2201.0 km, on horizon. CHAP THETA = 70.2°.

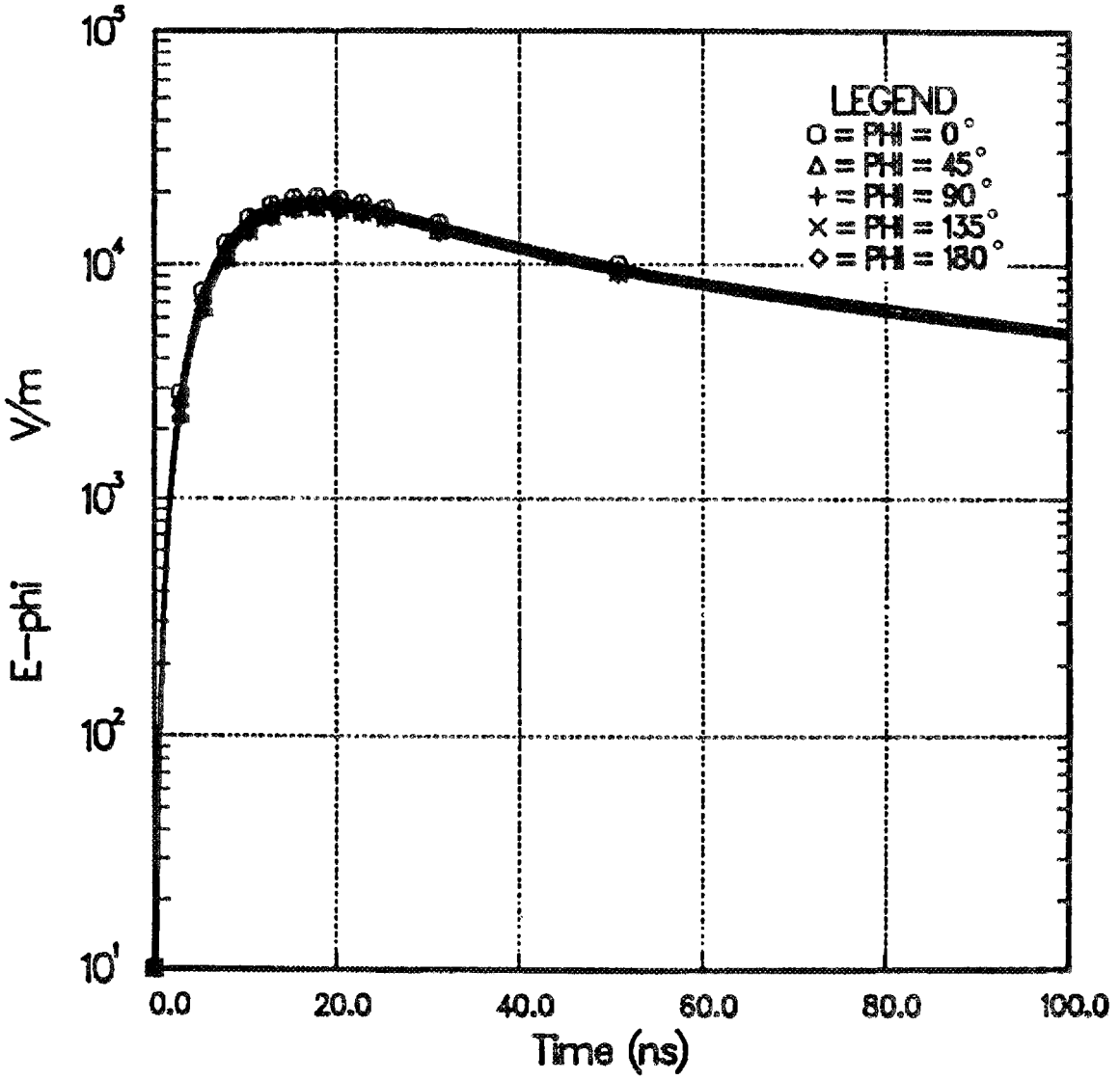

Figure 19. H = 400 km. Observer at GR = 2201.0 km, on horizon. CHAP THETA = 70.2°.

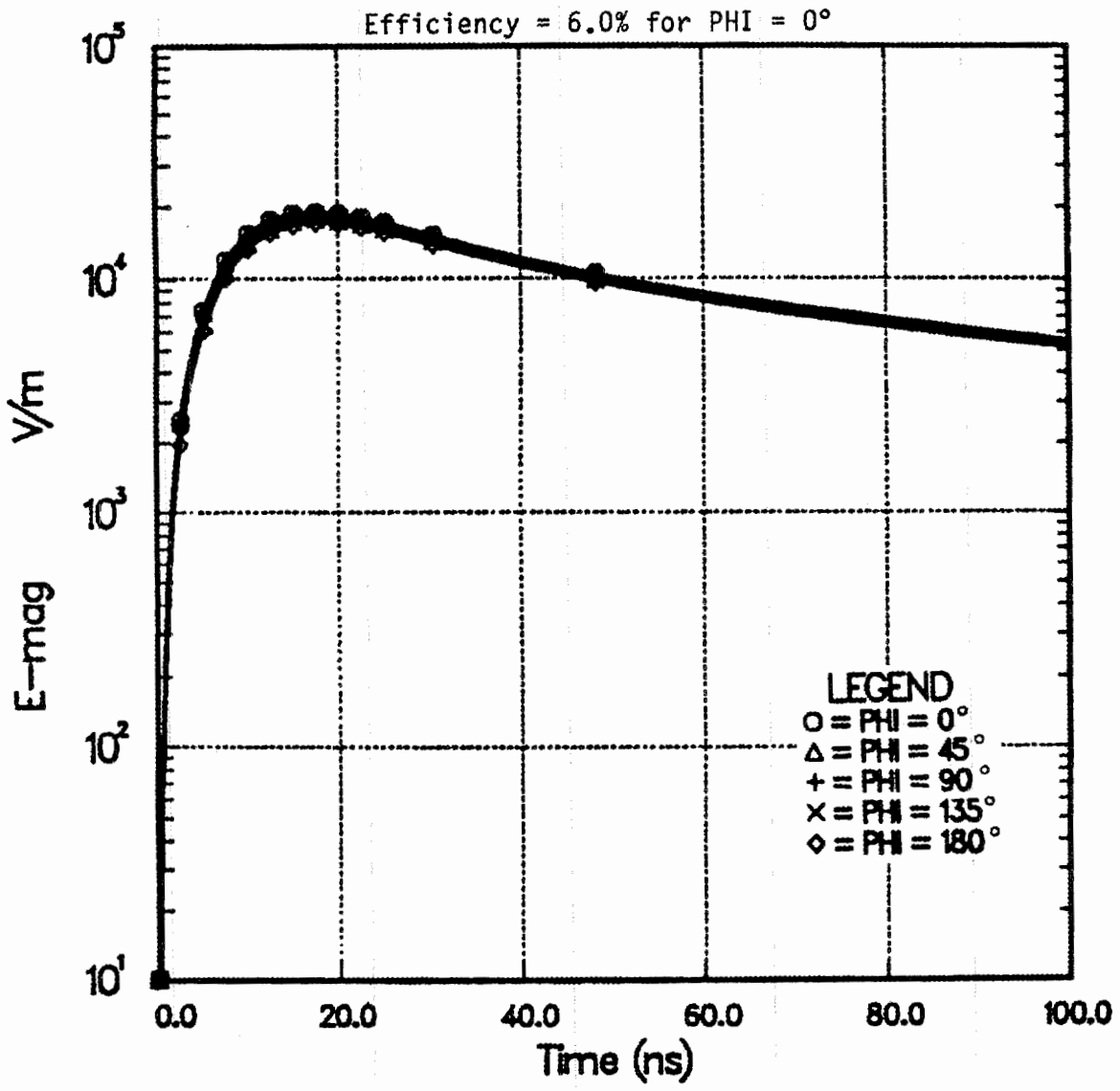

Figure 20. H = 400 km. Observer at GR = 2201.0 km, on horizon. CHAP THETA = 70.2°.

Note that the pulse is shorter for smaller ground range. This again comes from the higher air conductivity that builds up rapidly at the lower desaturation altitudes for intense gamma flux. The shorter pulse at smaller ground ranges contributes to inefficiency at these ranges.

Note that E_ϕ is considerably larger than E_θ for most observers. This comes from the rather large dip angle of the geomagnetic field, which makes its vertical component considerably larger than its horizontal component.

Finally, note that the peak of the pulse occurs at a time of the order of 10^{-8} second after onset, or a little earlier at small ground ranges. As stated in Section 3.2, this time delay comes from the finite time required by the Compton electrons to acquire a significant transverse velocity. We conclude that use of zero rise-time for the gamma pulse is an acceptable approximation for the cases considered here.

3.5 RESULTS OF CHAP CALCULATION FOR 200 KM HEIGHT OF BURST

As an excursion from the foregoing cases, we ran one CHAP calculation for a height of burst of 200 km. This was for $\theta_C = 60°$, $\phi_C = 180°$, corresponding to an observer at a ground range of 365 km to the south of GZ. The results are shown in figures 21 through 23. Note that the electric field is almost entirely E_ϕ (westward horizontal in this case), and that the peak value of E_ϕ is approximately 50 kV/m. The pulse is, of course, quite short for this strongly saturated case.

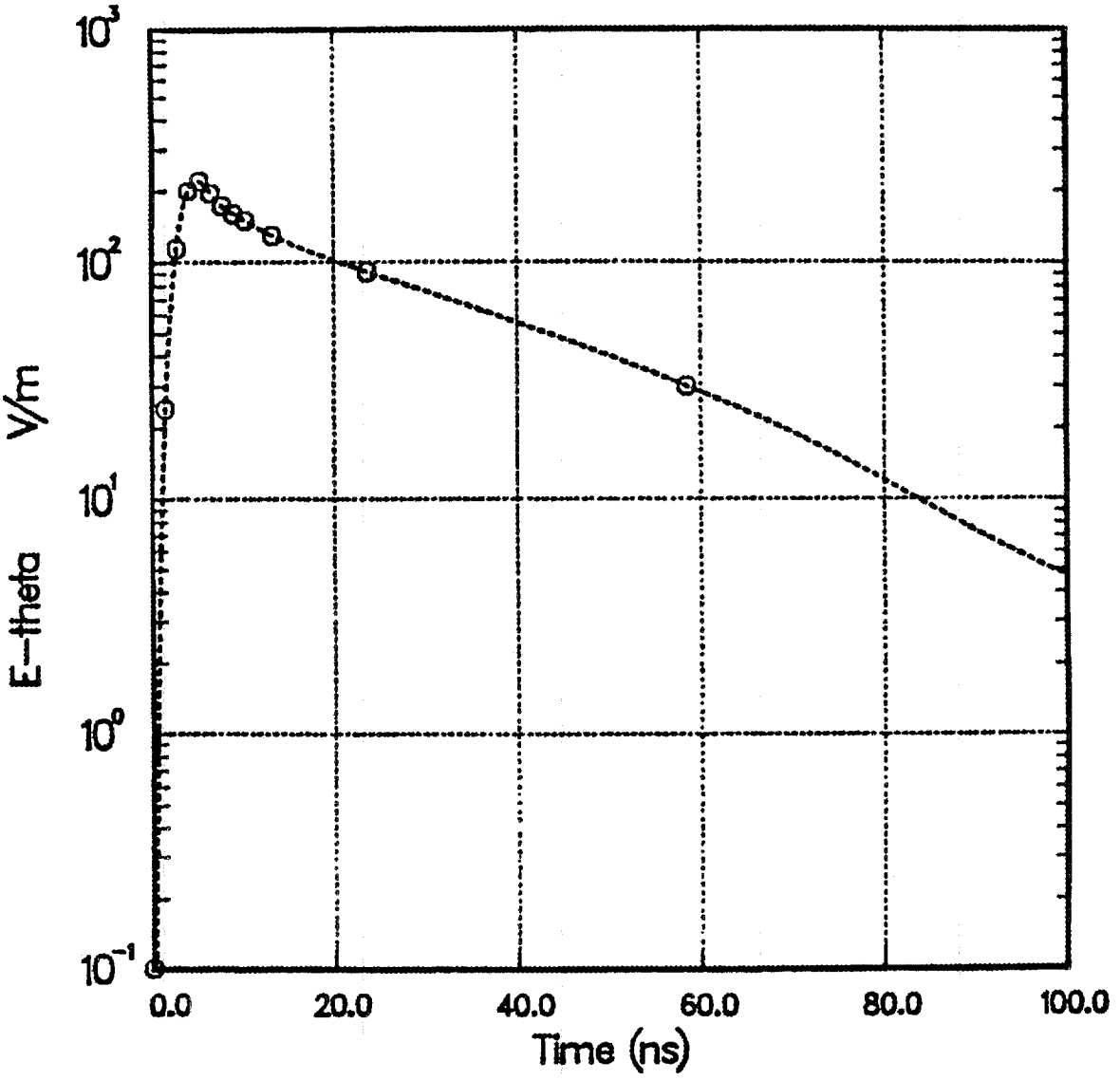

Figure 21. H = 200 km. Observer at GR = 365 km. CHAP THETA = 60°. PHI = 180°.

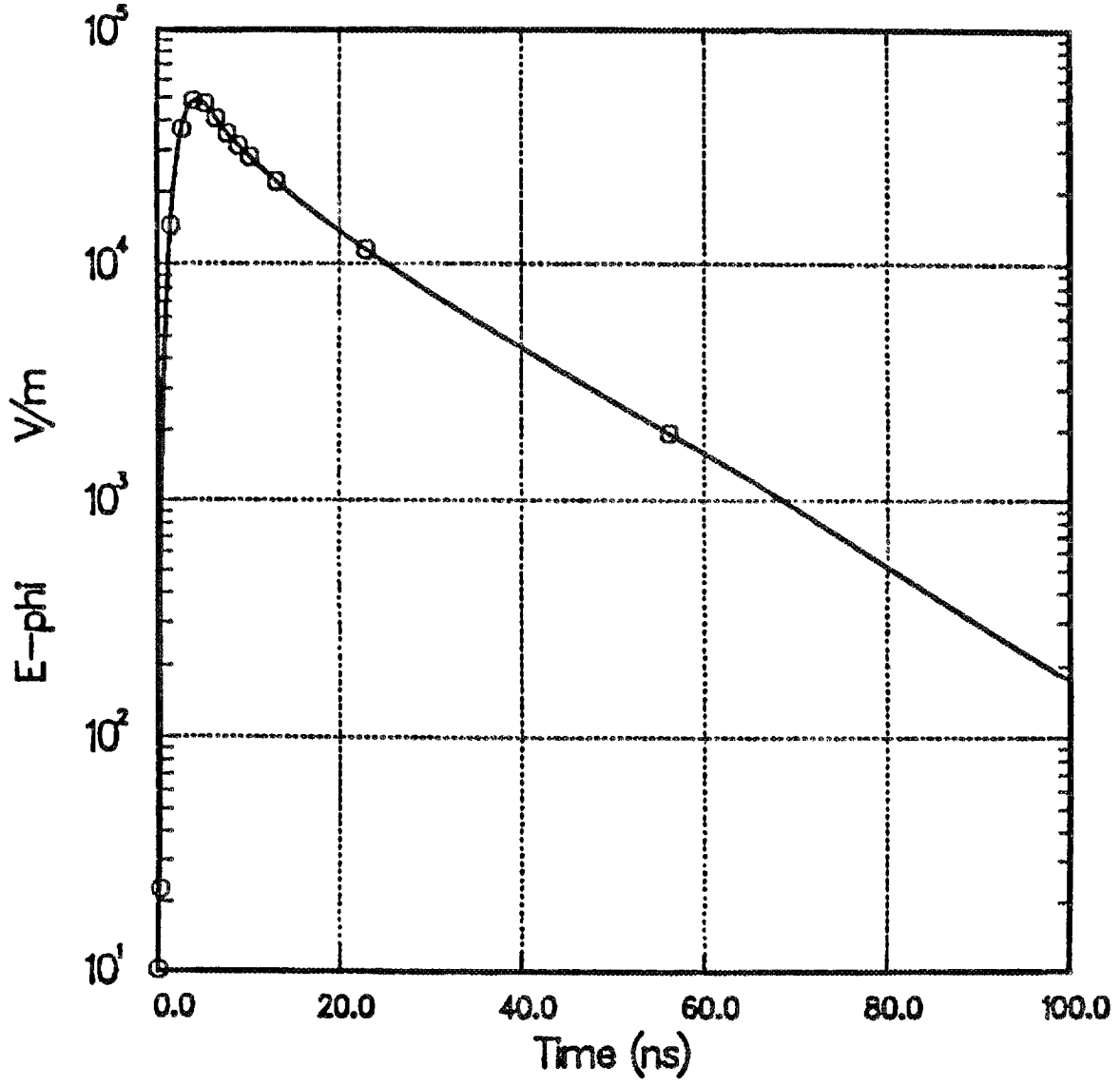

Figure 22. H = 200 km. Observer at GR = 365 km. CHAP THETA = 60°. PHI = 180°.

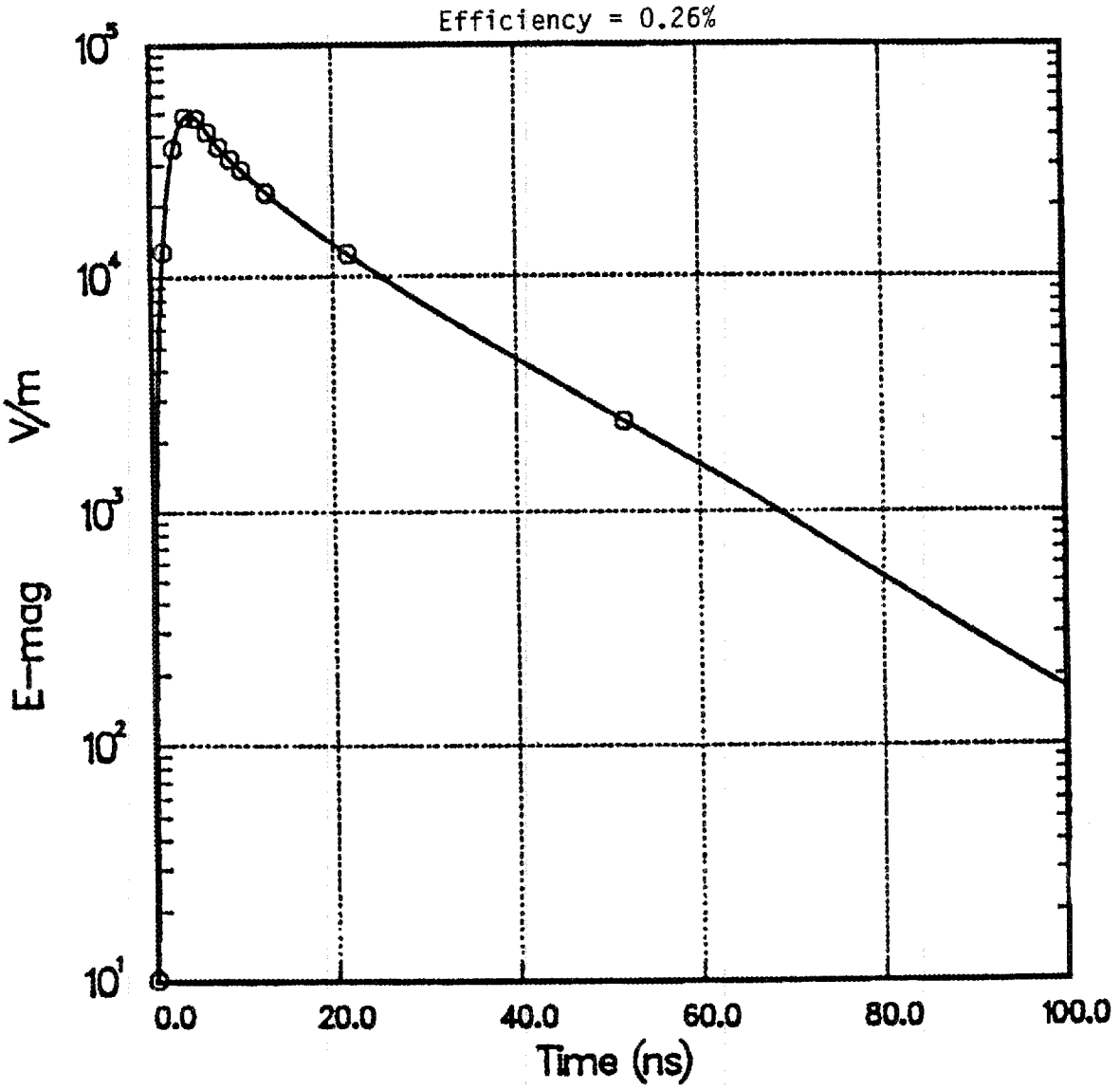

Figure 23. H = 200 km. Observer at GR = 365 km. CHAP THETA = 60°. PHI = 180°.

SECTION 4
ANALYTICAL FITS TO 400 KM ENVIRONMENTS

In order to provide environment data suitable for use in numerical calculation of the coupling of the HEMP to electrical and electronic systems, and to provide for interpolation between the observers in the CHAP calculations, we have made analytical fits to the CHAP results for 400 km height of burst. The method of using these fits is explained here. Input constants for the formulae are:

$$R_e = 6371 \text{ km} = \text{earth radius} ; \tag{48}$$

$$H = 400 \text{ km} = \text{burst height} ; \tag{49}$$

$$\chi_c = 36.05^\circ = \text{magnetic colatitude of GZ} . \tag{50}$$

The user begins by selecting an observer at:

$$GR = \text{ground range, km} ; \tag{51}$$

$$\phi_c = \text{magnetic azimuth, } -\pi < \phi_c \leq \pi . \tag{52}$$

Note that ϕ_c is the magnetic azimuth at GZ of the great circle passing through GZ and the observer. An observer on the same magnetic latitude line as GZ but at a large distance to the east has a ϕ_c somewhat less than 90°. The user then calculates:

$$\Psi_0 = GR/R_e = \text{geocentric angle of observer ;} \quad (53)$$

$$\theta_c = \arctan\left[\frac{R_e \sin\Psi_0}{H + R_e(1 - \cos\Psi_0)}\right] = \text{CHAP } \theta \text{ ;} \quad (54)$$

$$\theta_0 = \frac{\pi}{2} - (\theta_c + \Psi_0) = \text{burst elevation angle at observer .} \quad (55)$$

The next step is to locate the source region for this observer. This is done on the assumption that the height of the source region is 40 km. This is correct for observers near the horizon; at smaller ground ranges the height makes little difference. Calculate:

$$\Psi_s = \arcsin\left[\left(\frac{R_e + H}{R_e + 40}\right) \sin\theta_c\right] - \theta_c = \text{geocentric angle of source region ;} \quad (56)$$

$$\theta_s = \frac{\pi}{2} - (\theta_c + \Psi_s) = \text{burst elevation angle at source region ;} \quad (57)$$

$$\chi_s = \chi_c - \Psi_s \cos\phi_c = \text{colatitude of source region ;} \quad (58)$$

$$\phi_s = \phi_c + \Psi_s \cot\chi_c \sin\phi_c = \text{azimuth of ray in source region .} \quad (59)$$

The last two equations here are approximate, correct to first order in Ψ_s. These results are then used to calculate the components of the local geomagnetic field in the source region in the CHAP coordinate system. These are:

$$b_r = \sin\chi_s \cos\theta_s \cos\phi_s + 2\cos\chi_s \sin\theta_s \; ; \tag{60}$$

$$b_\theta = \sin\chi_s \sin\theta_s \cos\phi_s - 2\cos\chi_s \cos\theta_s \; ; \tag{61}$$

$$b_\phi = -\sin\chi_s \sin\phi_s \; . \tag{62}$$

The components of the HEMP electric field are then:

$$E_\theta = F(T) b_\phi + G(T) b_\theta b_r \; ; \tag{63}$$

$$E_\phi = -F(T) b_\theta + G(T) b_\phi b_r \; . \tag{64}$$

The first term in each case is the magnetic dipole part, and the second term is the electric quadrupole part. The time functions are, for $T \geq 0$:

$$F(T) = [1-e^{-(T/T_d)^2}][A_1 e^{-\beta_1(T-T_d)} + (A_{21}+A_{22}\sqrt{b_\theta^2 + b_\phi^2})e^{-\beta_2(T-T_d)}] \; ; \tag{65}$$

$$G(T) = [1 - e^{-(T/T_q)^2}]A_q e^{-\beta_q(T-T_q)} \; . \tag{66}$$

The parameters in these formulae are listed in table 1 as a function of ground range. Linear interpolation is to be used between entries in the table.

The first factor in each of the time functions governs the rise of the fields. In both cases, this factor starts out proportional to T^2, which is proper for the magnetic dipole part. The electric quadrupole part starts out as T^3, but for simplicity we have used the same form. The quadrupole part is generally small compared with the dipole part.

Table 1. Fit parameters for H = 400 km. The units of T_d and T_q are shakes (1 shake = 10^{-8} sec). The units of β_1, β_2 and β_q are shake^{-1}. The units of A_1, A_{21}, A_{22} and A_q are 10^4 V/m.

GR	T_d	β_1	β_2	A_1	A_{21}	A_{22}	T_q	β_q	A_q
0	0.540	3.83	1.000	2.838	0.100	0.166	0.590	3.22	0.0785
100	0.485	2.94	0.970	2.793	0.130	0.670	0.520	1.50	0.086
200	0.450	2.24	0.895	2.714	-0.098	0.998	0.480	1.00	0.097
300	0.460	1.74	0.745	2.595	-0.248	1.019	0.500	0.84	0.110
400	0.500	1.42	0.560	2.437	-0.311	0.986	0.590	0.69	0.126
500	0.545	1.19	0.435	2.273	-0.295	0.921	0.670	0.57	0.144
600	0.590	1.00	0.348	2.120	-0.057	0.737	0.716	0.44	0.161
700	0.636	0.853	0.285	2.000	+0.527	0.355	0.762	0.33	0.169
800	0.680	0.740	0.240	1.900	0.845	0.139	0.810	0.25	0.171
900	0.724	0.655	0.200	1.810	0.919	0.070	0.858	0.190	0.171
1000	0.768	0.590	0.170	1.730	0.948	0.023	0.905	0.148	0.169
1100	0.814	0.543	0.148	1.652	0.959	-0.010	0.953	0.125	0.167
1200	0.860	0.507	0.130	1.574	0.967	-0.041	1.000	0.108	0.164
1300	0.905	0.475	0.115	1.500	0.965	-0.065	1.048	0.088	0.161
1400	0.945	0.457	0.100	1.438	0.963	-0.088	1.096	0.078	0.157
1500	0.990	0.448	0.092	1.390	0.962	-0.110	1.140	0.070	0.154
1600	1.028	0.442	0.086	1.346	0.951	-0.126	1.182	0.066	0.151
1700	1.060	0.440	0.080	1.308	0.942	-0.145	1.223	0.062	0.147
1800	1.088	0.439	0.074	1.271	0.925	-0.159	1.260	0.059	0.144
1900	1.108	0.438	0.069	1.237	0.907	-0.172	1.292	0.056	0.141
2000	1.120	0.437	0.064	1.203	0.885	-0.182	1.320	0.053	0.138
2100	1.131	0.436	0.059	1.172	0.862	-0.191	1.338	0.050	0.135
2200	1.140	0.436	0.054	1.140	0.834	-0.198	1.350	0.047	0.132

For this reason we have used two decaying exponentials to fit the dipole part, but only one for the quadrupole part.

The dipole part was determined by fitting the CHAP E_ϕ at $\phi_c = 0°$ and 180°. The quadrupole part was determined by fitting the CHAP E_θ at $\phi_c = 0°$ or 180°, whichever was larger. The fields at all other azimuths are then fixed.

Fields calculated from the fits for the CHAP data points are shown in figures 24 through 35. The scale in these figures has been made the same as in figures 3 through 20, so that a Xerox copy of the present figures can be laid over the earlier ones to facilitate comparison. Comparison with the CHAP results shows that the fits are reasonably accurate down to about 10% of the peak value of the fields. This is all that was attempted, and should be sufficient for any reasonable application.

Recall that equations (36) and (37) can be used to decompose E_θ into vertical-upward and horizontal-radial parts. E_ϕ is already horizontal-azimuthal.

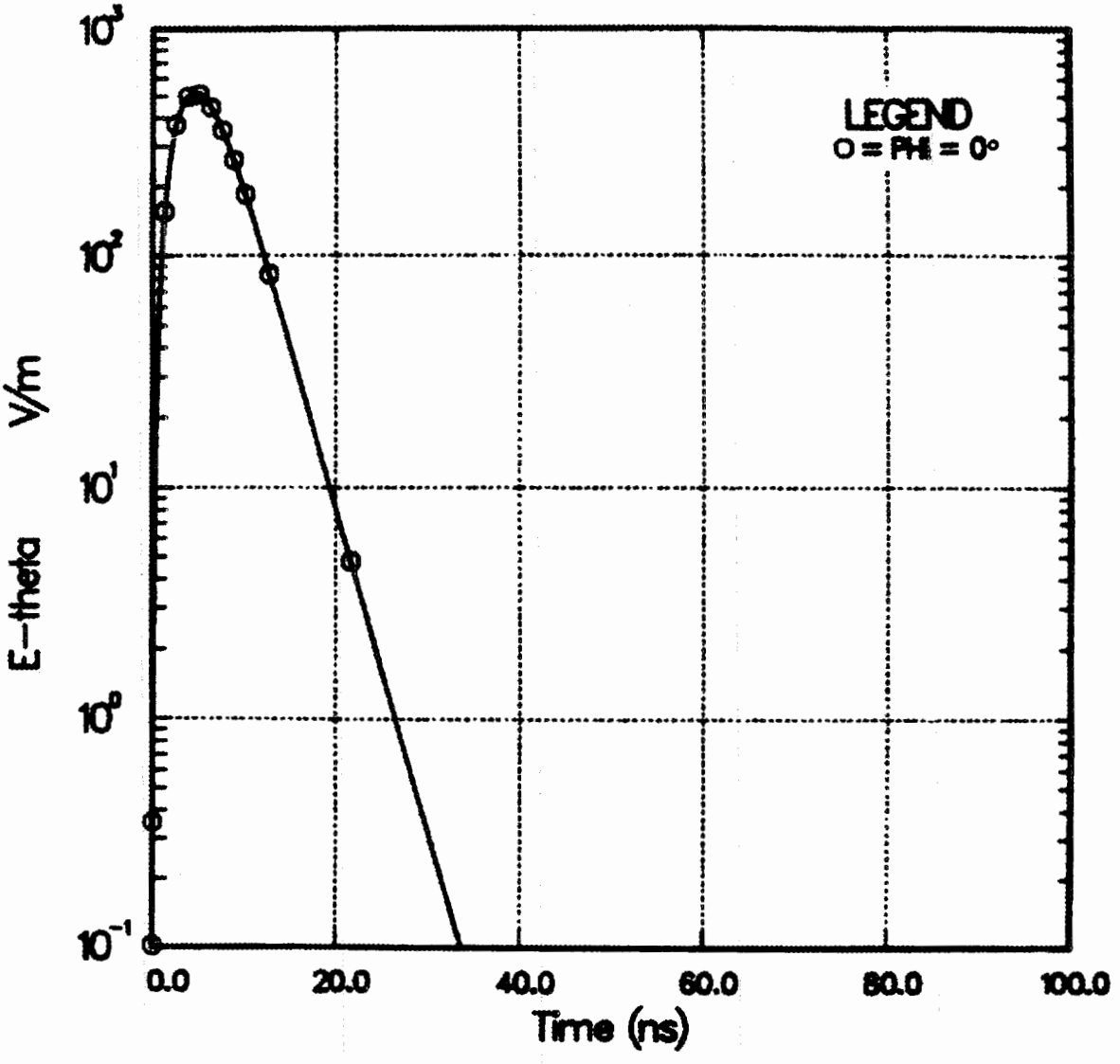

Figure 24. Fit to Figure 3. H = 400 km, GR = 0.

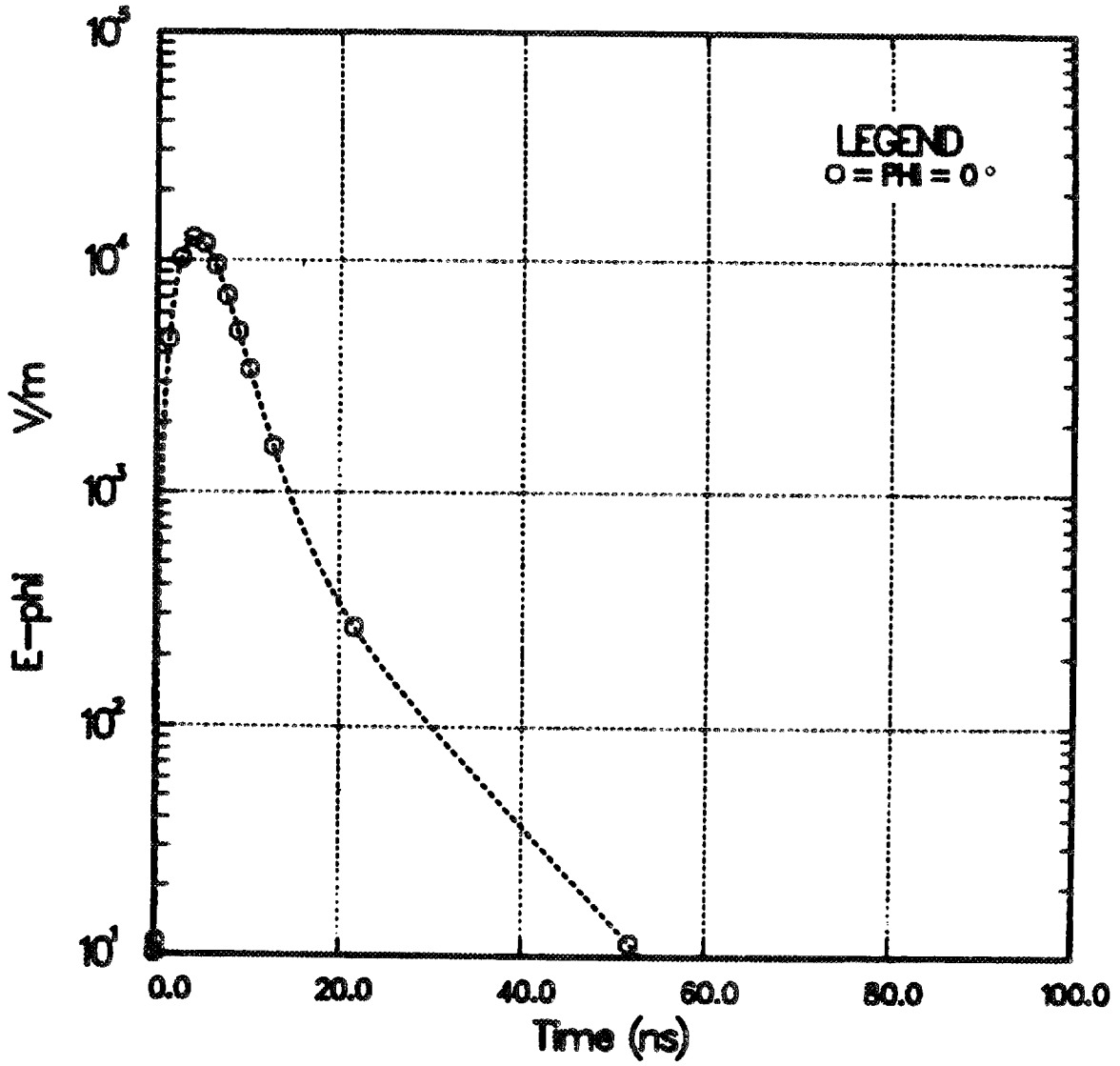

Figure 25. Fit to Figure 4. H = 400 km, GR = 0.

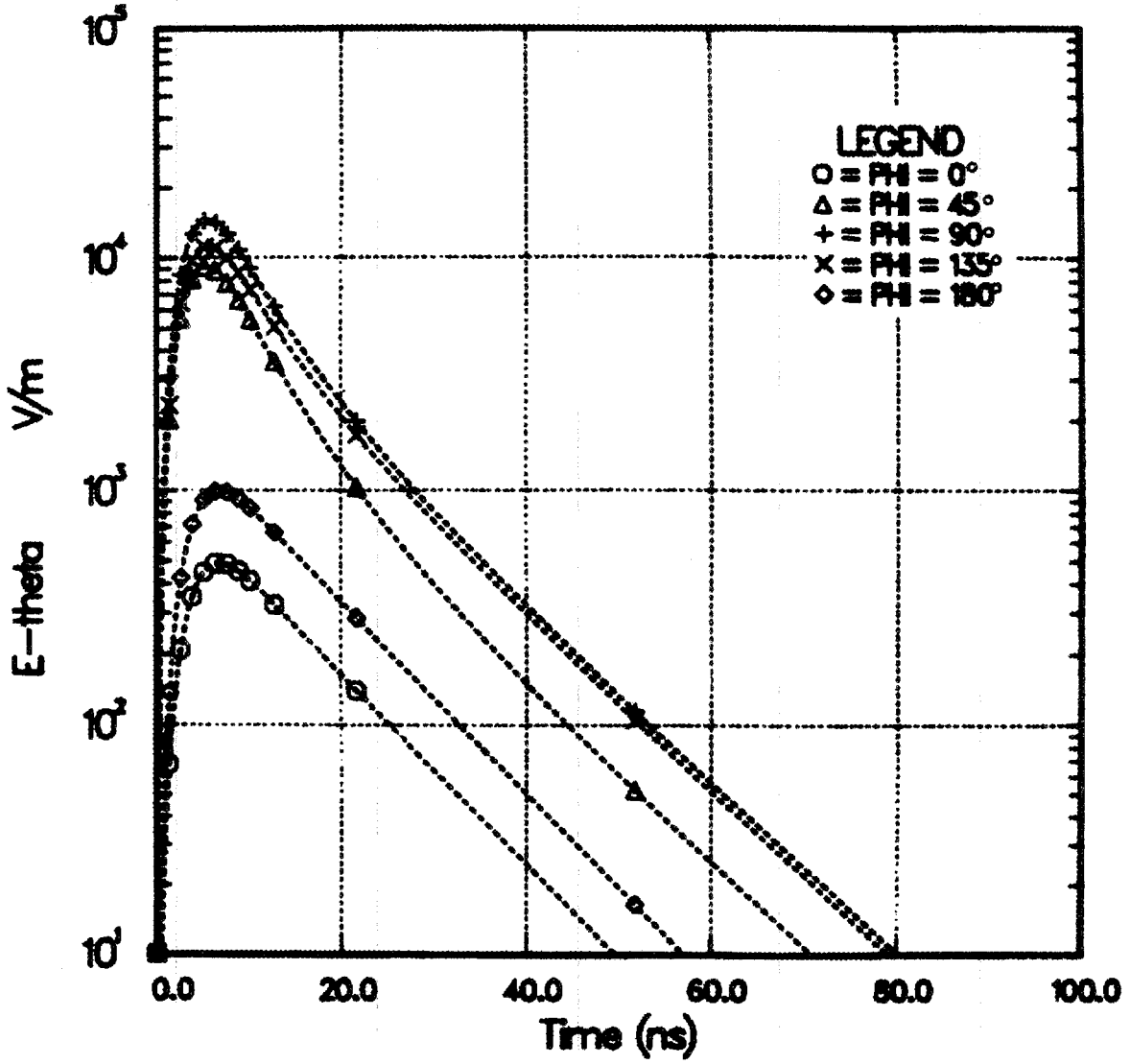

Figure 26. Fit to Figure 6. H = 400 km, GR = 233.5 km.

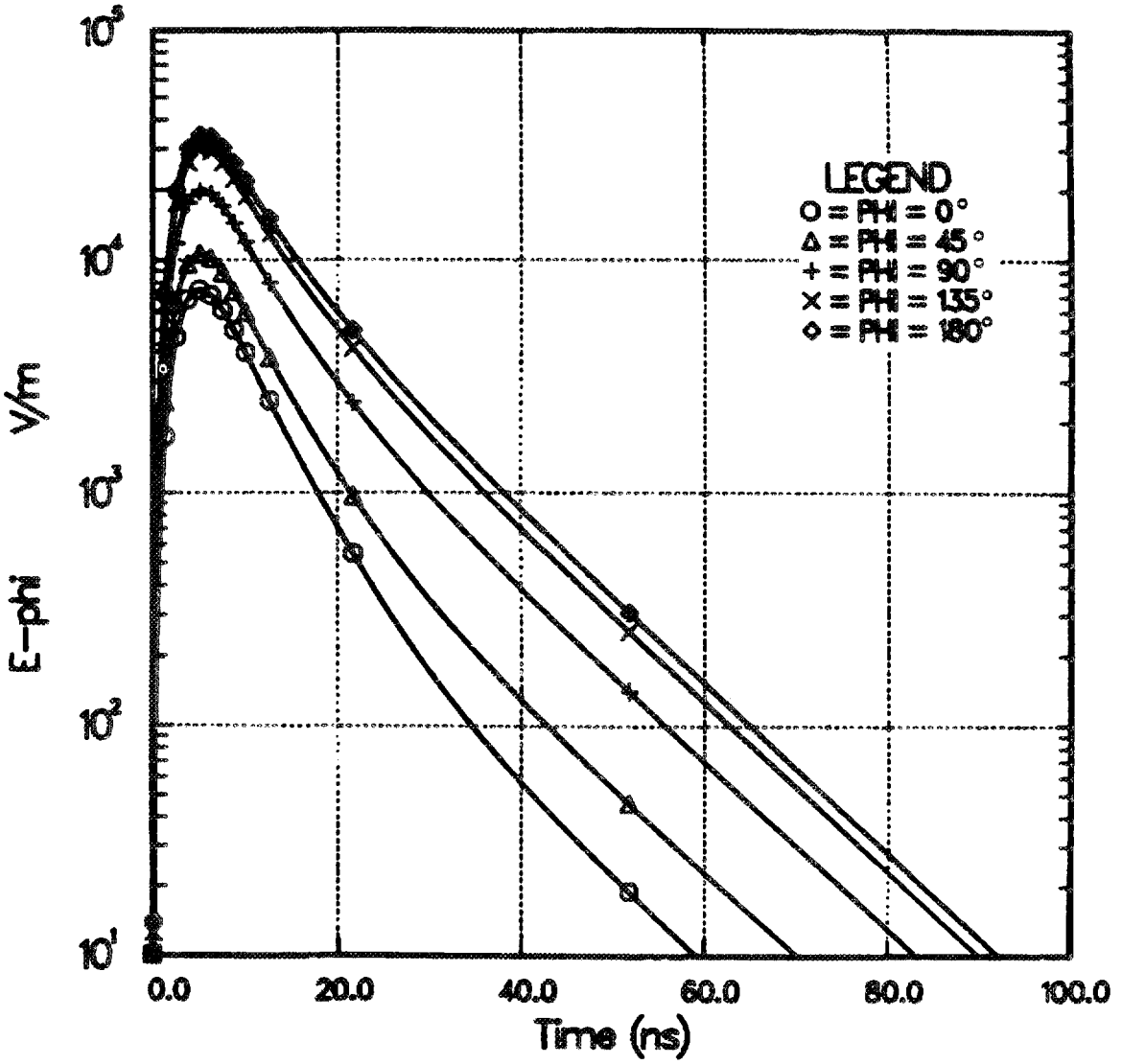

Figure 27. Fit to Figure 7. H = 400 km, GR = 233.5 km.

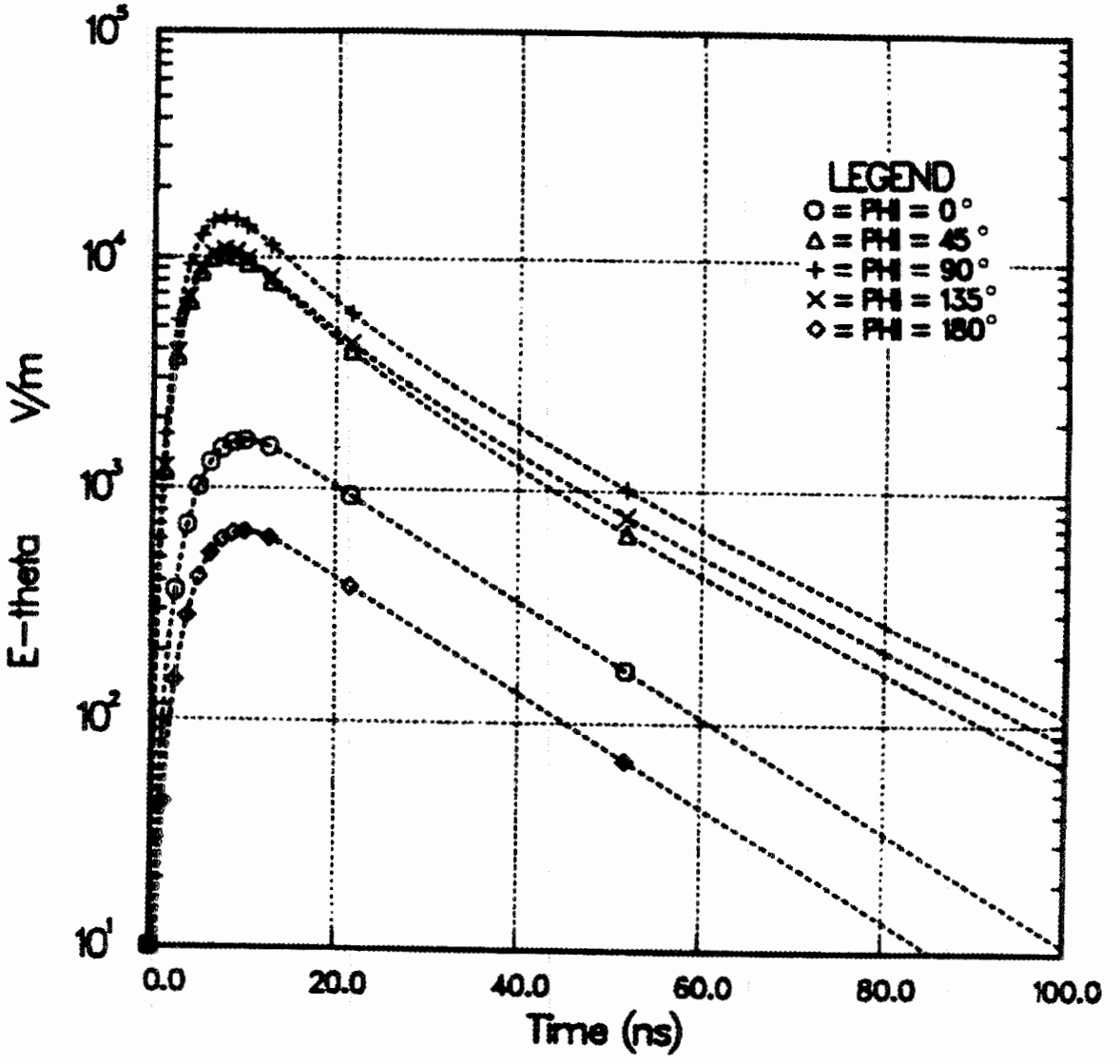

Figure 28. Fit to Figure 9. H = 400 km, GR = 500.6 km.

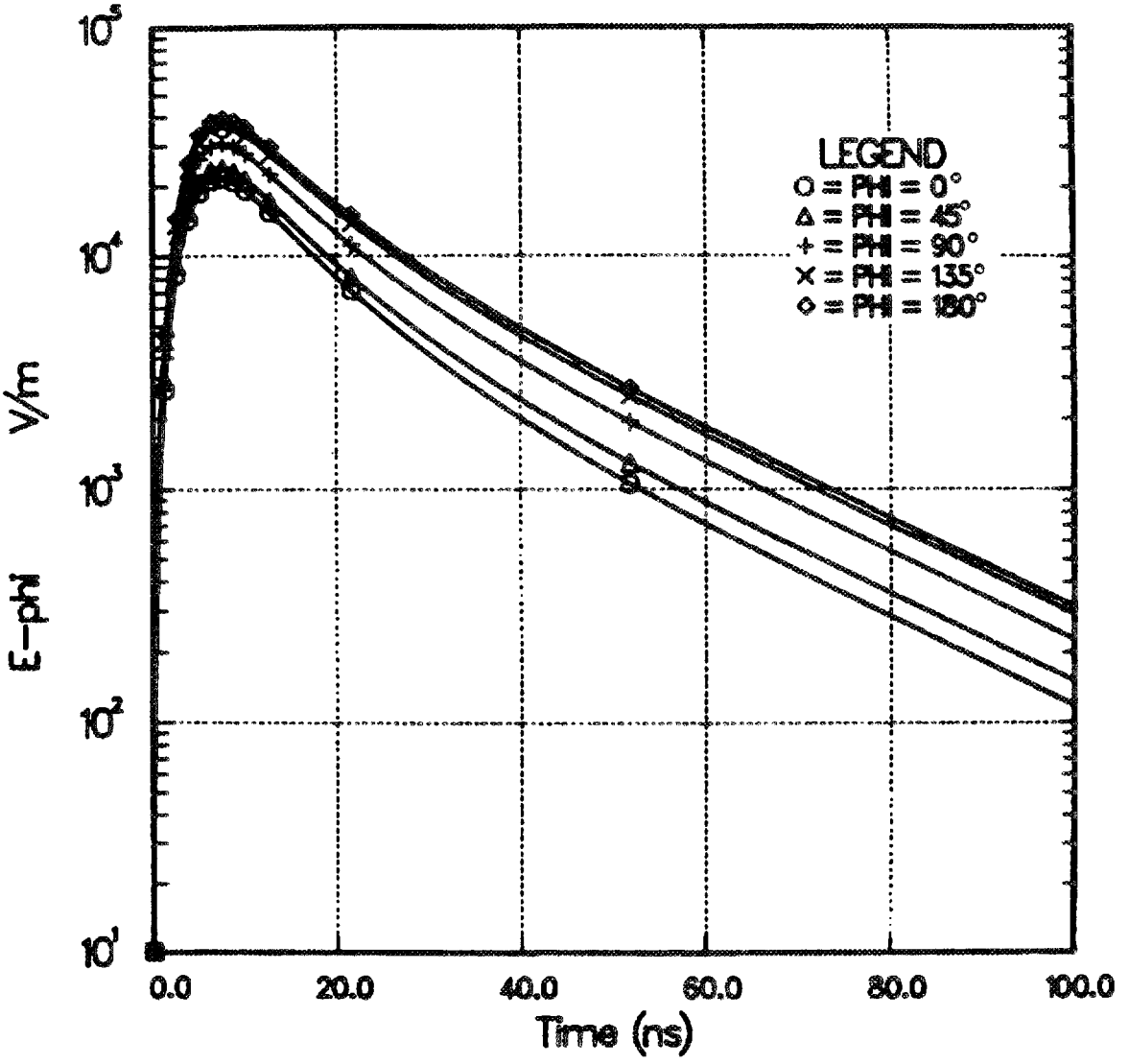

Figure 29. Fit to Figure 10. H = 400 km, GR = 500.6 km.

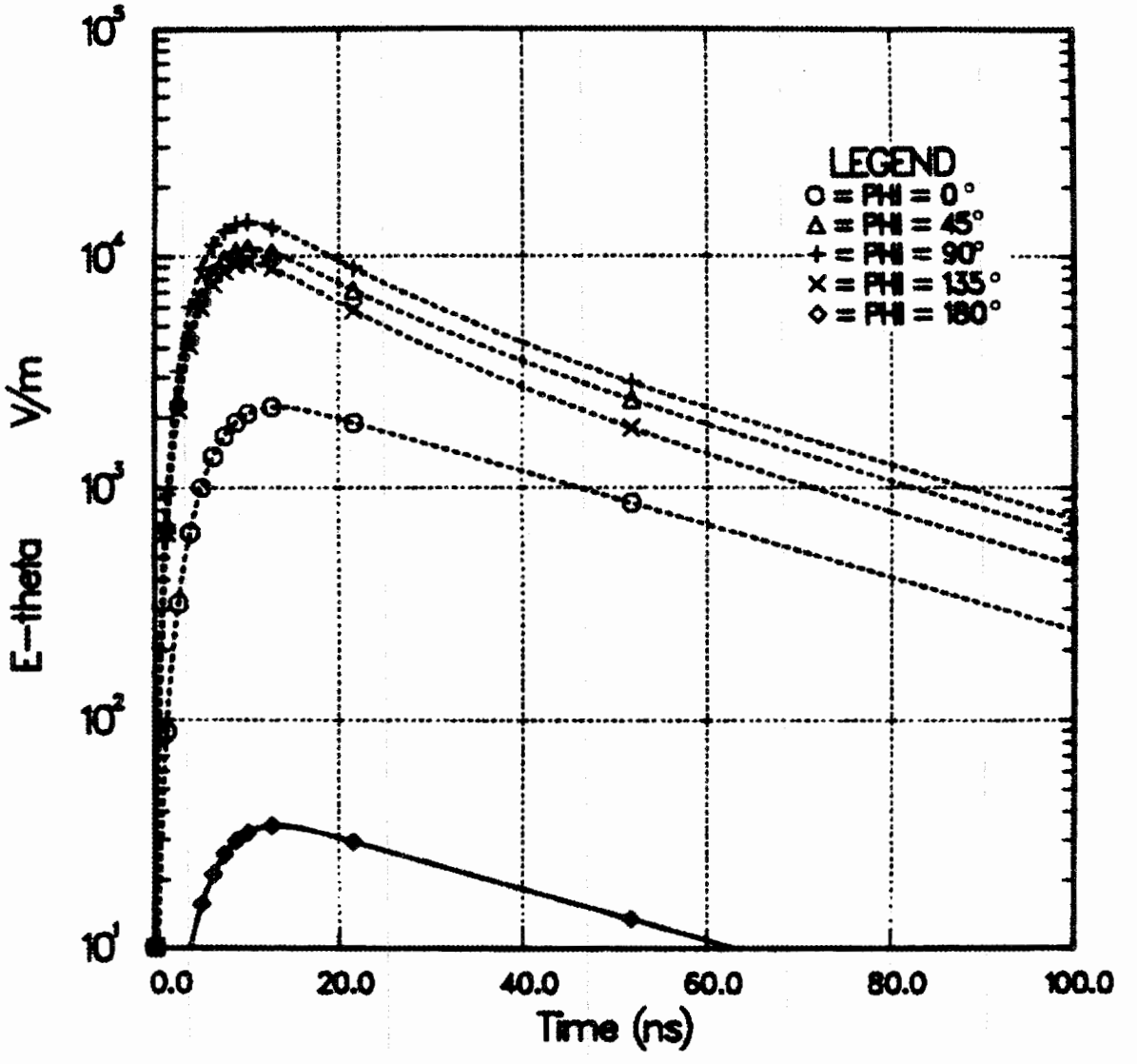

Figure 30. Fit to Figure 12. H = 400 km, GR = 776.6 km.

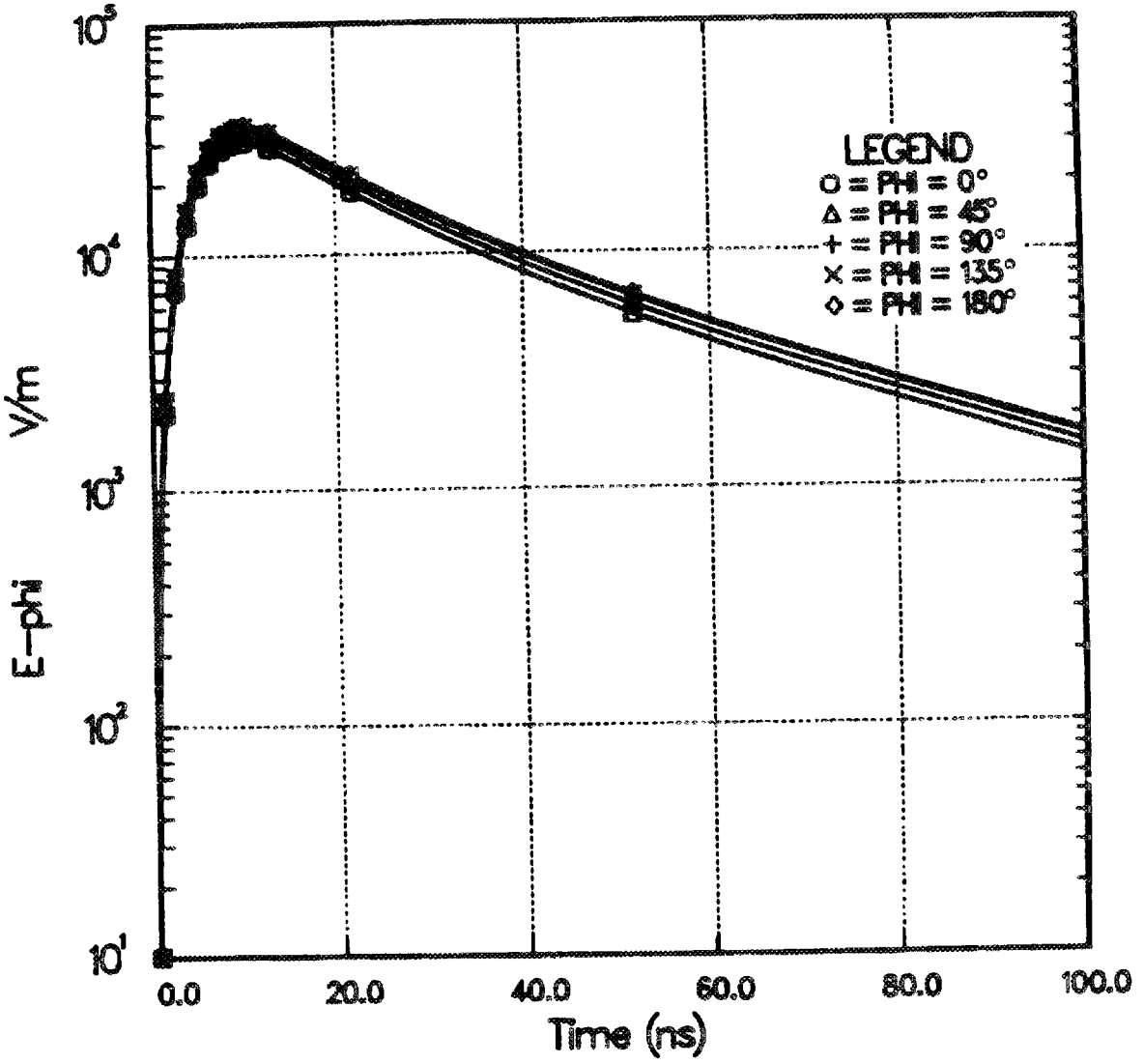

Figure 31. Fit to Figure 13. H = 400 km, GR = 776.6 km.

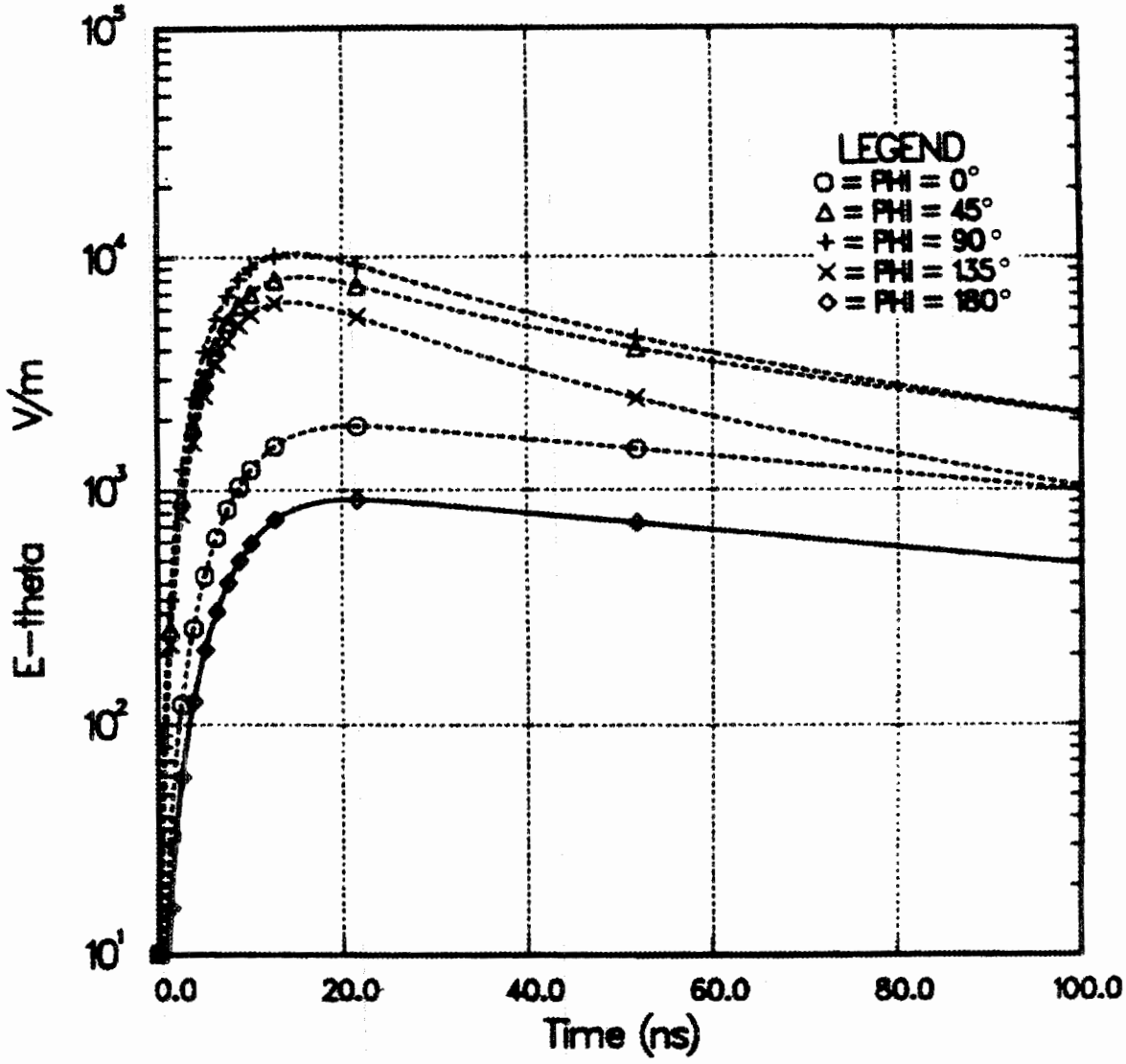

Figure 32. Fit to Figure 15. H = 400 km, GR = 1356.0 km.

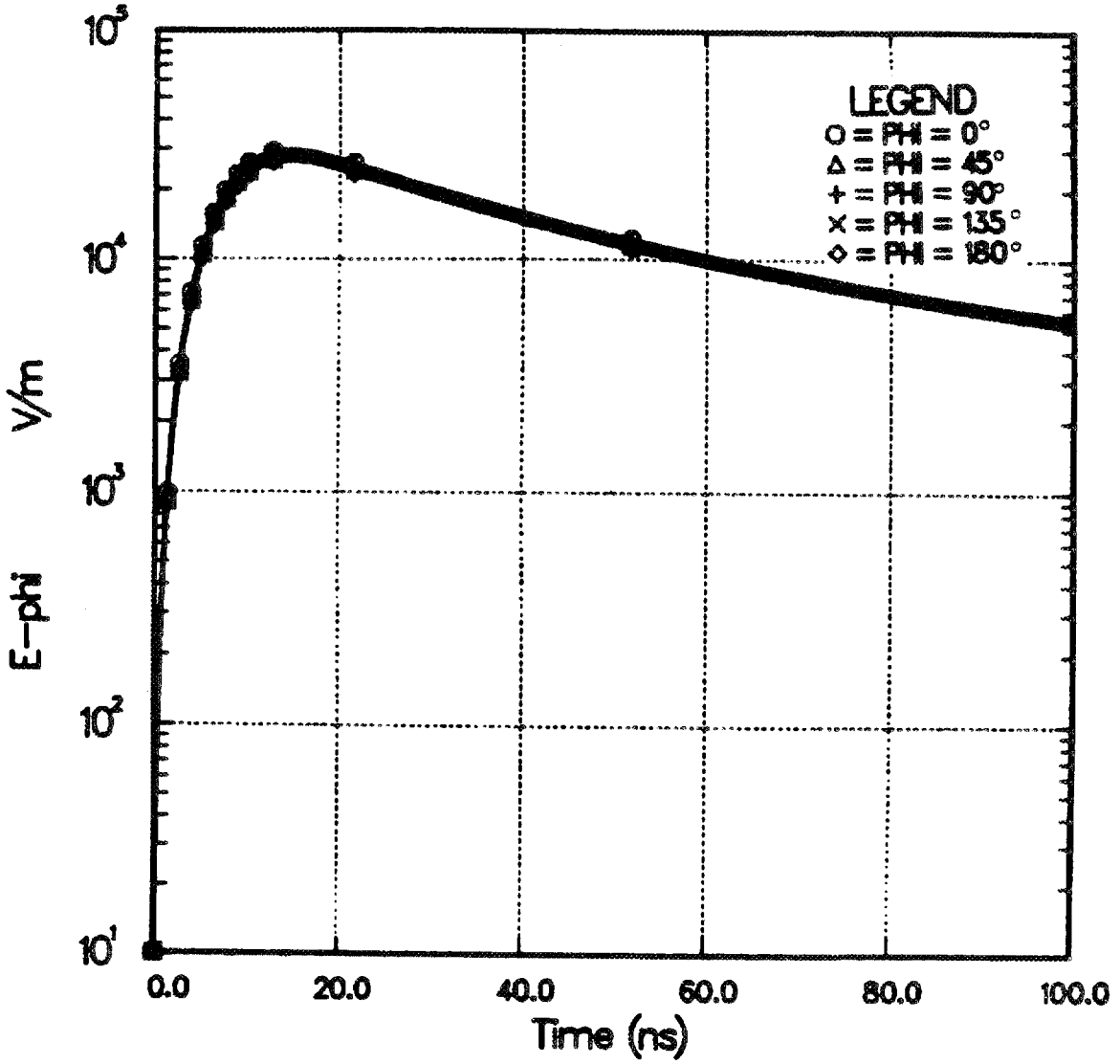

Figure 33. Fit to Figure 16. H = 400 km, GR = 1356.0 km.

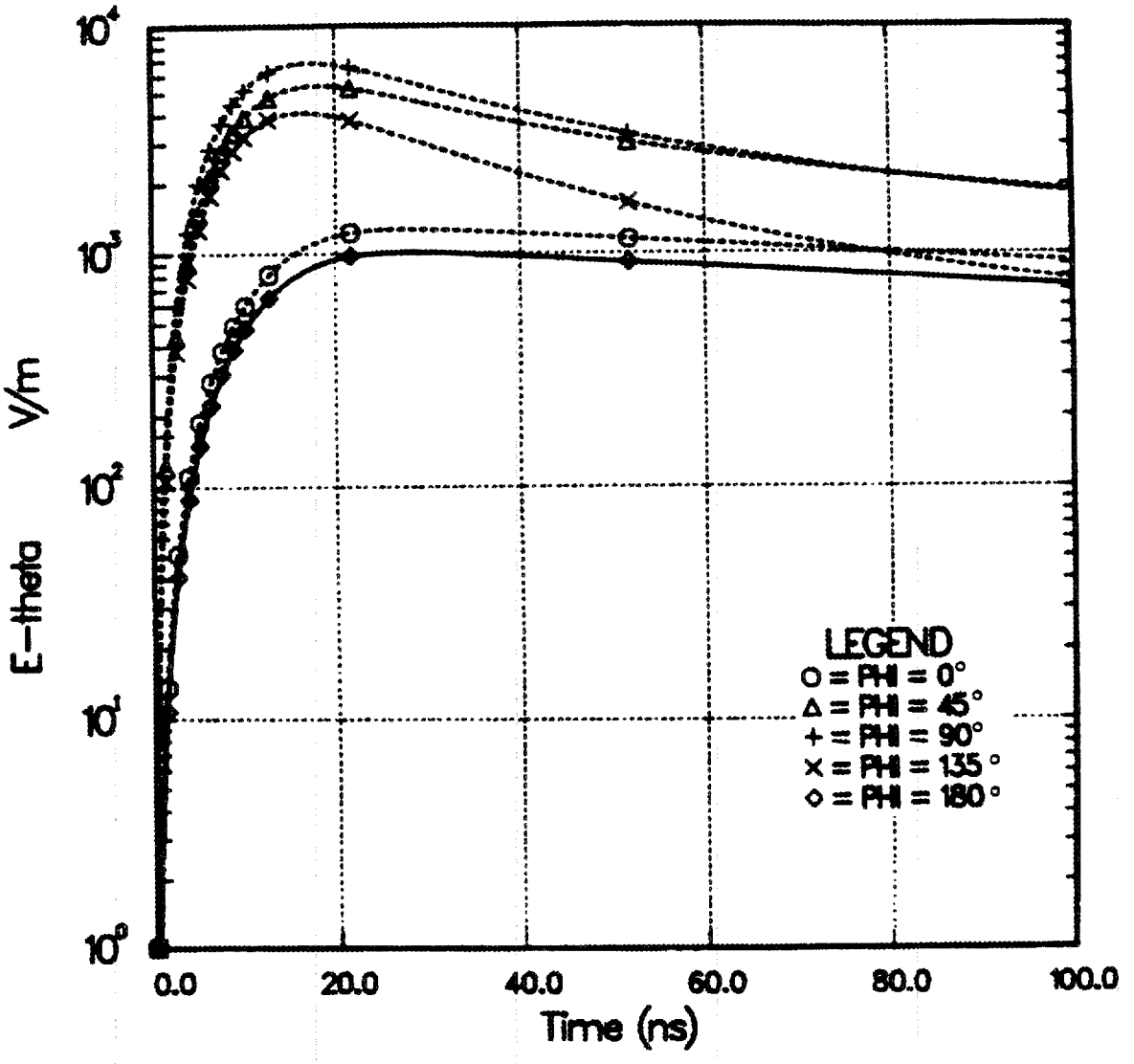

Figure 34. Fit to Figure 18. H = 400 km, GR = 2201.0 km.

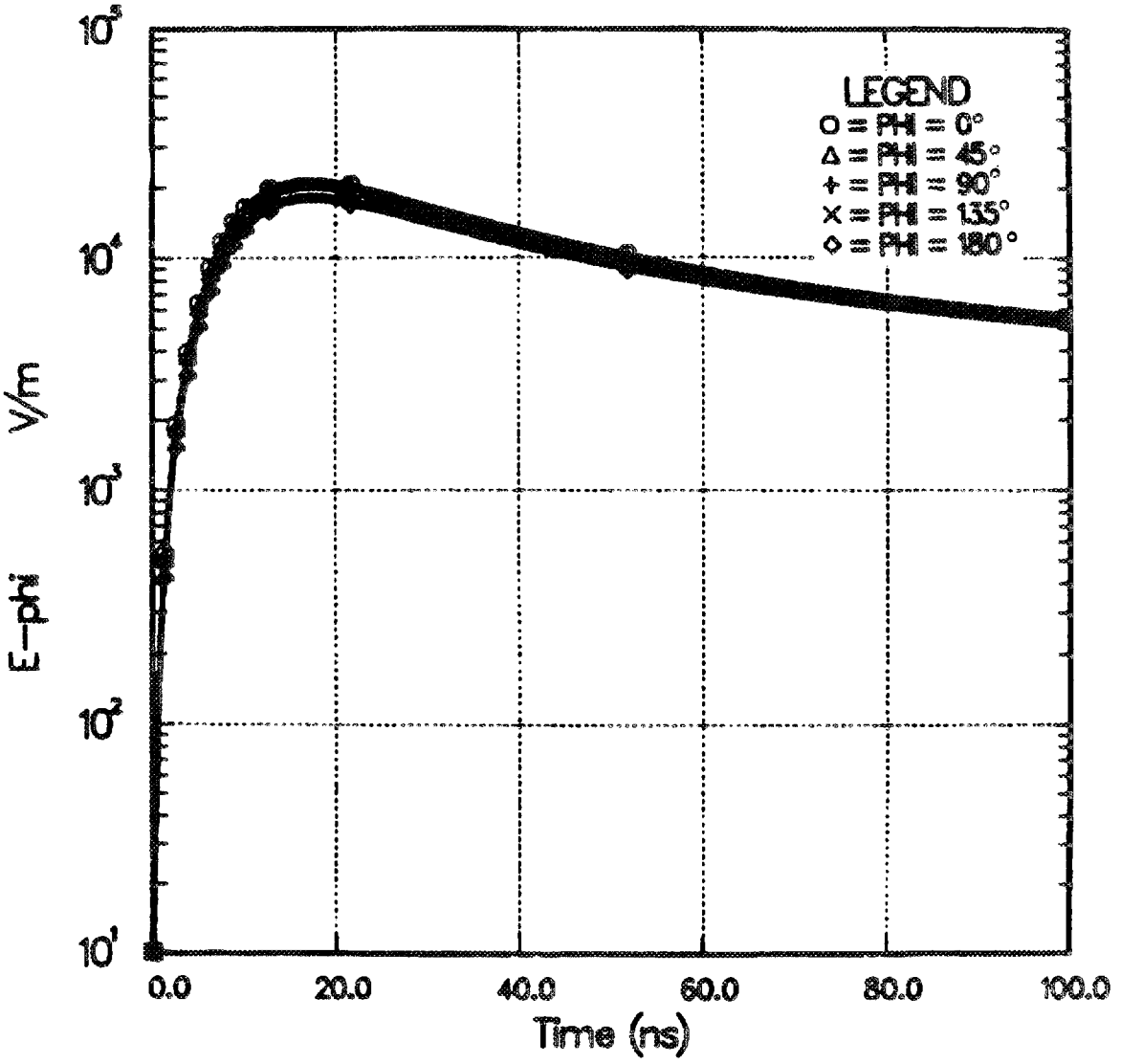

Figure 35. Fit to Figure 19. H = 400 km, GR = 2201.0 km.

SECTION 5
JUSTIFICATION OF CHAP RESULTS

In this section we examine the Compton current, air conductivity and electric field calculated by CHAP at four altitudes in the source region. This is done for H = 400 km and the observer at ground range of 777 km ($\theta_c = 60°$) and $\phi_c = 180°$. We show that these quantities are consistent with each other and with the physics of the outgoing wave theory.

5.1 THE COMPTON CURRENT

Table 2 lists relevant parameters for the four altitudes, which are given in the first column. The air density is ρ, and M is the mass of air per cm^2 traversed by the ray in reaching the given altitude. This was calculated using the burst elevation angle from the source region $\theta_s = 23.64°$, $\sin\theta_s = 0.401$. (Actually, this number varies slightly with altitude.) SR is the slant range from the burst. The mean free path λ_γ for Compton scattering of 2-MeV gammas is 22 gm/cm^2. From the total number of gammas N_γ emitted by the weapon ($N_\gamma = 1.3 \times 10^{26}$), the total density N_0 of birth places of Compton electrons, from first scatter of the gammas, is calculated from the formula (in consistent units)

$$N_0 = \frac{N_\gamma}{4\pi SR^2} \frac{\rho}{\lambda_\gamma} e^{-M/\lambda_\gamma} . \qquad (67)$$

This density is approached for $T > 1/\beta = 10^{-8}$ sec. (See equation (26).) At early times, the density of birth places is

$$N_b(T) \approx N_0 \beta T . \qquad (68)$$

Table 2. Parameters associated with four altitudes.

Alt., km	ρ, gm/cm^3	M, gm/cm^2	SR, km	N_0, m^{-3}	J_0, A/m^2
51.8	8.48E-7	1.65	764.4	6.35E7	3.05E-3
35.5	7.91E-6	13.7	805.1	3.09E8	1.48E-2
24.1	4.63E-5	74.6	824.7	1.08E8	5.18E-3
20.6	8.16E-5	129.4	842.2	1.51E7	7.25E-4

If the density N_0 of electrons were moving at the speed of light, it would make a current density

$$J_0 = N_0 ec = 4.8 \times 10^{-11} N_0 \text{ A/m}^2 , \tag{69}$$

which we call the reference current density. N_0 and J_0 are listed in Table 2.

Figure 36 shows J_ϕ as a function of retarded time at the four altitudes. The short horizontal bars near the maxima of the curves are the values of J_0. At the highest altitude, the maximum of J_ϕ is a little larger than J_0. This occurs because the density N_C of Compton electrons is higher than the density of birth places because of their radial motion,

$$N_C = N_0/(1 - \beta_r) . \tag{70}$$

Because β_r is near unity at early time, the average of $1/(1-\beta_r)$ can be greater than 10 at early time. This is explained in Reference 9. The maximum of the transverse current occurs before the electrons have been

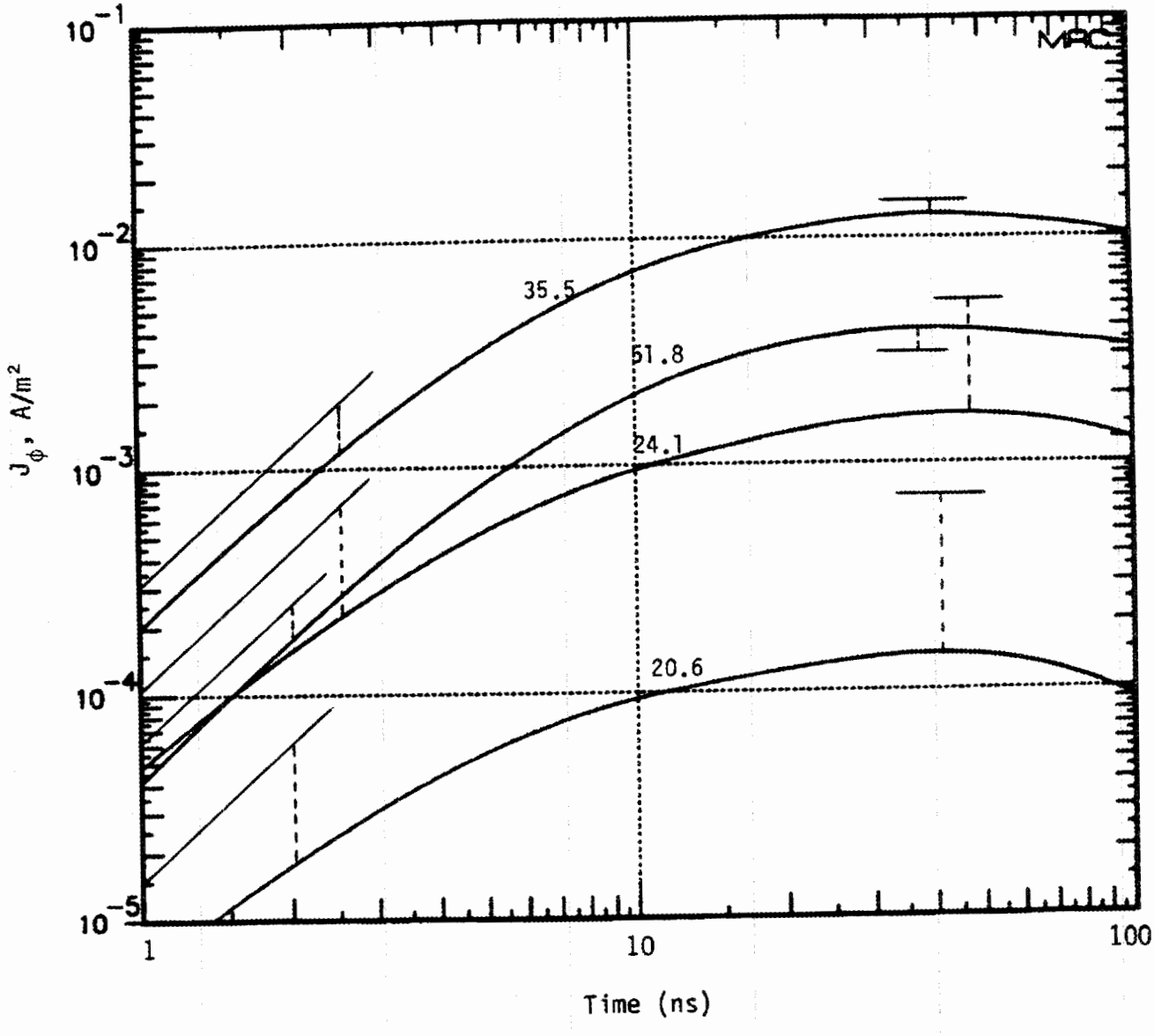

Figure 36. Compton current at four altitudes. H = 400 km. GR = 777 km. PHI = 180°.

turned through 90°, so that β_r is still positive at this time. At progressively lower altitudes, the maximum of J_ϕ becomes progressively smaller than J_0 because of multiple scattering and energy loss of the Compton electrons.

Reference 9 gives an analytical theory of the initial rise of the transverse Compton current. For an impulse source of gammas of energy 2 MeV, J_ϕ at early time is given by

$$J_\phi = 44.8 J_0 \omega_0 T \ , \tag{71}$$

where ω_0 is the gyro frequency

$$\omega_0 = eB/m = 0.92 \times 10^7 \ \text{sec}^{-1} \text{ in present case} \ . \tag{72}$$

Here m is the electron rest mass and e its charge. With our continuous gamma source after T = 0, where the density of birth places is given by equation (68), the expression for J_ϕ at early times is

$$J_\phi = 44.8 J_0 (\beta T)(\omega_0 T)/2 \ . \tag{72}$$

The sloping lines in figure 36 at early times are drawn from this formula. It can be seen that for the higher altitudes the J_ϕ computed by CHAP are only slightly less than this formula. At lower altitudes, the effect of multiple scattering is already substantial at retarded time of 10^{-9} sec. The actual age of Compton electrons is about 10 T at these early times. Thus the CHAP Compton currents are well justified.

5.2 THE AIR CONDUCTIVITY

Figure 37 shows the air conductivity computed by CHAP at the four altitudes. The conductivity is given by

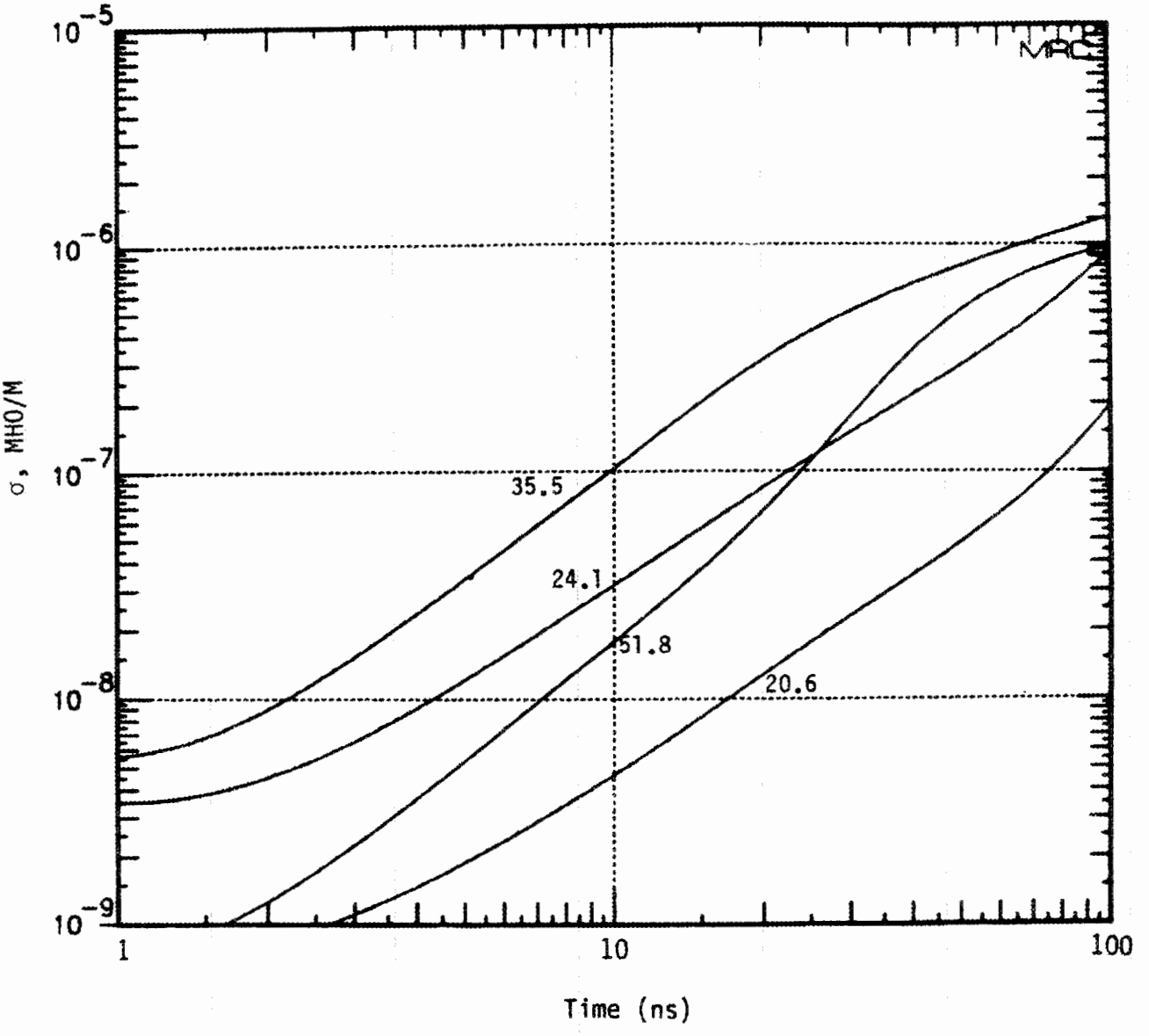

Figure 37. Air conductivity at four altitudes. H = 400 km. GR = 777 km. PHI = 180°.

$$\sigma = N_e e \mu \ , \tag{73}$$

where N_e is the density of secondary electrons and μ is their mobility. The mobility depends on the electric field (which Joule heats the secondary electrons) and on the air density. If μ were independent of E, the sigma curves woud be proportional to T^2 at early times. This follows from the fact that the density of Compton electrons is proportional to T, and each of these is ionizing at a constant rate, so that $N_e \propto T^2$. Because μ decreases with increasing E, σ rises less rapidly than T^2.

We shall examine the magnitude of the conductivity at 35.5 km altitude and at $T = 10^{-8}$ sec, which is

$$\sigma = 1.05 \times 10^{-7} \text{ mho/m} \ . \tag{74}$$

Figure 38 gives $E = 3.2 \times 10^4$ V/m at this altitude and time. From table 2 the air density is 6.4×10^{-3} atmospheres, so that

$$E/\rho = 5 \times 10^6 \text{ V/m/atmos} \ . \tag{75}$$

Note that this value of E/ρ is in the avalanche region, in which the ionization rate per electron is greater than its (two-body) attachment rate. However, experimental data of Davies (Ref. 10) shows that, at the low air density just stated, the ionization rate per electron is only 1.3×10^7/sec--not quite large enough to have a substantial effect on the electron density in times of the order of 10^{-8} sec. (There is a noticeable effect of avalanching in the conductivity curve for 51.8 km, beginning at 2×10^{-8} sec.)

For the value of E/ρ given by equation (75), Reference 10 gives the value of the mobility, for the present air density,

$$\mu = 6.4 \frac{m}{sec} / (\frac{V}{m}) \ . \tag{76}$$

In order to produce the conductivity of equation (74), equation (73) then requires an electron density of

$$N_e = 1.03 \times 10^{11}/m^3 \ . \tag{77}$$

Let us see if this is the correct number of secondaries made by the Compton electrons by a retarded time of 10^{-8} sec. At this time, the density of Compton birthplaces is

$$N_b = (1 - e^{-\beta T})N_0 = 0.63N_0 = 1.95 \times 10^8/m^3 \ , \tag{78}$$

and the average density over the time span is about half of this. The average density of Compton electrons is about 10 times that, or

$$\overline{N}_c = 9.8 \times 10^8/m^3 \ . \tag{79}$$

In sea level air, Compton electrons make about 66 ion pairs/cm, or 2.0×10^4 ion pairs per 10^{-8} sec. At the air density for altitude of 35.5 km, the ionization rate of a Compton electron would be about 128 ion pairs per 10^{-8} sec. However, this number includes all of the ionization produced by the Compton electrons and their more energetic secondaries. (See Ref. 6.) The primary ionization is only 40% of this. Reference 6 indicates that,

at 10^{-8} sec for the relevant air density, the ionization will be 78% complete. Thus the ionization per Compton electron by 10^{-8} sec will be

$$N_{ip} \approx 100 \text{ ion pairs/c.e.} \tag{80}$$

Multiplying this number by $\bar{N}_c$ gives

$$N_e = 9.8 \times 10^{10}/m^3 , \tag{81}$$

within 5% of the number given by equation (77) required to make the conductivity computed by CHAP. Thus the CHAP conductivities are well justified, at least at this one point.

5.3 ELECTRIC FIELDS

The electric fields at the four altitudes are shown in figure 38. In order to help in understanding these results, we have graphed the ratio J_ϕ/σ, the saturated field, in figure 39.

The condition for saturation at altitudes where the ray has traversed less than one gamma mean-free-path (22 gm/cm^2) is given by equation (22). In the present case

$$h' = 6.6 \text{ km}/0.401 = 1.65 \times 10^4 \text{ m} . \tag{82}$$

Thus equation (22) becomes

$$\sigma \geq 3.2 \times 10^{-7} \text{ mho/m} . \tag{83}$$

According to table 2, the two highest altitudes are above the 1 mfp point. According to figure 37, E_ϕ should saturate at about 4 shakes and 2 shakes at the 51.8 km and 35.5 km altitudes, respectively. Comparison of figures 38 and 39 shows that this is indeed the case.

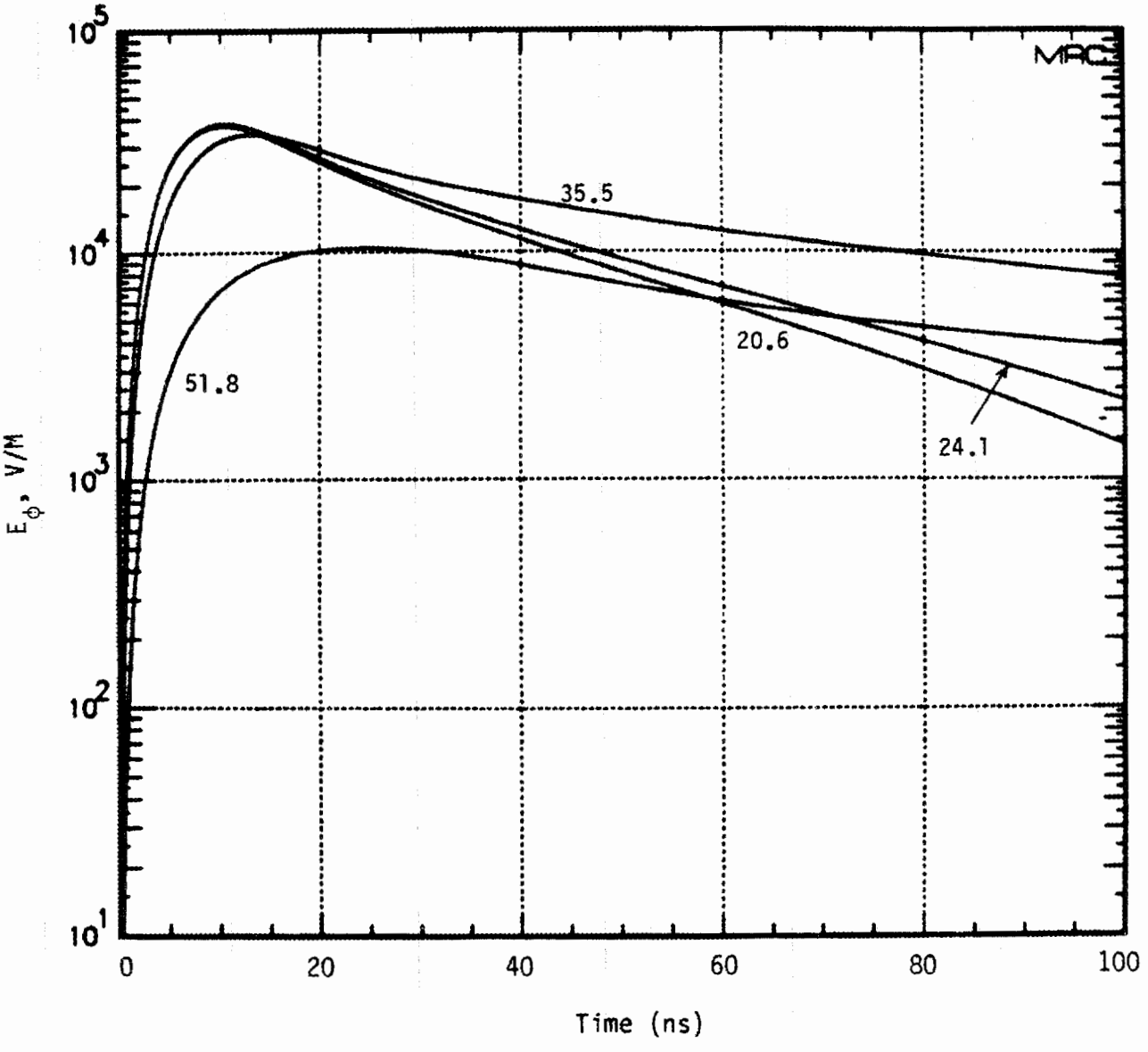

Figure 38. Electric field at four altitudes. H = 400 km. GR = 777 km. PHI = 180°.

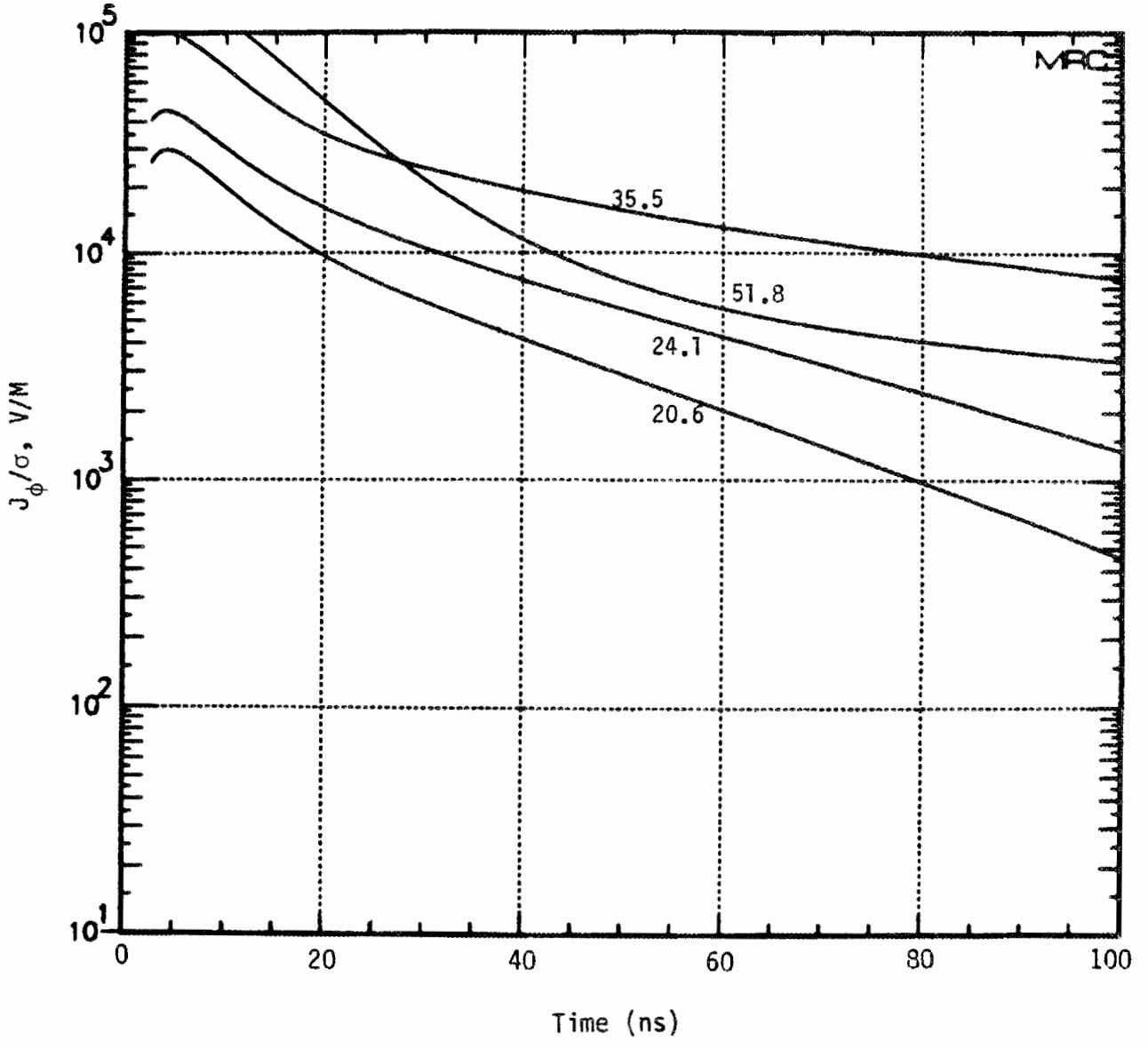

Figure 39. Saturated field at four altitudes. H = 400 km. GR = 777 km. PHI = 180°.

The condition for desaturation is that the attenuation length be long compared with λ_γ (in meters), the distance in which the conductivity will drop by a factor e^{-1}. At the two lower altitudes, according to table 2,

$$\begin{aligned} \lambda_\gamma &= 4.75 \times 10^3 \text{ m at } 24.1 \text{ km} , \\ &= 2.70 \times 10^3 \text{ m at } 20.6 \text{ km} . \end{aligned} \tag{84}$$

Thus the condition for desaturation before these altitudes are reached is

$$\begin{aligned} \sigma \ll 2/Z_0\lambda_\gamma &= 1.1 \times 10^{-6} \text{ mho/m at } 24.1 \text{ km} , \\ &= 2.9 \times 10^{-6} \text{ mho/m at } 20.6 \text{ km} . \end{aligned} \tag{85}$$

Figure 37 shows that this condition is well satisfied at all of the graphed times at 20.6 km. The conductivity is too small at this altitude to attenuate significantly the EMP that has been produced at higher altitude. This is fortunate for the EMP, since the saturated field is lower at this altitude. More intense gamma flux would reduce the EMP at the later times. This is the reason why the EMP is a short pulse at the smaller ground ranges in our nominal set of environments.

At 24.1 km, equation (85) is not well fulfilled at the later times graphed. That is why E_ϕ is decreasing at these times and at this altitude, as seen in figure 38.

Finally, let us check to see that there is enough Compton current at early times to produce the E_ϕ calculated by CHAP. Choosing a time of 10^{-8} sec, we normalize the Compton current to its value at 35.5 km. From this altitude upward, J_ϕ should be proportional to (see equation (67))

$$J_\phi \sim \frac{\rho}{\lambda_\gamma} e^{-M/\lambda_\gamma} , \tag{86}$$

since multiple scattering has not had a pronounced effect at 10^{-8} sec at these altitudes. The constant of proportionality can be fixed by writing

$$J_\phi = J_1 \frac{\rho}{\rho_1} e^{-(M-M_1)/\lambda_\gamma} , \tag{87}$$

where the subscripts 1 refer to quantities at 35.5 km. Then using equation (15) (which neglects conduction current), we find

$$E_\phi = \frac{Z_0}{2} J_1 \int \frac{\rho}{\rho_1} e^{-(M-M_1)/\lambda_\gamma} dr$$

$$= \frac{Z_0}{2} J_1 \frac{\lambda_\gamma}{\rho_1} \int \frac{dM}{\lambda_\gamma} e^{-(M-M_1)/\lambda_\gamma}$$

$$= \frac{Z_0}{2} J_1 \frac{\lambda_\gamma}{\rho_1} \text{ at } 35.5 \text{ km} . \tag{88}$$

Using $\lambda_\gamma = 22$ gm/cm^2, and $\rho_1 = 7.91 \times 10^{-6}$ gm/cm^2 from table 2 gives

$$\frac{\lambda_\gamma}{\rho_1} = 2.78 \times 10^6 \text{ cm} = 2.78 \times 10^4 \text{ m} . \tag{89}$$

Then using $J_1 = 7 \times 10^{-3}$ A/m^2 from figure 36 gives

$$E_\phi = 3.7 \times 10^4 \text{ V/m at } 35.5 \text{ km} . \qquad (90)$$

This is a little larger than the value 3.2×10^4 V/m read from figure 38 at 1 shake. Air conductivity has just begun to have a significant effect.

Thus the relation of the CHAP E_ϕ to J_ϕ and σ is at least approximately in agreement with the outgoing wave theory. Actually, CHAP is probably a little more accurate than the outgoing wave theory, since it includes ingoing waves.

SECTION 6
FOURIER TRANSFORMS AND CONTOUR PLOTS

Fourier transforms of the HEMP fields are of direct practical use only for systems that are known to respond linearly to the HEMP. Even then, their principal utility is for narrow band systems, e.g., some antennas. Figure 40 shows the amplitude of the Fourier transforms of several of the E_ϕ fields calculated by CHAP. It is seen that there is substantial variation in the transforms, as there is in the time-domain fields.

To offer a more graphic view of the dependence of the HEMP on range and azimuth, figures 41, 42 and 43 present contour plots of the peak values of E_ϕ, E_V and E_ρ. Generally, these peak values tend to decrease with increasing range, in addition to varying with azimuth. However, the pulse length increases with increasing range. Figure 44 presents a contour plot of $\int E_\phi dt$, the impulse associated with the principal component E_ϕ of the HEMP. This quantity, which is significant for the coupling to long lines, is seen to increase with increasing range out to the horizon.

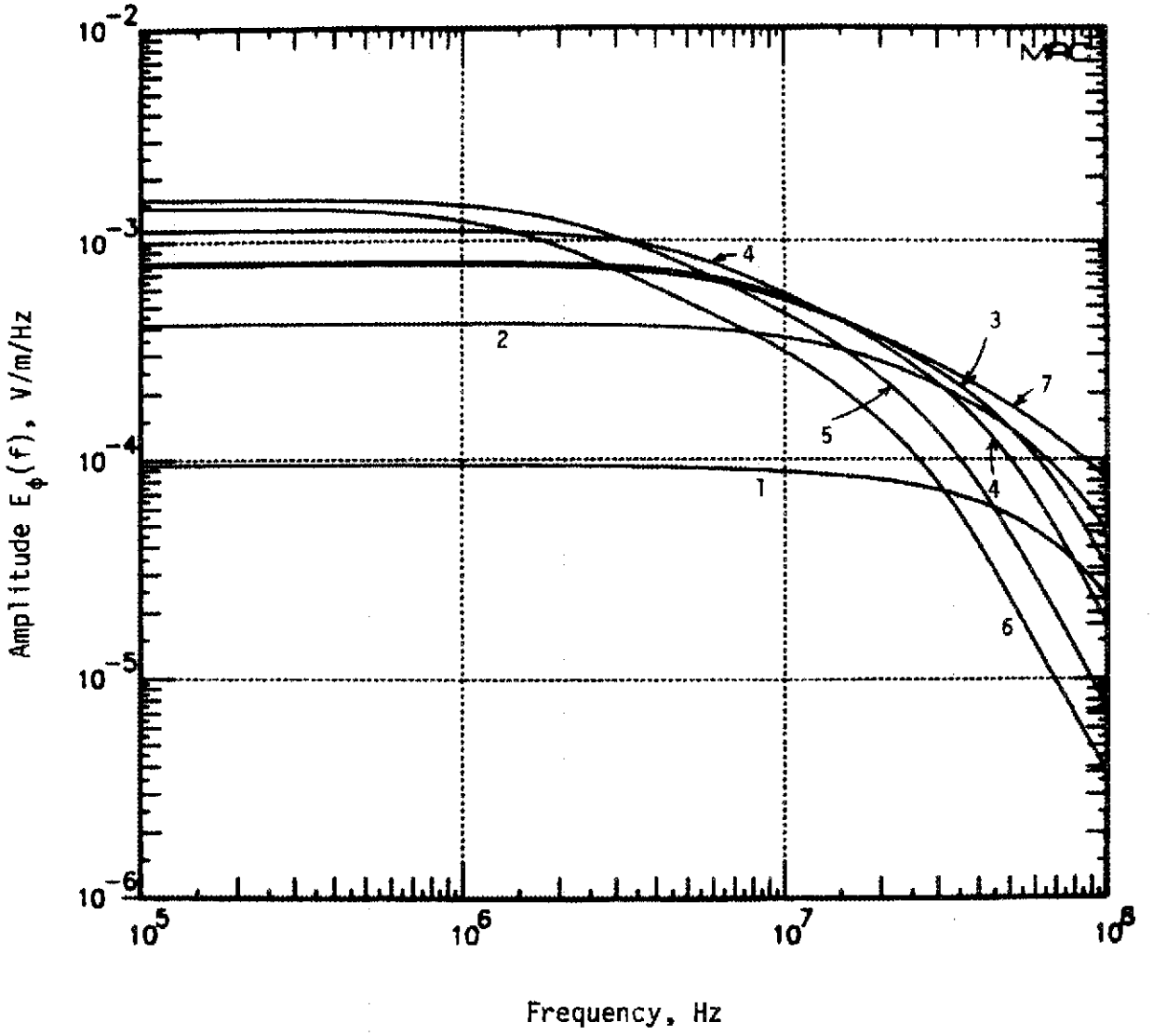

Observers:

1 H = 400 km, GR = 0, ϕ_c = 0

2 H = 400 km, GR = 233 km, ϕ_c = 180°

3 H = 400 km, GR = 501 km, ϕ_c = 180°

4 H = 400 km, GR = 777 km, ϕ_c = 180°

5 H = 400 km, GR = 1356 km, ϕ_c = 180°

6 H = 400 km, GR = 2201 km, ϕ_c = 180°

7 H = 200 km, GR = 365 km, ϕ_c = 180°

Figure 40. Amplitude of Fourier transforms of E_ϕ for various observers.

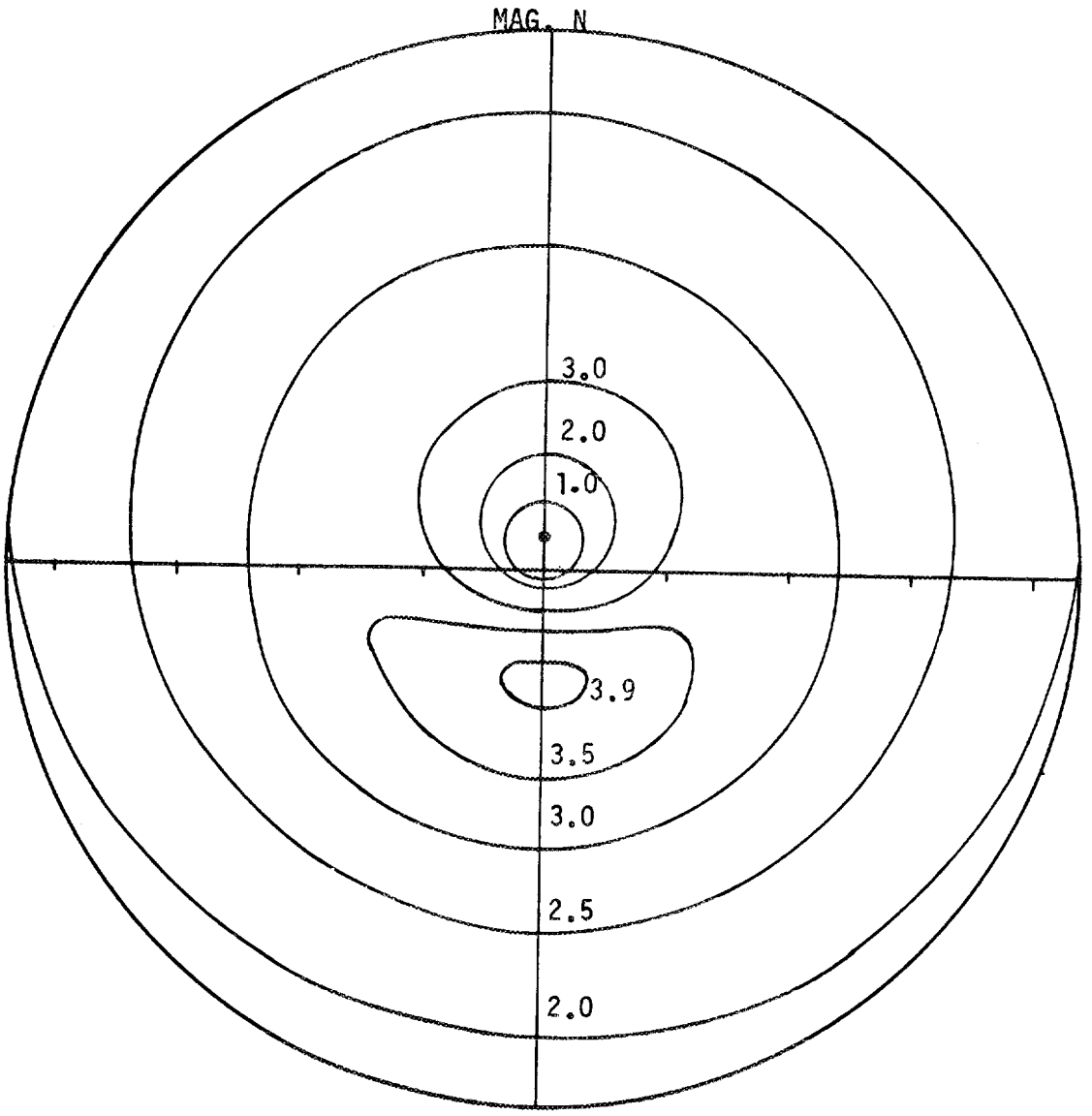

Figure 41. Contour plot of the peak value of the azimuthal electric field E_ϕ. Numbers on the contours are in units of 10^{-4} V/m. The outer circle is the horizon at 2200 km ground range.

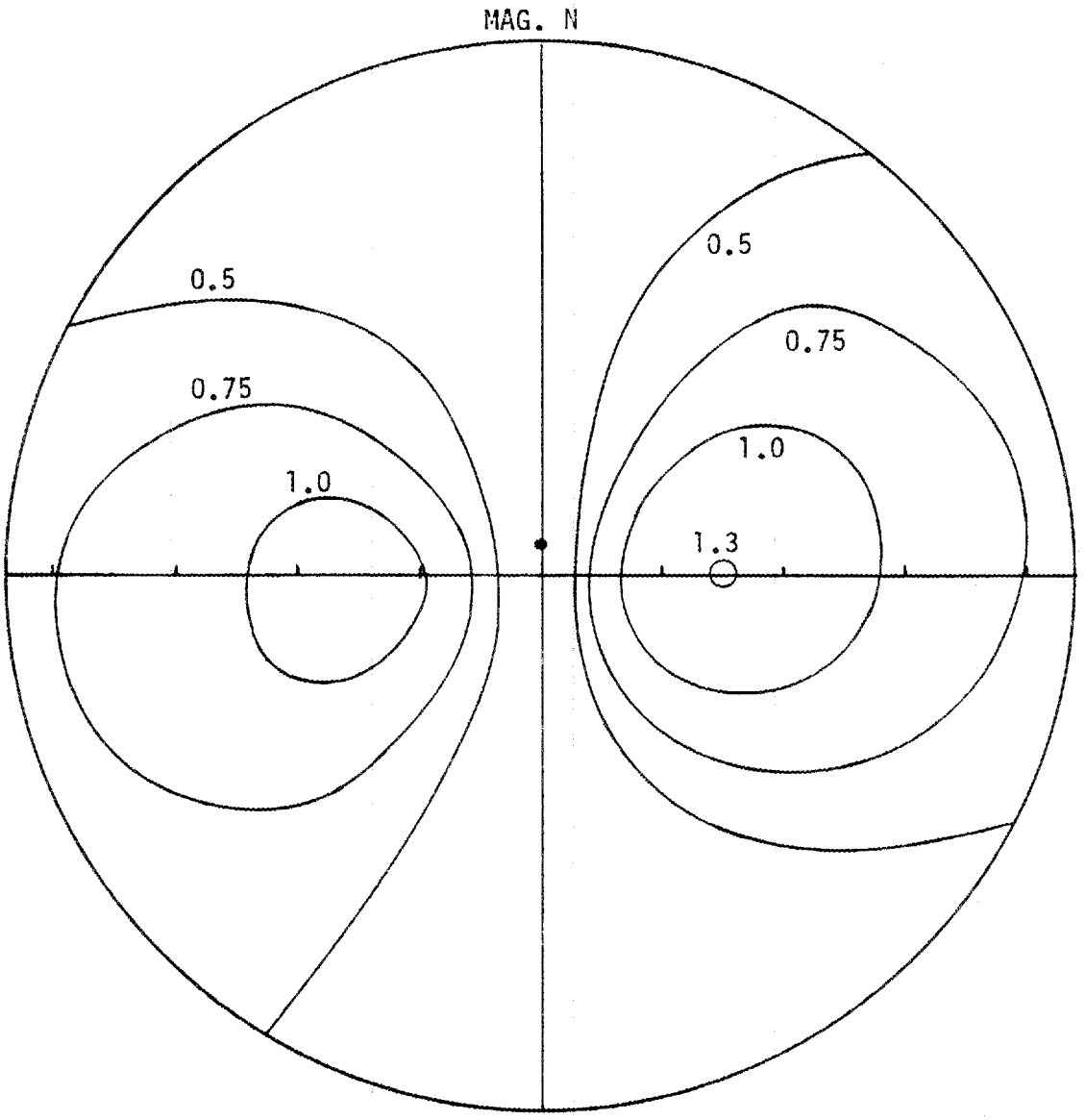

Figure 42. Contour plot of the peak value of the vertical electric field E_v. Numbers on the contours are in units of 10^4 V/m. The outer circle is the horizon at 2200 km ground range.

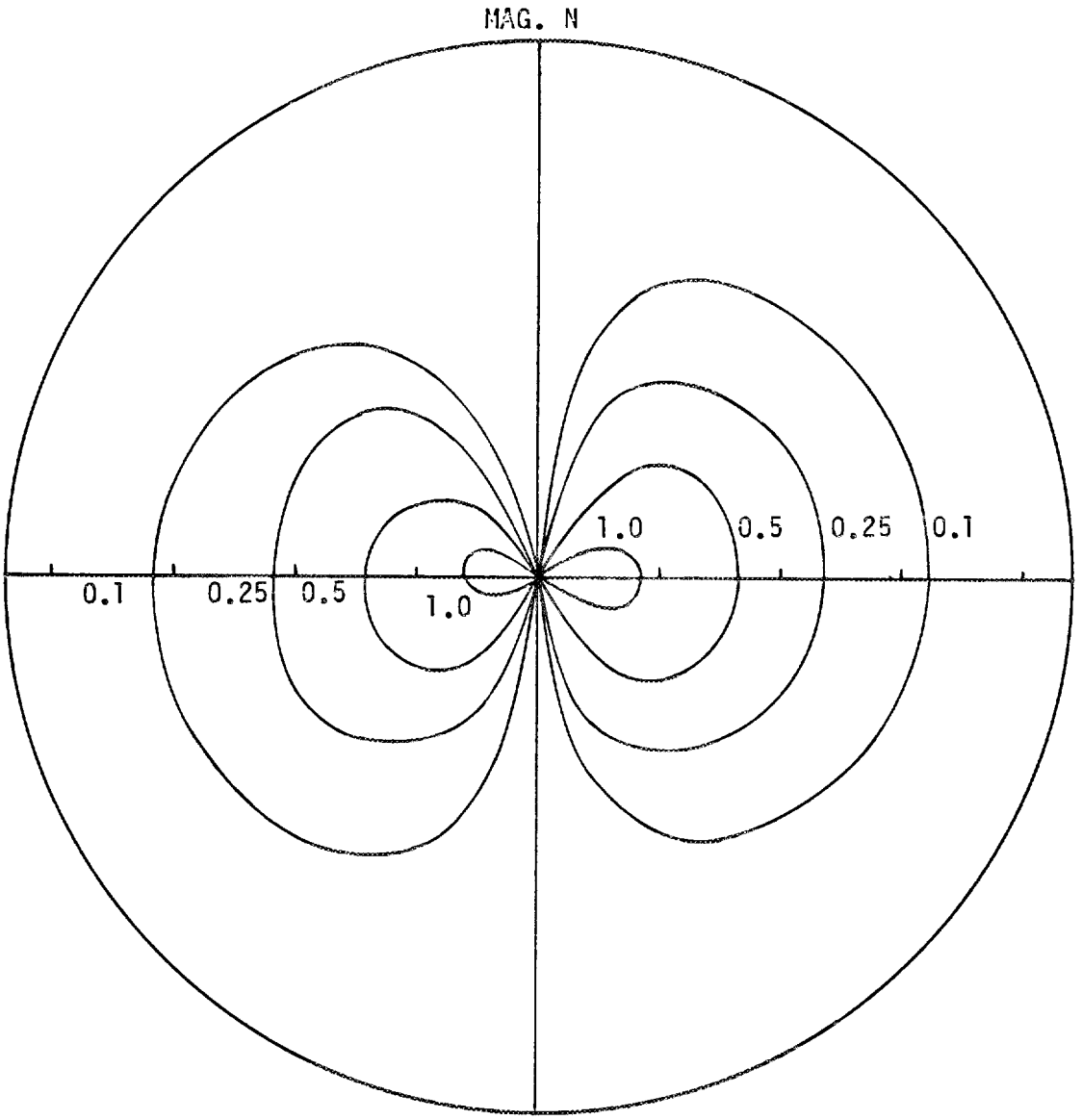

Figure 43. Contour plot of the peak value of the horizontal radial electric field E_ρ. Numbers on the contours are in units of 10^4 V/m. The outer circle is the horizon at 2200 km ground range.

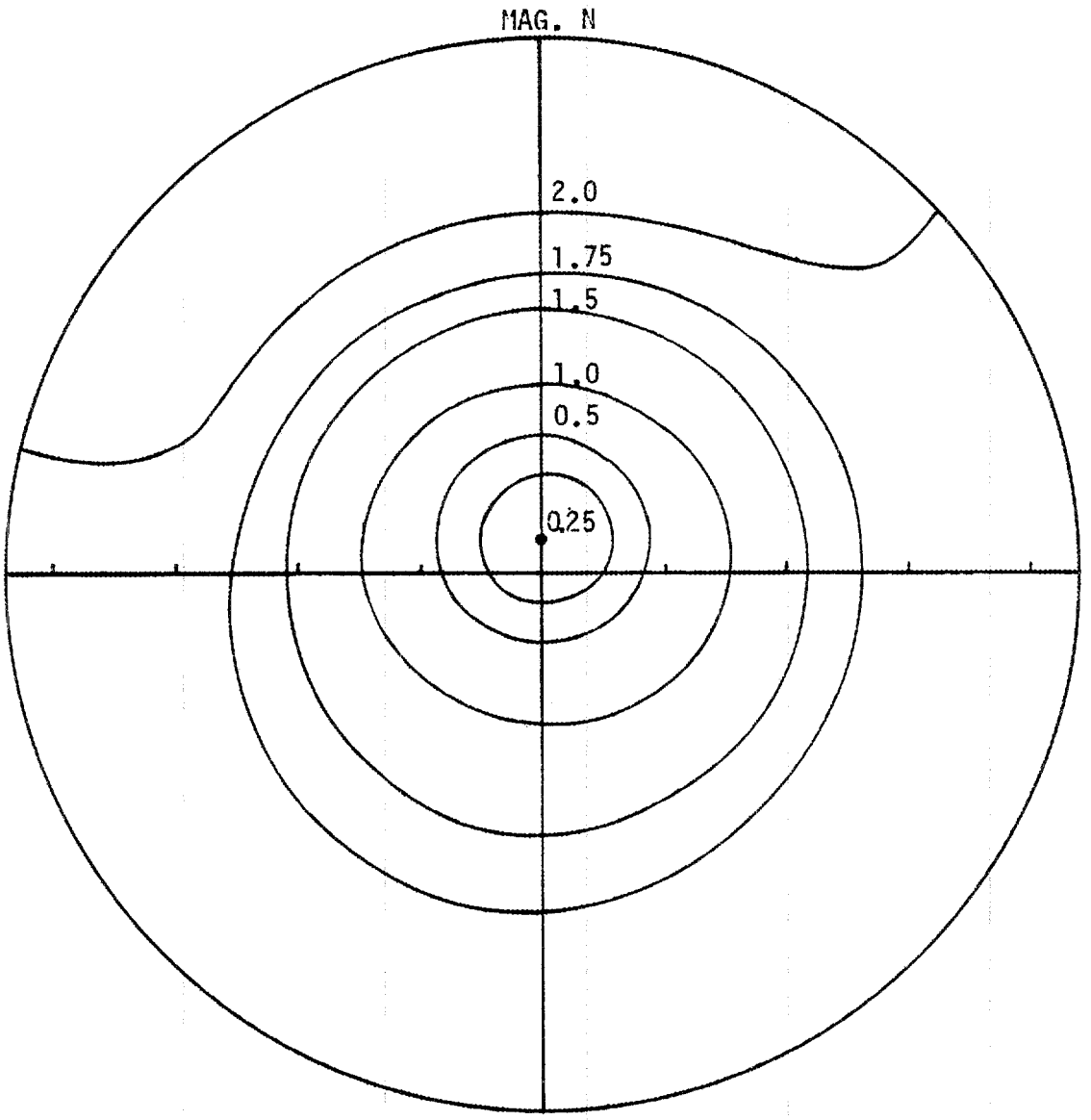

Figure 44. Contour plot of the impulse $\int E_\phi dt$. Numbers on the contours are in units of 10^{-3} V sec/m. The outer circle is the horizon at 2200 km ground range.

LIST OF REFERENCES

1. Longmire, C. L., IEEE Trans. on Ant. and Prop., Vol. AP-6, No. 1, p. 3, January 1978.

2. Longmire, C. L., "Close-In EM Effects Lectures X and XI," Los Alamos Scientific Laboratory, LAMS-3073, April 1964, unpublished.

3. Karzas, W. J., and R. Latter, "Phys. Rev., Vol. 137B, p. 1369, 1965.

4. Longley, H. J., and C. L. Longmire, "Development of CHAP--A High-Altitude EMP Code," MRC-R-375, DNA 4521T, Mission Research Corporation, January 1978.

5. Hamilton, R. M., S. R. Schwartz and C. L. Longmire, report to be published by Lawrence Livermore National Laboratory.

6. Longmire, C. L., and J. Koppel, "Formative Time Lag of Secondary Ionization," MRC-R-88, Mission Research Corporation, January 1974.

7. Longmire, C. L., "The Early-Time EMP from High-Altitude Nuclear Explosions," MRC-R-809, DNA-TR-84-175, Mission Research Corporation, December 1983.

8. Glasstone, S., and P. J. Dolan, "The Effects of Nuclear Weapons," pp. 495 and 534, 1977.

9. Longmire, C. L., "Effect of Multiple Scattering on the Compton Recoil Current," MRC-R-378, DNA-4543T, Mission Research Corporation, February 1978.

10. Davies, D K., "Measurements of Swarm Parameters in Dry Air," Westinghouse Electric Corporation, published by Dikewood Corporation as report DC-TN-2030.308-1, May 1983.

ORNL/Sub/86-18417/1
Dist. Category 97a,b,c

INTERNAL DISTRIBUTION

1-24. P. R. Barnes
25. R. B. Braid
26. R. S. Carlsmith
27. F. C. Chen
28. L. G. Christophorou
29. R. I. Crutcher
30. S. J. Dale
31. W. Fulkerson
32. P. A. Gnadt
33. T. L. Hudson
34. M. A. Kuliasha
35. F. C. Maienschein
36. J. W. MacDonald
37. B. W. McConnell
38. M. O. Pace
39-43. D. J. Slaughter
44. R. A. Stevens
45-46. J. P. Stovall
47. Central Research Library
48. Document Reference Section
49. Energy Information Library
50-52. Laboratory Records - RC
53. Laboratory Records Department
54. ORNL Patent Section

EXTERNAL DISTRIBUTION

55. V. D. Albertson, Department of Electrical Engineering, 123 Church Street, S. W., University of Minnesota, Minneapolis, MN 55455

56. H. W. Askins, Jr., The Citadel, Charleston, SC 29409

57. AT&T Information Systems, Division Manager, Building 83, Room 1B23, 100 Southgate Parkway, Morristown, NJ 07960

58. C. E. Baum, AFWL/NTAAB, Kirkland AFB, NM 87117-6008

59. R. Bellem, Director for Radiation, Defense Nuclear Agency, Washington, DC 20305

60. D. W. Boehm, DCA, Code R-430, DCEC, 1860 Wiehill Avenue, Reston, VA 22090-5500

61. J. N. Bombardt, R & D Associates, 105 E. Vermijo Street, Suite 450, Colorado Springs, CO 80903

62. G. E. Brackett, Code H25, Navy Surface Weapons Center, 1091 New Hampshire Avenue, Silver Springs, MD 20903-5000

63. E. H. Brehm, Department GK/CN32, Brown, Boveri, and Cie, Aktiengesellschaft, Postfach 351, D-6800 Mannheim 1, WEST GERMANY

64. F. C. Buchholz, Pacific Gas & Electric Co., 77 Beagle Street, Room 2933, San Francisco, CA 94106

65. J. F. Buck, Wisconsin Electric Power Company, 231 W. Michigan, Milwaukee, WI 53201

66. L. M. Burrage, McGraw-Edison, P. O. Box 100, 11131 Adams Road, Franksville, WI 53126

67. H. S. Cabayan, Lawrence Livermore Laboratory, P. O. Box 5504, Livermore, CA 94550

68. F. L. Cain, Georgia Institute of Technology, Engineering Experiment Station, Atlanta, GA 30332

69. J. G. Carbonell, Carnegie-Mellon University, Pittsburgh, PA 15213

70. R. N. Carlile, Department of Electrical and Computer Engineering, University of Arizona, Tucson, Arizona 85721

71. I. J. Carney, Nuclear Survivability Organization, Boeing Aerospace Company, P. O. Box 3999, Seattle, WA 98124

72. CESE, Via Rubattino 54, Milano, 20734 ITALY

73. V. L. Chartier, Bonneville Power Administration, P. O. Box 491-ER, Vancouver, WA 98666

74. K. K. Chen, Sandia National Laboratory, Drawer 1333, P. O. Box 5800, Kirkland AFB, NM 87185

75. R. F. Chu, Philadelphia Electric Company, 2301 Market Street, MS 10-1 P. O. Box 8699, Philadelphia, PA 19101

76. H. E. Church, Aluminum Company of America, 1501 Alcoa Building, Pittsburgh, PA 15219

77. B. Cikotas, Defense Communications Agency, Code 8340, Arlington Hall Station, Arlington, VA 22213-542

78. C. F. Clark, Bonneville Power Administration, P. O. Box 3621, Portland, OR 97208

79. R. E. Clayton, Power Technologies, P. O. Box 1058, 1482 Erie Boulevard, Schenectady, NY 12301-1058

80. A. Clerici, Sanelmi, Via Pergolesi 25, 20124 Milano, Italy

81. H. W. Colborn, North American Electric Reliability Council, 101 College Road East, Princeton, NJ 08540-6601

82. P. L. Collins, Defence Intelligence Agency, VP-TPO, Washington, DC 20301-6111

83. D. E. Cooper, Southern California Edison Company, P. O. Box 800, 2244 Walnut Grove Avenue, Rosemead, CA 91770

84. R. Cortina, ENEL-Centro Ricera, Automatica, VIA Volta 1, Cologno Monzese (MI), ITALY

85. G. Dahlen, Royal Institute of Technology, S-100-44, Stockholm, SWEDEN

86. J. Darrah, Headquarters, NORAD/G5, Peterson AFB, CO 80914

87. W. M. Druen, 8200 South Memorial Parkway, Suite D, Huntsville, Alabama 35802

88. J. C. Engimann, Commonwealth Edison, 1319 S. First Avenue, Maywood, IL 60153

89. D. M. Ericson, Jr., Sandia National Laboratory, Division 6414, Kirkland AFB, NM 87185

90. W. E. Ferro, Electric Research and Management, Inc., P. O. Box 165, State College, PA 16804

91. W. G. Finney, Project Manager, Stanley Consultants Incorporated, Stanley Building, Muscatine, IA 52761

92. F. Fisher, GE Corporation, Electric Utility Systems Engineering, Building 5, Room 306, Schenectady, NY 12345

93. M. Fitzgerald, MITRE Corporation, P. O. Box 208, Bedford, MA 01730

94. P. B. Fleming, Science & Eng. Associates, Mariners Square, Suite 127 1900 N. Northlake Way, P. O. Box 31819, Seattle, WA 98103

95. R. Gates, Research Division, Federal Emergency Management Agency, 500 C Street, SW, Washington, DC 20472

96. M. R. Gent, North American Electric Reliability Council, 101 College Road East, Princeton, NJ 08540-6601

97. S. M. Gillis, Duke University, Department of Economics, 4875 Duke Station, Durham, NC 27706

98. W. Graham, R & D Associates, P. O. Box 9695, Marina Del Ray, California 90291

99. J. J. Grainger, Electric Eng. Department, North Carolina State University, 5004 Hermitage Drive, Raleigh, NC 27612

100. I. S. Grant, Power Technologies Incorporated, 1482 Erie Boulevard, Schenectady, NY 12305

101. A. R. Gritzke, U. S. Department of Navy, Nuclear Warfare Projects Office, Washington, DC 20360

102. J. Gut, Institute for Military Security Technology, Auf der Mauer 2, Zurich CH-8001, SWITZERLAND

103. V. Guten, National Security Agency (R-52), Fort G. Mead, MD 20755

104. M. H. Heese, Rensselaer Polytechnic Institute, JEC 5008, Troy, NY 12181

105. D. Higgins, JAYCOR, Santa Barbara Facility, 360 South Hope Avenue, P. O. Box 30281, Santa Barbara, CA 93105

106. D. W. Hilson, Power Electronics Application Center, 10521 Research Drive, Suite 400, Knoxville, TN 37932

107. Dr. Narain Hingorani, Electric Power Research Institute, P. O. Box 10412, Palo Alto, CA 94303

108. F. C. Holdes, Pacific Gas & Electric Company, 3235-18th Street, San Francisco, CA 94110

109. W. S. Howington, Noranda Aluminum, Inc., P. O. Box 70, New Madrid, MO 63869

110. Hutchins, BDM Corporation, 1801 Randolph, SW, Albuquerque, NM 87106

111. Hugh M. Hyatt, Applied Pulse Corp. (APC), 153 Commercial Avenue Sunnyvale, CA 94086

112. V. Inkis, Ontario Hydro, U7E1, 700 University Avenue, Toronto, Ontario M5G1X6, CANADA

113. Paul B. Jacob, Mississippi State University, P. O. Drawer EE, Mississippi State, MS 39762

114. Wasyl Janischewskyj, University of Toronto, Electrical Eng. Department, Toronto, Ontario, M5S1A4, CANADA

115. H. P. Johnson, Georgia Power Company, 270 Peachtree Street, 11th Floor, Atlanta, GA 30303

116. V. K. Jones, Science & Engineering Associates, Inc., Mariners Square, Suite 127, 1900 N. Northlake Way, P. O. Box 31819, Seattle, WA 98103

117. F. R. Kalhammer, Electric Power Research Institute, 3412 Hillview Avenue, P. O. Box 10412, Palo Alto, CA 94303

118. T. Karlsson, FOA 387, Box 1165, Likoping, 58111 SWEDEN

119. W. Karzas, R & D Associates, P. O. Box 9695, Marina Del Rey, CA 90291

120. R. E. Kasperson, Clark University, Graduate School of Geography, Worchester, MA 01610

121. Ken Klein, U.S. Dept. of Energy, 1000 Independence Avenue, SW, Forrestal Building, Room 5E-052, Washington, DC 20585

122. J. Kopefinger, Duquesne Light Company, System Planning Department 21-2, 1 Oxford Center, Pittsburgh, PA 15279

123. N. Kolcio, American Electric Power, 1 Riverside Plaza, Columbus, OH 43216

124. D. C. Koury, SHADE, CIS PCB SES, Apo, NY 09055

125. T. R. LaPorte, Institute of Government Studies, 109 Moses Hall, Berkeley, CA 94720

126. J. Labadie, IRT, 6800 Poplar Place, McLean, VA 22131

127. H. T. Lam, South Carolina Public Service Authority, 1 Riverwood Drive, Monks Corner, SC 29461

128. R. C. Latham, Duke Power Company, P. O. Box 33189, Charlotte, NC 28242

129. A. Latter, R & D Associates, P. O. Box 9695, Marina Del Rey, CA 90291

130. J. S. Lawler, University of Tennessee, Department of Electrical Engineering, Knoxville, TN 37916

131. K. S. H. Lee, Kaman Science Corporation, Dikewood Division, 2800 28th Street, Suite 3780, Santa Moncia, CA 90405

132. J. R. Legro, Advanced Systems Technology, Westinghouse Electric Corporation, 777 Penn Center Blvd., Pittsburgh, PA 15235

133. M. Lessen, Consulting Engineer, 12 Country Club Drive, Rochester, NY 14618

134. Library, Defense Technical Information Center, Cameron Station, Alexandria, VA 22314

135. Library, JAYCOR, 205 S. Whiting Street, Alexandria, VA 22304

136. Library, Institute for Energy Analysis, ORAU, Oak Ridge, TN 37830

137. J. Lloyd, U. S. Army Engineering, USAEDH (ED-SD), P. O. Box 1600 Huntsville, AL 35087

138. J. Locasso, Rockwell International, 3370 Meraloma Avenue, P. O. Box 4192 Mail Code 031-BB17, Anaheim, CA 92803

139. Dr. C. L. Longmire, Mission Research Corporation, P. O. Drawer 719, Santa Barbara, CA 93102

140. R. M. Maliszewski, American Electric Power Service Corporation, 1 Riverside Plaza, P. O. Box 16631, Columbus, OH 43216-6631

141. J. N. Mallory, Southern California Edison Co., P. O. Box 800, Rosemead, CA 91770

142. G. C. Manthey, Energy R & D, DOE/ORO, Federal Building, Oak Ridge, TN 37830

143. T. A. Martin, IRT Corporation, 1953 Gallows Road, Vienna, VA 22180

144. J. D. Martin, Harris Corporation, PRD Electronics Division, 6801 Jericho Turnpike, Syossett, NY 11791

145. P. S. Maruvada, Hydro-Quebec Institute of Research, 1800 Montee Ste-Julie, Varennes, Quebec.J0L2P0, CANADA

146. R. G. McCormack, CERL, U. S. Army Corps of Engineers, P. O. Box 4005, Champaign, IL 61820

146. C. Menemenlis, University of Patras, Patras, GREECE

147. David B. Miller, Mississippi State University, P. O. Drawer EE, Mississippi State, MS 39762

148. I. N. Mindel, IIT Research Institute, 10 West 35th Street, Chicago, IL 60616

149. D. L. Mohre, Cajun Electric Power Corporation, P. O. Box 15440, Baton Rouge, LA 70895

150. B. B. Mrowca, Baltimore Gas & Electric Company, P. O. Box 1475, Baltimore, MD 21203

151. K. Muller, IABG, Einsteinstrasse 20, Ottobrunn 8012, WEST GERMANY

153. E. M. Murtha, General Service Admin., Booz Allen and Hamilton, 18th & F Streets, NW, Washington, DC 10405

154. Dr. H. P. Neff, University of Tennessee, Dept. of Electrical Engineering, Knoxville, TN 37916

155. B. O. Nettles, Engineering Center, Navel Electronic System (Code 203) 4600 Marriott Drive, Charleston, SC 29418

156. D. R. Nevius, North American Electric Reliability Council, 101 College Road East, Princeton, NJ 08540-6601

157. Principal Engineer, Baltimore Gas & Electric Company, Room 1020, P. O. Box 1475, Baltimore, MD 21203

158. B. Noel, Los Alamos National Lab., Mail Station 5000, P. O. Box 1663, Los Alamos, NM 87545

159. B. Nowlin, Arizona Public Service Company, P. O. Box 21666, Phoenix, AZ 85036

160. R. Oates, Atomic Weapons Research Establishment, Building D57, Aldermaston, Reading RG74PR, ENGLAND

161. G. Orrell, Dep. Assoc. Director, Federal Emergency Management Agency, 500 C Street, SW, Washington, DC 20555

162. L. Paris, University of Pisa, Via Diotisalvi 2, PISA 56100, ITALY

163. R. Parker, R & D Associates, P. O. Box 9335, Albuquerque, NM 87119

164. R. Parkinson, Science Applications, Inc., 5150 El Camino Real, Suite B-31, Los Altos, CA 94022

165. A. Pigini, CESI, Via Rubahimo 59, Milano, ITALY

166. J. B. Posey, Ohio Brass Co., 380 N. Main Street, Mainsfield, OH 44903

167. M. Rabinowitz, Electric Power Research Institute, 3412 Hillview Avenue, P. O. Box 10412, Palo Alto, CA 94303

168. W. A. Radaski, Metatech Corporation, 358 South Fairview Avenue, Suite E, Goleta, CA 93117

169. Al Ramus, Maxwell Laboratories, Inc., 8835 Balboa Avenue, San Diego, CA 92123

170. J. J. Ray, Bonneville Power Administration, P. O. Box 3621, Portland, OR 97208

171. T. J. Reed, Advanced Systems Technology, Westinghouse Electric Corp., 777 Penn Center Boulevard, Pittsburgh, PA 15235

172. R. L. Retallach, American Electric Power, 1 Riverside Plaza, Columbus, OH 43216

173. J. Richardson, National Academy of Science, 2101 Constitution Avenue, Washington, DC 20418

174. F. Rosa, Division of System Intg., Nuclear Regulatory Commission, MS P1030, Washington, DC 20555

175. D. H. Sandell, Harza Engineering Co., 150 South Wacker Drive, Chicago, IL 60606

176. J. A. Sawyer, MITRE Corporation, MS-H070, P. O. Box 208, Bedford, MA 01703

177. R. A. Schaefer, Metatech Corporation, 20 Sunnyside Avenue, Suite D, Mill Valley, CA 94941

178. M. Schechter, A.D.A., P. O. Box 2250(81), Haifa 31021, ISRAEL

179. Dominique Serafin, Cente d'Etudes de Gramat, 46500 Gramat, FRANCE

180. H. Singaraju, Air Force Weapons Laboratory, Kirkland AFB, NM 87117

181. J. C. Smith, McGraw-Edison Company, Power Systems Group, P. O. Box 440 Canonsburg, PA 15317

182. A. C. Smith, Jr., Beam Research Program, Lawrence Livermore National Lab., P. O. Box 808, Livermore, CA 94550

183. R. Smith, Defense Nuclear Agency, RAEE, 6801 Telegraph Road, Alexandria, VA 22310

184. W. Sollfrey, RAND Corporation, 1700 Main Street, Santa Monica, CA 90406

185. H. Songster, Electric Systems Division, Electric Power Research Institute, 3412 Hillview Avenue, P. O. Box 10412, Palo Alto, CA 94303

186. G. K. Soper, Defense Nuclear Agency, Washington, DC 20305

187. S. Spohn, Defense Nuclear Agency, DB-6E2, Washington, DC 20301-6111

188. J. R. Stewart, Power Technologies, Inc., P. O. Box 1058, 1482 Erie Blvd., Schenectady, NY 12301-1058

189. R. L. Sullivan, Consultant, Gainesville, FL 32611

190. I. O. Sunderman, Lincoln Electric System, P. O. Box 80869, Lincoln, NE 68501

191. R. W. Sutton, Science Applications, Inc., 1710 Goodridge Drive, P. O. Box 1303, McLean, VA 22102

192. F. M. Tesche, LuTech Inc., 3724 Mt. Diablo Boulevard, Lafayette, CA 94549

193. The Citadel, Vice President, Charleston, SC 29409

194. R. J. Thomas, Cornell University, 302 Phillips Hall, Ithaca, NY 14853

195. R. Torres, BDM Corporation, 1801 Randolph SW, Albuquerque, NM 87106

196. W. Tyler, NT, Kirkland AFB, NM 87117

197. M. A. Uman, University of Florida, Department of Electrical Eng. Gainesville, FL 32611

198. E. F. Vance, Route 3, Box 268A, Fort Worth, TX 76140

199. Major Vandre, USA IDR, ATTN SGRD-UDR-E, Walter Reed Army Medical Center, Washington, DC 20307-5300

200. D. R. Volzka, Wisconsin Electric Power Company, 231 West Michigan Street, Milwaukee, WI 53201

201. C. B. Williams, IRT Corporation, 3030 Callan Road, San Diego, CA 92121

202. D. D. Wilson, Power Technologies, Inc., P. O. Box 1058, Schenectady, NY 12301

203. U. P. Wissmann, AEG-Telefunken, General Electric Company, 1 River Road, Building 36-444, Schenectady, NY 12345

204. D. A. Woodford, Manitoba Hydro, System Planning Division, P. O. Box 815 Winnipeg, Manitoba R-3C-2P4, CANADA

205. H. W. Zaininger, Zaininger Engineering Company, 3408 Vance Court, San Jose, CA 95132

206. Office of the Assistant Manager for Energy Research and Development, Oak Ridge Operations Office, DOE, P. O. Box E, Oak Ridge, TN 37831

207-740. For distribution as shown in TIC-4500, Distribution Category UC-97a,b,c

☆U.S. GOVERNMENT PRINTING OFFICE: 1987-748-168/40106